Synthesis and Characterization of Cu-based Catalysts resulting from Cu,Zn,X Hydrotalcite-like Compounds

vorgelegt von
Diplom Chemikerin
Stefanie Kühl
aus Berlin

Von der Fakultät II - Mathematik und Naturwissenschaften
der Technischen Universität Berlin
zur Erlangung des akademischen Grades
Dr. rer. nat.

genehmigte Dissertation

Promotionsausschuss:
Vorsitzender: Prof. Dr. R. Schomäcker
1. Gutachter: Prof. Dr. R. Schlögl
2. Gutachter: Prof. Dr. T. Ressler
3. Gutachter: Prof. Dr. M. Muhler

Tag der wissenschaftlichen Aussprache: 30.09.2011

Berlin 2012

D 83

Zusammenfassung

Cu,Zn,Al-Hydrotalcit (engl: layered double hydroxide – LDH) wird im Co-Fällungsschritt der bekannten $Cu/ZnO/Al_2O_3$ Katalysatoren zur Methanol Synthese als Nebenprodukt gebildet. In der vorliegenden Arbeit wurde das LDH System systematisch untersucht.

Zuerst wurde durch Co-Fällung ein phasenreines Cu,Zn,Al-LDH mit der Zusammensetzung $(Cu_{0.5}Zn_{0.17})Al_{0.33}(OH)_2(CO_3)_{0.17} \cdot m\,H_2O$ hergestellt. Es zeigt die typische plättchenförmige Morphologie sowie erwartete homogene Elementverteilung. Durch thermische Zersetzung in Luft wurde ein Carbonat-modifiziertes, amorphes, gemischtes Oxid gebildet. Dieses gemischte Oxid kann beschrieben werden als CuO, das gut verteilt ist in $ZnAl_2O_4$, das noch stabilisierendes Carbonat enthält und das eine starke Wechselwirkung von Cu^{2+} Ionen mit der Zn-Al Matrix aufweist. Nach der Reduktion, die der entscheidende Nanostrukturierungsschritt für den ex-LDH Katalysator ist, wurde ein Cu-basierter Katalysator erhalten, in dem Cu verteilt ist in einer $ZnAl_2O_4$ Spinell-ähnlichen Matrix. Aufgrund der hohen Einbettung der kleinen Cu-Partikel (7 nm) hat er nur eine kleine absolute Aktivität in der Methanol Synthese, verglichen mit einem konventionell hergestellten Referenzkatalysator, aber eine große intrinsische Aktivität (relativ zur Cu-Oberfläche), was die große Bedeutung des Grenzflächenkontaktes von Cu sowie dessen Umgebung zeigt.

Durch kontrollierte Co-Fällung innerhalb von Mikroemulsionstropfen wurde phasen-reines LDH mit kleineren Partikeln hergestellt. Daraus wurden kleinere $Cu/ZnAl_2O_4$-Aggregate mit geringerer Einbettung der resultierenden Cu-Partikel gewonnen. Dieser Cu-basierte Katalysator zeigte eine höhere absolute Aktivität in der Methanol-Dampfreformierung, wobei eine kleinere intrinsische Aktivität beobachtet wurde.

Des Weiteren wurden zwei Probenserien hergestellt, in denen Cr und Ga als substitierende Elemente für Al verwendet wurden, um ihre Effekte auf das ex-LDH Katalysator-System zu untersuchen und Verständnis für die Funktionalität von Al zu gewinnen. Nach thermischer Zersetzung in Luft wurden sowohl für Cr enthaltende Proben als auch für Ga Anteile $\leq 15\,at\%$, ähnlich zum Cu,Zn,Al-System, Carbonat-modifizierte gemischte Oxide gewonnen. Höhere Ga Anteile führten zur Bildung von kristallinem $Zn(Al,Ga)_2O_4$ oder $ZnGa_2O_4$ Spinell. In beiden Probenserien wurde keine Korrelation von Cu-Oberfläche und katalytischer Aktivität beobachtet. Letzten Endes zeigen diese Probenserien, dass es möglich ist eine Serie von Cu-basierten Katalysatoren mit der gleichen Synthesegeschichte herzustellen, die charakterisiert sind durch eine homogene Elementverteilung und eine vergleichbare Mikrostruktur aber signifikante Unterschiede in katalytischer Leistung, was auf Unterschiede in der intrinsischen Aktivität in der Methanol Synthese zurückgeführt werden kann. In allen hergestellten Proben konnte die Wechselwirkung zwischen Cu und der oxidischen Matrix als wichtiger Parameter identifiziert werden, um die intrinsische Aktivität zu kontrollieren.

Zusammenfassend lässt sich sagen, dass die Grenzflächenwechselwirkungen von Cu und der oxidischen Matrix die Aktivität von Cu-Partikeln positiv zu beeinflussen scheinen und dass ein optimaler Katalysator einen Kompromiss zwischen exponierter Oberfläche und Grenzfläche benötigt. Sowohl die Modifizierung der Grenzfläche (Cr) als auch die Art der Grenzflächenwechselwirkung (Ga) wurden als Möglichkeit gezeigt, diese positiven Wechselwirkungen zu nutzen und den resultierenden Katalysator zu modifizieren.

Abstract

Cu,Zn,Al layered double hydroxide (LDH) are formed as a by-phase during the co-precipitation step of the well known $Cu/ZnO/Al_2O_3$ catalysts for methanol synthesis. In the present work the LDH system was investigated systematically.

First of all, a phase pure Cu,Zn,Al LDH was prepared by co-precipitation, resulting in the composition $(Cu_{0.5}Zn_{0.17})Al_{0.33}(OH)_2(CO_3)_{0.17} \cdot m\,H_2O$ and showing the typical platelet-like morphology and homogeneous elemental distribution. Upon decomposition in air a carbonate-modified, amorphous mixed oxide was formed. This mixed oxide can be described as well dispersed CuO within $ZnAl_2O_4$ still containing stabilizing carbonate and showing a strong interaction of Cu^{2+} ions with the Zn-Al matrix. After reduction, the main nanostructuring step of ex-LDH catalyst, a Cu based catalyst was obtained with Cu dispersed in a $ZnAl_2O_4$ spinel-like matrix. Due to the high embedment of the small Cu particles (7 nm) it exhibits just a small absolute activity in methanol synthesis compared to the conventionally prepared reference catalyst but a high intrinsic one (relative to the Cu surface area) showing the high importance of the interface contact of Cu and its surrounding.

By pH-controlled co-precipitation within microemulsion droplets a Cu-based catalysts was prepared from a phase pure LDH with smaller particles. Thus, smaller $Cu/ZnAl_2O_4$ aggregates with less embedment of the resulting Cu particles were obtained and a higher activity in methanol steam reforming was observed. However, a smaller intrinsic activity was observed in methanol steam reforming.

Furthermore, two sample series were prepared using Cr and Ga as substituting elements for Al to investigate their effects onto the ex-LDH catalyst system and to gain understanding of the functionality of Al. After decomposition in air carbonate-modified mixed oxides were obtained for Cr containing samples as well as for Ga contents $\leq 15\,\mathrm{at\%}$, similar to the Cu,Zn,Al system. Higher Ga contents led to the formation of crystalline $Zn(Al,Ga)_2O_4$ or $ZnGa_2O_4$ spinel. Both sample series did not show a correlation of Cu surface area and catalytic activity. After all, these sample series show that it is possible to prepare a series of Cu based catalysts with the same preparation history, which are characterized by a homogeneous elemental distribution and a similar microstructure but significant differences in catalytic performance attributed to differences in intrinsic activity in methanol synthesis. In all prepared sample series, the interaction between Cu and the oxide matrix was identified as an important parameter to control this intrinsic activity.

In summary, interface interactions between Cu and the oxide seem to beneficially affect the activity of the Cu particles and the optimal catalyst requires a compromise of exposed surface and interface. The modification of the interface area (Cr) as well as the type of the interface interaction (Ga) were reported to be a possibility to use these positive interactions and modify the resulting Cu based catalyst.

Table of Contents

7 Final Discussion   **121**

List of Figures

List of Tables

List of Abbreviations

BET adsorption isotherm model of Brunauer, Emmet and Teller

DLS dynamic light scattering

DSC differential scanning calorimetry

LDH layered double hydroxide

ME microemulsion

MS mass spectrometry

NEXAFS near-edge x-ray absorption fine structure

PSD particle size distribution

RFC reactive frontal chromatography

SA surface area

SEM scanning electron microscopy

TCD Thermal conductivity detector

TEM transmission electron microscopy

TEY total electron yield

TG thermogravimetry

TPO temperature programmed oxidation

TPR temperature programmed reduction

WTY weight time yield

XAS x-ray absorption spectroscopy

XPS x-ray photoelectron spectroscopy

XRD x-ray diffraction

XRF x-ray fluorescence anaylsis

1 Introduction

Besides ammonia and sulfuric acid, methanol belongs to the most important, industrially produced basic chemicals. In 2007 35 million tons were produced and consumed [1], and until 2009 the global consumption increased to 42 million tons [2]. Recently, most of the produced methanol is used as educt for the production of
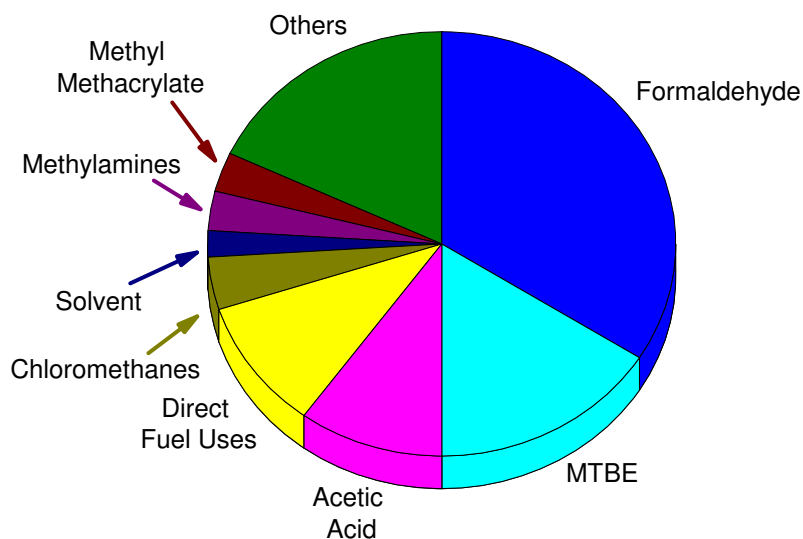
Figure 1.1: Distribution of global consumption of methanol in 2009 [2].

formaldehyde, methyl tertiary butyl ether (MTBE), acetic acid and other chemicals (see Fig. 1.1) [2].

A relative small, but growing sector of the application of methanol are fuels. The high potential of methanol as a fuel arises from its promising properties. It can be converted to hydrogen at lower temperatures (150 - 350 °C) than most other fuels (> 500 °C) because no carbon-carbon bond has to be broken [1]. Furthermore, methanol has a high H/C ratio (4 : 1) and is liquid at atmospheric pressure and ambient temperatures. Thus, it is often called "liquid hydrogen storage" [1, 3].

1.1 Methanol Synthesis

The first synthetic plant for methanol synthesis was commercialized by BASF AG in 1923 where methanol was produced from carbon monoxide and hydrogen using a ZnO/Cr_2O_3 catalyst at high temperatures (300 - 400 °C) [3].

In the 1960s the *ICI* (*Imperial Chemical Industries*) developed the synthesis of methanol by syngas produced from sulfur-free natural gas. Thus, it was possible to use copper based catalysts which are more active (reaction temperatures of 250 - 350 °C) but also more sensitive to catalyst poisons like sulfur [3]. Today, still a finely tuned $Cu/ZnO/Al_2O_3$ catalyst is used in industry for the low-pressure methanol synthesis from syngas (consisting of carbon monoxide, carbon dioxide and hydrogen) [4].

The formation of methanol by conversion of syngas can proceed by the hydrogenation of both CO (Eq. (1.1)) as well as CO_2 (Eq. (1.2)) [5].

$$CO + 2\,H_2 \quad \rightarrow \quad CH_3OH \tag{1.1}$$

$$CO_2 + 3\,H_2 \quad \rightarrow \quad CH_3OH + H_2O \tag{1.2}$$
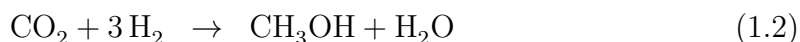
Additionally to methanol formation, CO conversion, the so called water-gas-shift reaction (Eq. (1.3)), as well as its back reaction are running on the same catalyst.

$$CO + H_2O \rightleftharpoons CO_2 + H_2 \tag{1.3}$$

1.1.1 Catalysts for Methanol Synthesis

Nowadays, all catalysts used for the low-pressure methanol synthesis consist of copper and zinc oxide, and mostly alumina as stabilizing component [6]. Mostly empirical optimization has led to a preparation route for the widely used $Cu/ZnO/Al_2O_3$ catalysts based on co-precipitation, followed by calcination and reduction [7, 8] – called "conventionally prepared catalyst" in the following. After co-precipitation a mixture of different hydroxy carbonates results: malachite ($Cu_2(CO_3)(OH)_2$), rosasite (($Cu,Zn)_2(CO_3)(OH)_2$), aurichalcite (($Cu,Zn)_5(OH)_6(CO_3)_2$) and Cu,Zn,Al-hydrotalcite-like compounds [4, 9]. An intimate mixture of the oxides can be obtained by calcination. Afterwards, the CuO component is reduced yielding highly dispersed and catalytically active Cu.

During the years different models were presented about the active phase of Cu based catalysts. The precise knowledge of the active phase would allow for a modification of the catalyst to gain a high amount of these species [3]. First Klier et al. [10] suggested Cu^+ species dissolved in the ZnO structure, forming a solid solution. Another model proposed a Schottky barrier at the Cu-ZnO interface as active phase [11], which favors the formation of oxygen vacancies, active for the chemisorption of CO and CO_2.

Grunwaldt et al. claimed that the difficulty of the characterization of the active phase of the Cu/ZnO catalysts is due to their variable structure [12]. The so called Topsøe model suggests a variation of the catalyst surface in dependence of the applied gas atmosphere. These effect, schematically shown in Figure 1.2, was observed by EXAFS investigations of a Cu/ZnO catalyst with a Cu loading of 4.5 wt%. While
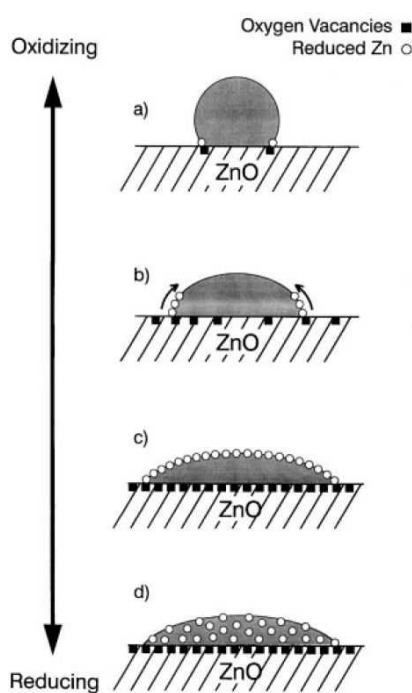
Figure 1.2: Schematic model of the dynamic behavior of metallic Cu particles on the ZnO support [12].

under oxidizing syngas conditions spherical Cu particles are present beside ZnO (Fig. 1.2(a)), a reducing syngas (Fig. 1.2(b)) results in an increasing wetting of the ZnO support by Cu particles (strong metal support interaction). Strongly reducing

conditions (only H_2 und CO) led to the formation of oxygen vacancies at the Cu-ZnO interface and an even dispersion of the Cu particle on top of the vacancies ((Fig. 1.2(c))). The formation of surface Cu-Zn alloying and finally bulk alloying (brass formation), which is catalytically inactive, was observed under severe reducing conditions ((Fig. 1.2(d)). The formation of the highly active species for the methanol synthesis was proposed to occure in between the two extreme conditions.

Nauman d´Alnoncourt et al. [13] described a partial covering or encapsulation of Cu particles by ZnO_{1-x}, observed under strongly reducing conditions, as the SMSI effect.

Additionally, microstructural strains within the Cu particles, implemented by the hydroxycarbonate precursors, were described by Bems et al. [14] and Günter et al. [15] to enhance the catalytic activity.

1.2 Layered Double Hydroxides

Cu,Zn,Al hydrotalcite-like compounds are formed as a by-phase during the co-precipitation step of the above described $Cu/ZnO/Al_2O_3$ catalysts (Chap. 1.1.1).

The mineral hydrotalcite, $Mg_6Al_2(OH)_{16}CO_3 \cdot 4\,H_2O$, as a hydroxy carbonate of Mg and Al is a white hydrous material with a rhombohedral crystal structure [16]. It was found in South Wales and Tasmania, Australia, whereas its site of first occurrence is Snarum, Norway. In current literature this mineral group is named layered double hydroxide (LDH). It is used as a description for synthetic or natural lamellar hydroxides with divalent and trivalent cations in the main layer and different inorganic or organic anions in the interlayer. In general LDH´s can be described with the formula $[M^{II}_{1-x}M^{III}_x(OH)_2]^{x+}(A^{n-}_{x/n}) \cdot m\,H_2O$ [16].

As the name suggests LDH´s are layered structures composed of two alternating, structurally and chemically different layers. Their structure is related to that of brucite $(Mg(OH)_2)$, where Mg^{2+} ions are octahedrally coordinated by hydroxyl-groups forming edge-linked octahedra, and hydrogen bonds are connecting these layers [17]. In LDH´s part of the M^{2+} cation position of brucite is occupied by M^{3+} cations with a similar ionic radius. The resulting positive charge necessitates the presence of interlayer, charge balancing anions [18]. Typically, this charge compensation is achieved by planar carbonate groups intercalating between the brucitic layers, as

shown schematically in Figure 1.3. Besides the additional anions, water molecules
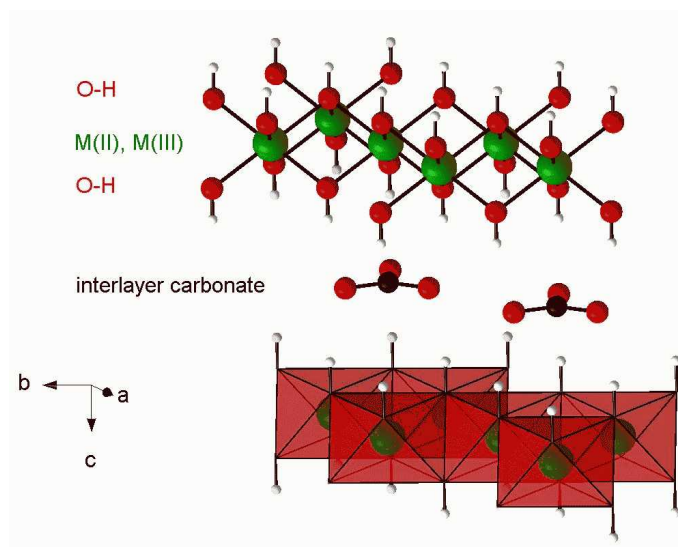
Figure 1.3: Schematic structure of LDH compound.

are located in the interlayer, occupying the remaining free space and connecting the hydroxyl groups of the brucitic layer via hydrogen bonds.

In LDHs the cation coordination sphere is far from the regular octahedron. Indeed, the octahedra are strongly flattened along the stacking direction, lowering the symmetry from O_h (m3m) to D_{3d} (-3m) [19]. The higher the mean ionic radius of the metal cation, the more flattened are the octahedra with a lowering of the layer thickness and an increase of the metal–metal distance. Furthermore, two different geometries for the stacking of the brucitic layers are described in literature [16, 17]:

- **BC–CA–AB–BC**: rhombohedral unit cell with three layers,
- **BC–CB–BC**: hexagonal unit cell with two layers.

The rhombohedral and hexagonal structures are very similar and only differ in the stacking sequence of adjacent brucite layers $[M^{II}6M^{III}2(OH)_{16}]^{2+}$ and the interlayers in the type of $[CO_3 \cdot 4H_2O]^{2-}$ [20]. Both natural and synthetic LDH compounds are mainly rhombohedral [16].

One major characteristic of LDHs is that, in most cases, only weak bondings occur between interlamellar ions or molecules and the brucitic main layer. Therefore, a great variety of anionic species can be incorporated within the layers, directly during

the formation of the layered structure or by later anionic exchange [19]. These anions can belong to

- halides: fluorides, chlorides, . . . ,

- oxo-anions: carbonates, nitrates, sulfates . . . ,

- oxo- & polyoxo-metallate: chromates, dichromates, . . . ,

- anionic complexes: ferro- & ferricyanide, $[PdCl_4]^{2-}$, . . . , and

- organic anions: carboxylates, phosphonates, alkyl sulphates, ...

In relation to the size, the charge and the ordering of these interlamellar species, the interlayer space is modified dramatically as shown schematically in Figure 1.4 for a selection of inorganic and organic anions [19].
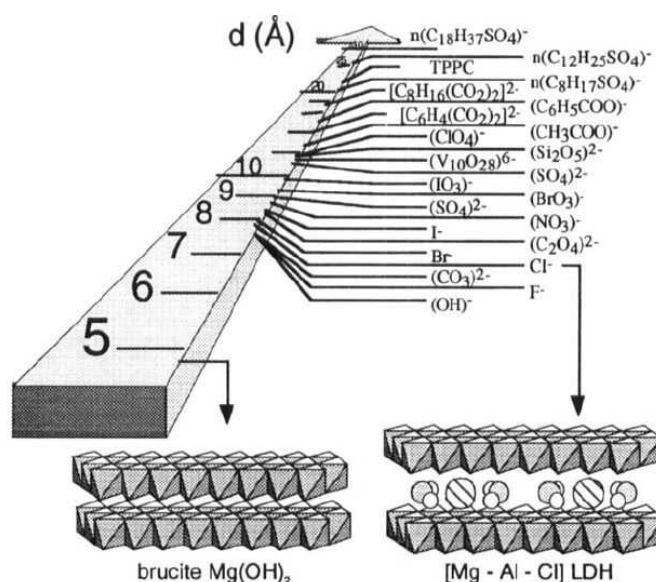
Figure 1.4: Evolution of interlayer space depending on intercalated anion [19].

1.2.1 LDH as precursor for Cu based catalysts

In general, it is simple and inexpensive to synthesize LDH on laboratory and industrial scales. First synthetic LDHs where prepared by Feitknecht et al. in 1942 by conversion of dilute $MgCl_2$-$AlCl_3$ solutions with sodium hydroxide [21, 22]. The most common method to obtain LDHs is the co-precipitation method [19], which was already

mentioned as the method of choice for the preparation of the Cu based catalysts precursors (see Chap. 1.1.1). Furthermore, there were other methods applied for the preparation of LDH such as hydrothermal synthesis or post-treatment [23] and cation and/or anion exchange methods [17, 18, 24]. Cavani et al. [17] claimed that the first requirement to obtain phase pure LDH is the right ratio of cations and anions. For the preparation of Cu,Zn,Al mixed hydroxy carbonate precursors, Trifiro et al. [25] have reported that phase pure $CuM^{II}M^{III}$ LDH compounds are only formed for $Cu:M^{II}$ ratios ≤ 1 and $(Cu + M^{II}):M^{III}$ ratios ≈ 3, claiming that deviances of these values led to Cu,Zn hydroxy carbonates of malachite kind.

The application of LDH precursors for catalysis has been comprehensively reviewed by Cavani et al. [17] as well as by Forano et al. [16], both highlighting their potential due to the homogeneous distribution of all metal cations inside the brucite layers, yielding well-dispersed, small and stable metal particles on mixed oxides support after calcination and reduction. Busetto et al. [26] reported that the smallest Cu particles were found for $Cu/ZnO/Al_2O_3$ catalysts with high amounts of LDH phase within their precursor. Hence, LDH is proposed to work as stabilizer preferring the formation of small and stable oxide particles as well as small Cu particles [27]. Furthermore, Turco et al. [28] presented a $Cu/ZnO/Al_2O_3$ catalyst for oxidative methanol reforming derived from hydrotalcite-like precursor, containing $18\,at\%$ Cu, where paratacamite was observed as by-phase $(33\,wt\%)$ after co-precipitation.

In a previous study we have reported about Cu-rich phase pure Cu,Zn,Al hydrotalcite obtained by co-precipitation [29]. Therein, the investigation of a series of samples with the general composition $(Cu,Zn)_{1-x}Al_x(OH)_2(CO_3)_{x/2} \cdot m\,H_2O$ with a fixed Cu:Zn ratio of $70:30$ was presented, where phase pure samples were found for $0.3 \leq x \leq 0.4$, which strongly deviates from the above mentioned requirements of cation ratios. Such Cu,Zn,Al hydrotalcites are promising catalyst precursor materials as they show a homogeneous distribution of the metallic and oxidic components on an atomic level, resulting in very small Cu particles. A detailed investigation of the prepared sample series showed that during calcination two different kinds of material were formed from the single phase precursors – amorphous areas with Zn and Al in the spinel ratio $1:2$ and granular areas, which are either depleted in Zn or Al (depending on the precursor composition). In case of a precursor composition approaching a Zn:Al ratio of $1:2$ little or no segregation was observed during calci-

nation suggesting the formation of a $Cu/ZnAl_2O_4$-type catalyst in which the spinel phase is X-ray amorphous.

1.3 Outline of the work

As already mentioned (Chap. 1.1), the industrial applied catalyst system results in catalyst precursors usually comprised of a phase mixture of different hydroxy carbonates [30]. Due to the varying $Cu:Zn$ ratios of the single phases and their typically low crystallinity these mixtures are hard to characterize comprehensively [14, 31]. However, it can be expected that all components of the precursor lead to different domains in the $Cu/ZnO/Al_2O_3$ catalysts with different types of material and individual catalytic properties. Alltogether, these domains form the highly active industrial system containing an inhomogeneous microstructure [32]. In literature, the relevance of the individual precursor phases for applied $Cu/ZnO/Al_2O_3$ or binary Cu/ZnO model catalysts is discussed controversially. Aurichalcite [33], rosasite [34], zincian malachite [35], as well as a phase mixture of rosasite and hydrotalcite [9] have been suggested as desired precursor phases leading to highly active catalysts.

This thesis will concentrate on the hydrotalcite phases only. The hydrotalcite or LDH system, as a typical component of the complex phase mixture in conventionally prepared precursor materials, is investigated to obtain information on its role in the conventional catalyst system. The main objective is to make a contribution to the understanding of the complex chemistry underlying the Cu based catalysts. The objective is to prepare phase pure LDHs with a homogeneous distribution of all metal components on an atomic level, a high surface area and a narrow particle size distribution (PSD). Under these circumstances, the formation of catalysts of a homogeneous microstructure exhibiting a high dispersion of the metal species and an enhanced metal-oxide interaction after reduction can be expected. The main characteristic of the catalysts of the previous study [29] (see also Chap. 1.2.1) was that the resulted Cu particles were to a large extent not accessible to the reaction gas, as the particles were strongly embedded into the oxidic matrix. A large Cu surface area is, however, a prerequisite for high catalytic performance of $Cu/ZnO/Al_2O_3$ catalysts [36]. Furthermore, it is known that in addition to a large Cu surface area also intrinsic factors can affect the surface normalized activity of Cu [36, 37]. We

have recently shown that the embedment of Cu nanoparticles in ZnO/Al_2O_3 may benifically affect the intrinsic activity of the exposed Cu surface area [38] in methanol synthesis, i.e. the activity or concentration of the active sites on the Cu surface. This effect is probably related to the stabilization of a strained and/or defective form of Cu. Lattice strain [15] and planar defects [32] have been identified in previous studies as indicators for high intrinsic activity of the exposed Cu surface area. It has to be mentioned, that the main objective of this thesis is not to prepare a better catalyst but to make a contribution to the understanding of the complex chemistry underlying these Cu based catalysts.

First of all, the Cu,Zn,Al LDH precursor as well as the resulting calcined and reduced sample are investigated carefully, including a detailed evaluation of the reduction behavior. The nominal composition is chosen to $Cu : Zn : Al = 50 : 17 : 33$, as a high copper content is necessary to be comparable to industrially used catalysts. Otherwise, it was shown before [29] that a homogeneous microstructure should result with a $Zn : Al$ ratio of $1 : 2$.

By applying a pH-controlled co-precipitation within microemulsion droplets to the LDH precursor system it is supposed to influence the nucleation during the precipitation process to finally form small Cu particles with improved accessibility to the reactant gas, but still show a good stability during reaction.

Furthermore, as LDH enables the insertion of a broad variety of cation composition, it is representing a precursor system with a powerful basis to study the effect of different promoter species on the redox- and catalytic properties independent of Cu content and preparation history, which is generally influencing the resulting catalyst [39]. Al in its oxidic form is supposed to be a multifunctional promoter, which is working as a separator as well as an important species on the interface to Cu [40, 41]. Within this thesis Al is substituted stepwise by Cr and Ga to investigate their effects onto the ex-LDH catalyst system to gain understanding of the functionality of Al and to insert new properties into the system which Al does not have.

All prepared catalysts as well as their precursors were thoroughly characterized by various methods, including XRD, BET, TGA, TPR and N_2O-RFC. For selected samples TEM, NEXAFS and XPS investigation was performed.

2 Methodology – fundamentals and theoretical details

2.1 X-ray Diffraction

X-ray diffraction (XRD) is a non-destructive technique widely applied for characterization of crystalline materials [42]. In catalyst research, XRD is applied for phase identification, quantitative analysis, and quantification of structural imperfections. Mainly it is used for the control of all preparation steps in the synthesis procedure of solid catalysts [43]. Commercial X-ray powder diffractometers are typically equipped with Cu Kα radiation, which is available from standard X-ray tubes with a power of around 2 kW.

The qualitative phase analysis of a given pattern is based on the comparison of the line positions and intensity distributions of a set of reflections with a database [43]. Most commonly, the Powder Diffraction File (PDF), distributed by the International Centre for Diffraction Data (ICDD) is used [44]. Solid catalyst material often consists of nanocrystalline phases resulting in significant line-broadening in X-ray diffraction.

Figure 2.1 shows a typical XRD pattern of an Cu,Zn,Al-LDH obtained by co-precipitation. It consists of sharp basal reflections at small values of 2θ corresponding to successive orders of the interlayer spacing [18]. Additionally, relatively weak non-basal reflections are present at higher angles.

For a constant thickness of the brucite layer, e. g. constant cation composition, the d-spacing of the (00l)-reflections near 12 and 24°2θ correspond directly to the interlayer space [18].
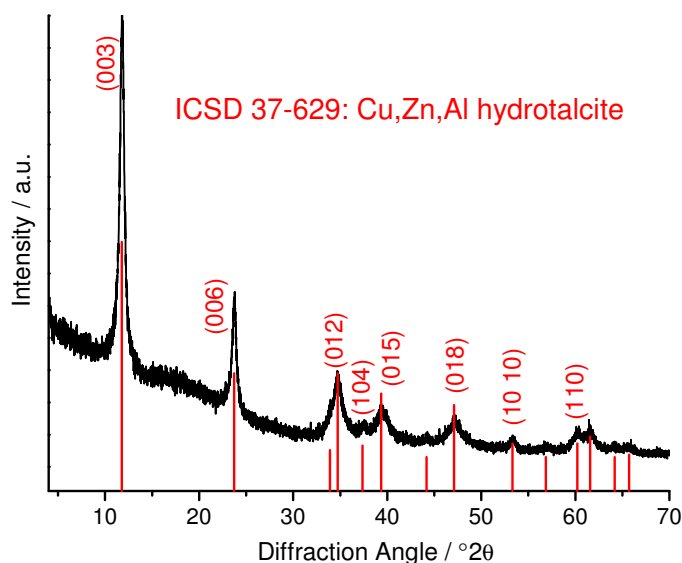
Figure 2.1: Example of XRD pattern of Cu,Zn,Al-LDH compound.

2.2 Temperature Programmed Reduction

The temperature programmed reduction (TPR) is a technique where at the same time a solid (typically reducible catalyst precursor) is exposed to a reducing gas mixture (H_2 or CO in argon or nitrogen) and the temperature is increased with a defined heating rate [45]. The reduction progress is continuously followed by measuring the composition (H_2 or CO content) of the reducing gas mixture at the outlet of the reactor. A typical TPR setup consists of a fixed-bed reactor in a furnace which can be temperature programmed and a Thermal conductivity detector (TCD) for determination of the gas composition. TPR can be used

- to find the most effective reduction conditions,
- to identify the phases of a catalyst and their interactions with the support,
- and to investigate the influence of an additional metal component.

It is a highly sensitive method, which does not depend on any specific property of the catalyst other than that the investigated species is in an reducible state [46].

Similarly to TPR, the oxidation behavior of a catalyst can be studied by means of temperature programmed oxidation (TPO). It is often used complementary to TPR experiments in order to study the reversibility of reduction and re-oxidation cycles of a catalyst and with that as a "stress-test" for the catalyst.

As this thesis is just about Cu based catalysts, this section will mainly concentrate on the reduction of copper oxide. Its reduction by hydrogen leads to the formation of Cu metal and water vapor (Eq. (2.1)).

$$CuO(s) + H_2(g) \longrightarrow Cu^0(s) + H_2O(g) \tag{2.1}$$
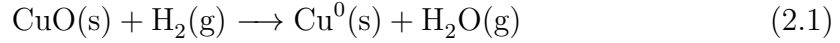
The free energy change (ΔG) of the reduction can be described by Equation (2.2) [46].

$$\Delta G = \Delta G^\circ + RTlog\left(\frac{p_{H_2O}}{p_{H_2}}\right) \tag{2.2}$$

The reduction is thermodynamically feasible only if ΔG is below zero. This is the case either for negative values of ΔG$^\circ$ (standard free energy change) or for small partial pressures of water (e.g. by increasing the flow rate) which results in high negative values for the logarithm. The change of the standard free energy is tabulated for several oxides [46]: For CuO it is below zero whereas both ZnO and Al$_2$O$_3$ have positive values which makes it possible to just reduce CuO in the system CuO/ZnO/Al$_2$O$_3$.

Furthermore, the shape of the obtained profiles, the temperature of the maximum reduction rate T$_M$ (maximum of the profile), as well as the resolution of the profiles are highly sensitive towards small variations in experimental parameters employed. Monti and Baiker [47] deeply investigated the influence of experimental parameters like hydrogen concentration, flow rate, heating rate and amount of reducing sample. They observed that an increasing heating rate led to an increase of the temperature with the maximum reduction rate T$_M$. An increase of the hydrogen concentration results in a higher T$_M$ and, furthermore, a decrease of the sensitivity of the method. On the other hand, changes of the flow rate as well as the amount of sample have just small influences on T$_M$.

To avoid large deformations of the TPR profile and, above all, to compare different measurements, it is necessary to choose the experimental parameters carefully. Monti and Baiker [47] defined a characteristic number K (see Eq. (2.3)), which correlates these parameters and thus facilitate the selection of appropriate operating variables.

$$K = \frac{S_0}{F \cdot c_0} \tag{2.3}$$

There, S_0 is the amount of reducing sample (μmol), F the flow rate (mL/min) and c_0 the starting concentration of hydrogen. For experimental relevant heating rates β between 6 and 18 K/min, K should have values between 55 s and 140 s. For smaller values the sensitivity is too low and for higher values the hydrogen consumption is too high, probably yielding in reduction profiles with a plateau as maximum. In experiments, which were done with optimized values of K good accordance was achieved between measured and simulated profiles.

Malet and Caballero have modified this value with the heating rate [48], by defining a characteristic number P (Eq. (2.4)). They suggested to get comparable TPR profiles the number P should have values ≤ 20 K.

$$\text{P} = \frac{\beta \cdot S_0}{F \cdot c_0} \tag{2.4}$$

Within this thesis the TPR conditions are set using both criteria to get comparable TPR profiles for the characterization of the ex-LDH catalyst system under analytic reaction control. Furthermore, the aim are profiles with a maximum of resolution to get the information of the amount of underlying processes without examining if the processes are thermodynamic or kinetic ones.

Characteristic for gas-solid reactions, like the reduction of a metal oxide with hydrogen, is that they are processing on an interface between the solid educt and solid product (metal oxide and reduced metal) called reaction interface. TPR data can be interpreted using the nucleation or the contracting sphere model [45], which are explained below. Both models are based on the assumption of a direct reduction of a sphere of metal oxide to metal [46], in a stream of flowing hydrogen. To get information about the occuring reduction mechanism, it is common to observe the degree of reduction α as a function of time t.

Characteristic for the nucleation model is the slow formation of the first nuclei of the solid product, which determines the reduction rate. In this case, the reduction starts after some time t_1, when the first oxygen ions are removed from the lattice by reduction. As soon as the concentration of formed vacancies reaches a critical value, the lattice rearranges and eventually first metal nuclei are formed [49]. The reaction interface begins to increase more and more rapidly because of the growth of already formed nuclei and the appearance of new nuclei. At a certain stage of the reduction the metal nuclei on the surface of the oxide particle have grown to

an extent where they touch each other forming a coating layer on top of the oxide grain [45]. Consequentially, the reaction interface is decreasing, which continues until the oxide is completely reduced. Figure 2.2(a) illustrates this nucleation mechanism which results in a sigmoidal α versus t plot as well as a maximum in the dα/dt versus t plot (t_1 is the induction time before the reduction starts) [46].
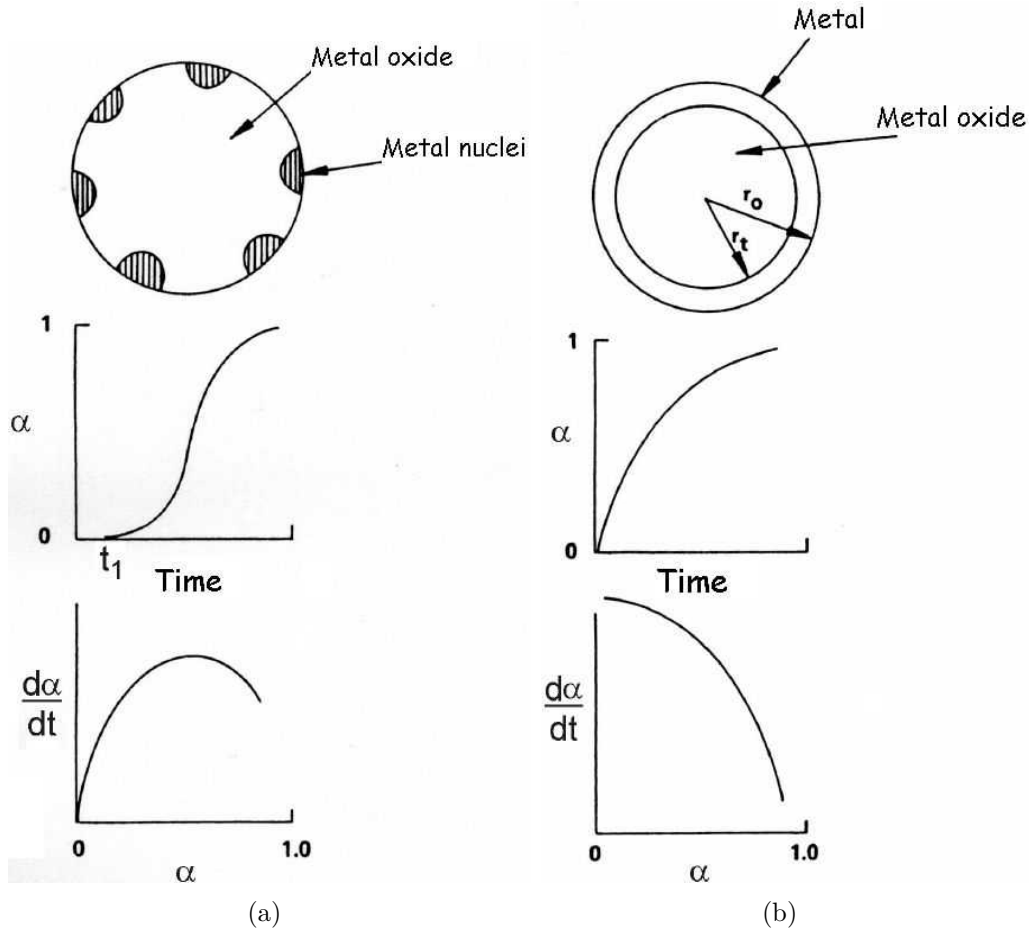
Figure 2.2: Schematically description of (a) nucleation model, and (b) contracting sphere model for metal oxide reduction [46]; α is the degree of reduction.

In other cases the reaction interface decreases continuously from the beginning of the reduction which is characteristic for the contracting sphere model. This follows by a very rapid nucleation resulting in a complete coverage of the oxide grain with a thin layer of metal in the first instant of the reaction [46]. Consequentially, the reaction interface decreases as the substrate grain is consumed in the course of the

reduction. Figure 2.2(b) shows the decreasing metal/metal oxide interface which results in the curved α versus t plot and the continously decreasíng reaction rate throughout the reduction (dα/dt versus t) of a metal oxide [46].

The distinction between the two models is mainly between a reaction interface (and hence rate) which is increasing in the early stages of the reduction process (nucleation model), and a reaction interface which is contracting throughout the reduction (contracting sphere model). The final stage in the nucleation model, where the reaction interface is shrinking as the metal layer grows, is equivalent to the contracting sphere model [45].

Activation energy

Wimmers et al. [50] described a procedure to determine the activation energy of the reduction of a catalyst precursor from TPR data. The reaction rate of solid-gas reactions can be described by Equation (2.5), $f(\alpha)$ is the model function to describe the gas-solid reaction and α, as already known, is the reaction progress.

$$\frac{d\alpha}{dt} = k(T) \cdot f(\alpha) \tag{2.5}$$

In TPR the temperature increases linearly with time at a heating rate β, thus the reaction rate equation can be rewritten as Equation (2.6), where the rate constant k can be expressed by using the Arrhenius equation (Eq. (2.7)).

$$\frac{d\alpha}{dT} = \frac{1}{\beta} \cdot k(T) \cdot f(\alpha) \tag{2.6}$$

$$\frac{d\alpha}{dT} = \frac{A}{\beta} \cdot e^{-E_A/RT} \cdot f(\alpha) \tag{2.7}$$

From the measurement of TPR profiles with different heating rates a modified temperature programmed "Arrhenius plot" is obtained from Equation (2.8) – under the assumption that the resulting displacement of maximum reduction temperature (T_M) is independent of the reduction mechanism [50].

$$ln\left(\frac{\beta}{T_{max}^2}\right) = \frac{-E_A}{RT_{max}} + ln\left(\frac{AR}{E_A}\right) + C \tag{2.8}$$

From the slope of that modified "Arrhenius plot" the apparent activation energy can be determined. It is simplified description of the complex reduction processes without knowing the elementary steps. Within this thesis the apparent activation energy is used as a tool to compare different kinds of catalysts.

2.3 Determination of Cu surface area

For the determination of the specific Cu surface area the principle of N_2O-reactive frontal chromatography (RFC) is used. This technique is based on the decomposition of nitrous oxide molecules on the surface of copper to produce chemisorbed oxygen atoms and gas phase nitrogen (Eq. (2.9)) [51].

$$N_2O_{(g)} + 2\,Cu_{(s)} \longrightarrow N_{2(g)} + (Cu{-}O{-}Cu)_{(s)} \tag{2.9}$$
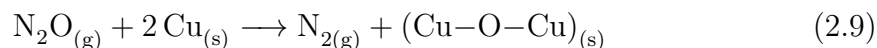
To avoid subsurface oxidation the experiments are carried out at $30\,°C$ [52]. The amount of nitrogen formed is quantified from the time interval of the frontal chromatogram of N_2, i.e. the time interval between the onset of appearance of N_2 and the breakthrough of N_2O. The Cu surface area is calculated assuming a molar stoichiometry of $Cu_{(s)}/N_2 = 2$ and a value of $1.46 \cdot 10^{-19}$ copper atoms m^{-2} [53].

2.4 X-ray Absorption Spectroscopy

X-ray absorption spectroscopy (XAS) is the only spectroscopic technique that provides information on the electronic and structural properties of catalysts under reaction conditions [54]. XAS is classified in two experimental methods, which are both used at synchrotron radiation facilities. The method called near-edge x-ray absorption fine structure (NEXAFS) determines a region of approximately $100\,eV$ directly at the absorption edge. Due to the position and the shape of the adsorption edge, it is possible to get information about the chemical bounding by comparison with reference materials and literature data by measurements in this region [55]. Furthermore, NEXAFS is strongly sensitive to the chemistry of the absorbing atom – formal oxidation state and geometry. EXAFS (extended x-ray absorption fine structure) describes the region upto $1\,keV$ after the absorption edge. The measurements in this

region yield information about the number of the neighboring atoms as well as their distances.

In a x-ray absorption process, a core level electron is excited to an empty state above the Fermi level. The basis of NEXAFS is the investigation of the electronic structure of the unoccupied levels of a system by scanning the photon energy (excitation energy) [56]. There are several techniques of detection of x-ray absorption, e.g. the transmission mode. Within this thesis only the total electron yield (TEY) was used as indirect detection method. It is a surface sensitive method, where electrons emitted by the sample are detected with a electron multiplier. These electrons are created by a cascade of multiple collisions of photoelectrons and auger electrons [56]. The information depths for transition metal oxides with TEY is estimated to approximately 4 nm [57].

2.5 Electron Microscopy

In addition to the bulk structural methods, such as XAS and XRD, which yield bulk structural information, electron microscopy provides information about the local elemental composition, structure and morphology of nanoparticles with the resolution ranging from micrometer scale down to atomic one [58]. By exposing the sample to an electron beam several processes are triggered due to the interaction of the primary electrons and the investigated sample (see Fig. 2.3). When electrons are colliding with atoms, they can simply be scattered back or collide inelastically and transfer their energy to secondary electrons. Other electrons pass through the sample with or without suffering energy loss or they are scattered by particles. Photons in the range from UV to infrared mainly result from a recombination of electron-hole pairs in the sample.

2.5.1 Scanning Electron Microscopy

In scanning electron microscopy (SEM) an image of the sample surface is obtained by scanning it with an electron beam in a raster pattern [58]. The ratio of the scanned area to the display area determines the magnification. Mostly secondary electrons (SE) which have low-energies ($0 - 100\,\text{eV}$) are used in imaging modes giving information about the surface topography. Besides this, backscattered electrons
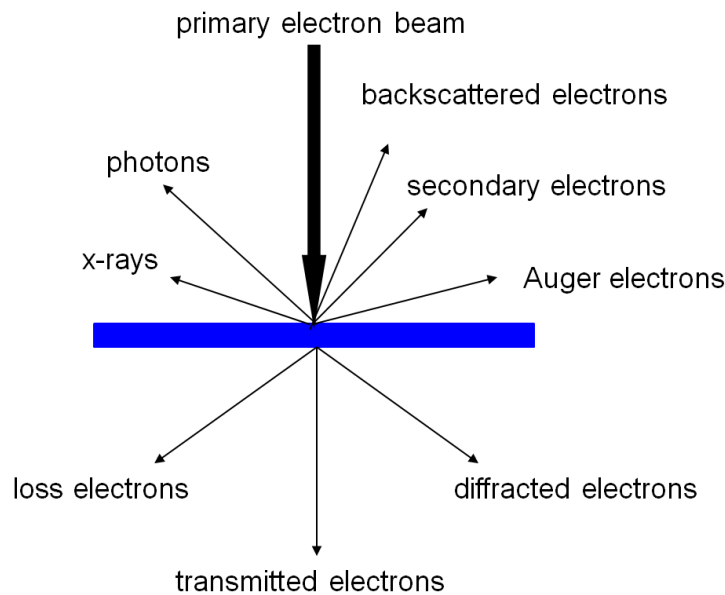
Figure 2.3: Interaction of primary electrons and the sample.

(BSE), which have energies comparable to those in the incident beam $(1 - 30 \, \text{keV})$, are used in SEM to gain information about the sample composition.

2.5.2 Transmission Electron Microscopy

In transmission electron microscopy (TEM) a primary electron beam of high energy $(100 - 200 \, \text{keV})$ and high intensity passes through a sample while the attenuation of the beam depends on the density and the thickness of the investigated sample [59]. Magnified images of the sample are formed by combining the transmitted electrons by means of an electromagnetic objective lens [58] representing a two-dimensional projection of a three-dimensional sample. Elastic scattering of electrons by atoms of the sample refract the primary electron beam and, consequently, the diffracted beam intensity increases at the expense of the intensity of the primary electron beam [59]. The fraction of elastically scattered electrons depends on structure, orientation, chemical composition, and defects of the sample. Accordingly, the diffracted electrons are used to obtain structural information.

Determination of interface ratio

With the knowledge of the Cu content it is possible to calculate the theoretical Cu surface area from average Cu particle sizes. As the Cu particles are more or less spherical the volume (V) as well as the surface area (A_O) of one particle can easily be calculated from its averaged diameter: $V = 1/6 \Pi d^3$, $A_O = \Pi \cdot d^2$. Thus, the surface area of one particle and the amount (z) of particles per gram catalyst add up to the theoretical (maximal) Cu surface area:

$$\text{Cu SA}_{\text{theo}} = A_O(\text{particle}) + z(\text{particle})\text{g}_{\text{cat}}^{-1} \tag{2.10}$$
$$= \pi d^2 \cdot \frac{wt\%\text{Cu}}{m(\text{particle})},$$

where the mass of one Cu particle is calculated from its volume and the density of Cu ($8.92\,\text{g/cm}^3$):

$$m(\text{particle}) = \rho \cdot V(\text{particle}). \tag{2.11}$$

The ratio of surface area exposed to gas (Eq. (2.12)) as well as the interface ratio (IFR, Eq. (2.13)) are resulting by comparison of the maximal (theoretical) Cu surface area with the one measured by N_2O-RFC (Chap. 2.3).

$$\text{Cu SA}_{expo} = \frac{\text{Cu SA}_{meas}}{\text{Cu SA}_{theo}} \tag{2.12}$$
$$\text{IFR} = 1 - \text{Cu SA}_{expo} \tag{2.13}$$

2.6 Other Characterization Methods

2.6.1 Nitrogen adsorption isotherm

The measurement of nitrogen adsorption isotherms at $-196\,°\text{C}$ is the typical method to investigate the surface area and porosity of solids. The sorption behavior of a material strongly depends on the pore size. The International Union of Pure and Applied Chemistry (IUPAC) gives the following classification of pores according to their inner diameter [60]: micropores $< 2\,\text{nm}$, mesopores $2-50\,\text{nm}$, and macropores $> 50\,\text{nm}$.

The sorption behavior of all three pore types strongly deviates from each other. Macropores are so wide that they act like flat surfaces, making adsorption equal to desorption. The sorption behavior in micropores, on the other hand, is dominated by the interactions between fluid molecules and pore walls, whereas in mesopores, additional to the fluid-wall interaction, an interaction between fluid molecules can occur.

BET surface area

The adsorption isotherm model of Brunauer, Emmet and Teller (BET) [61] is widely used as the standard procedure for the determination of the surface area of porous material. The effectiveness of the BET theory is that it enables an experimental determination of the number of molecules required to form a monolayer despite the fact that exactly one monomolecular layer is never formed. Typically, the BET equation is applied in the lineary form [62]:

$$\frac{p}{n^a(p^0 - p)} = \frac{1}{n_m^a C} + \frac{(C-1)p}{n_m^a C p^0},$$
(2.14)

where n^a is the amount adsorbed at the relative pressure p/p^0 and n_m^a is the monolayer capacity. A plot of $p/n^a(p^0 - p)$ versus p/p^0, the so called BET plot, yields a straight line usually in the range $0.05 \leq p/p^0 \leq 0.35$ of the isotherm [63].

To calculate the surface area, often called BET area, of the adsorbent from the monolayer capacity n_m^a (i. e. the number of adsorbed molecules in a complete monolayer), the knowledge of the average area A_x effectively occupied by an adsorbed molecule in the complete monolayer is required, as discribed by Equation (2.15), where N_A is the Avogadro constant.

$$S_t = A_x \cdot n_m^a \cdot N_A$$
(2.15)

The specific surface area can be calculated by deviding S_t by the sample weight. Nitrogen is generally considered to be the most suitable adsorptive for surface area determination and it is usually assumed that the BET monolayer is close-packed, giving $A_x(\mathrm{N_2}) = 0.162\,\mathrm{nm}^2$ at $-196\,°\mathrm{C}$ [60].

Pore size analysis

Pore sizes can be estimated using the nitrogen adsorption-desorption isotherm. The most popular method for size analysis of mesopores is the BJH method, named after Barett, Joyner and Halenda [64]. The model is a numerical integration method which is based on the assumption that the pores are shaped cylindrical. The typical procedure, detailed described in [63], uses either the adsorption or desorption branch of the isotherm. However, despite cases of pore blocking usually the desorption branch is used. Computation starts at a relative pressure p/p^0 of 0.97 down to a relative pressure of approximately 0.4. The BJH method considers an isotherm as a series of steps taking place while the pressure is decreased. The amount of adsorbate removed in each step represents the emptying of inner pores from liquid adsorbate as well as a film thinning process.

2.6.2 Thermogravimetric Analysis

In thermogravimetry (TG) the mass change of a substance is recorded as a function of temperature when a sample is subjected to a controlled temperature program in a controlled atmosphere [65]. Such an analysis relies on a high degree of precision in the measurement of three characteristics: weight, temperature, and temperature change. It is most often combined with a mass spectrometer and can provide information about decomposition temperatures, absorbed moisture content of the respective materials, the level of inorganic and organic components in the materials, and decomposition points of solvent residues.

In the differential scanning calorimetry (DSC) the differences of the heat flow of the sample and a reference compound are measured during a defined temperature program as a function of sample temperature. Simultaneous TG/DSC measures both heat flow and weight changes in a material as a function of temperature or time. The complementary information obtained allows differentiation between endothermic and exothermic events which have no associated weight loss (e.g., melting and crystallization) and those which involve a weight loss (e.g., degradation).

2.6.3 Photoelectron Spectroscopy

In x-ray photoelectron spectroscopy (XPS) x-ray photons from a laboratory source or a synchrothron storage ring excite core electrons from a sample to high energy states [56]. The core hole subsequently decays either through an Auger process or through photon emission (fluorescence). It is a surface sensitive method which is widely used for the investigation of the electronic structure of a sample. Within this thesis, XPS was used to determine the Cu:Zn ratio after reduction. The curve fitting of the Cu2p and Zn2p peaks was performed based with a mixed Gaussian/Lorentzian function and background subtraction was carried out by using the Shirley method. Quantitative calculations were performed using normalized Cu2p, Zn2p intensities, taking into account the photon-energy dependence of the atomic subshell photoionization cross sections [66].

3 Experimental

3.1 Materials

The metal nitrates and bases were supplied by different companies with purities around 99% ($Cu(NO_3)_2$ – Roth, $Zn(NO_3)_2$ – Fluka, $Al(NO_3)_3$ – Riedel-de-Häen, $Ga(NO_3)_3$ – Sigma Aldrich, $Cr(NO_3)_3$ – Fluka, NaOH – Riedel-de-Häen and Na_2CO_3 – Roth) and were used without further purifications. Deionized water was taken from a Millipore water treatment system (MilliQ). For the microemulsion synthesis cyclohexane was supplied by Roth with a purity of 99.9 %. The surfactant Marlipal O13/40 ($C_{21}H_{44}O_5$) is a non-ionic surfactant of the alkyl polyglycolether type with a mean ethoxylation degree of four and was supplied by Sasol (Marl, Germany) with a purity of 98 %.

3.2 Co-Precipitation of LDH compound

LDH precursors were precipitated from a $Cu^{2+}/Zn^{2+}/Al^{3+}$ nitrate solution (total metal concentration: 0.43 M; $Cu : Zn : Al = 50 : 17 : 33$) with an aqueous solution of NaOH (0.3 M) and Na_2CO_3 (0.045 M) as the precipitating agent. The reaction was carried out at a constant pH value (pH = 8 ± 0.7) at 25 °C – pH and temperature were controlled by the automated lab reactor system (Labmax from Mettler Toledo) (see Fig. 3.1).

After an ageing time of one hour the blue powder was isolated by filtration, washing and drying at 100 °C for 13 h. In case of the promoter study (Chap. 6) Al was substituted stepwise by Cr (label: CrX) or Ga (label: GaX) gaining two sample series with Cu,Zn,Al-LDH (label: CZA) as crossing point (in the labels X is the at% of the substituting element).

(a)   (b)
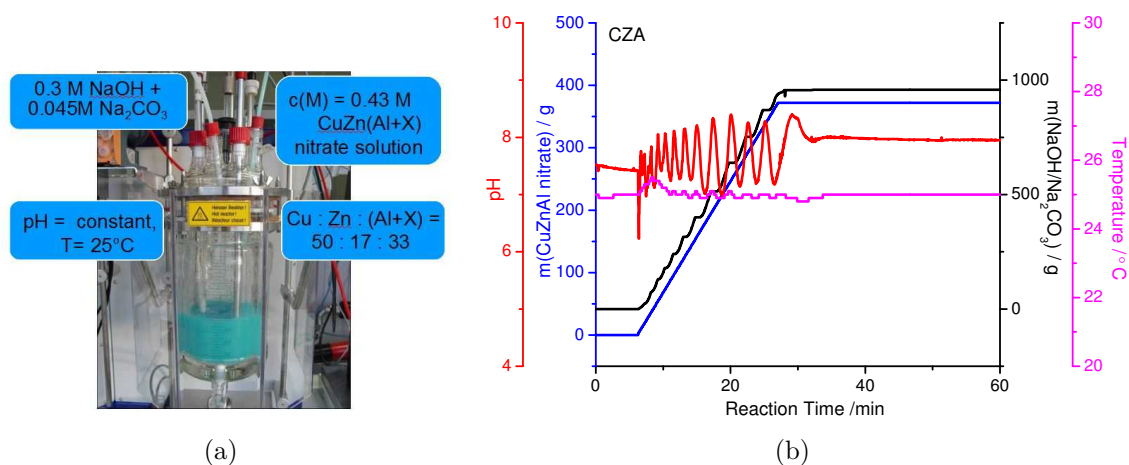
Figure 3.1: Co-precipitation and ageing: (a) in an automated laboratory reactor system (labmax), (b) protocol of co-precipitation (Labmax).

All precursor sample were afterwards calcined in air at $330\,°C$ for $3\,h$ (heating rate $2\,K/min$). Finally, the Cu based catalyst was obtained by reduction of the calcined sample in $5\,\%$ H_2/Argon and a heating rate of $6\,K/min$. The reduction temperature was adjusted for each catalyst to $15\,°C$ above T_{max} of the TPR profiles.

3.2.1 LDH synthesis from microemulsion

The microemulsions were prepared by mixing cyclohexane and the surfactant in a glass flask and adding either water or the salt solution. For the base solution it needed approximately $12\,h$ until stable microemulsions were formed. Just for practical reasons the microemulsion synthesis of the Cu,Zn,Al-hydrotalcite was carried out with just one microemulsion: A microemulsion ($\gamma = 0.25$, 8% H_2O) of the aqueous solution of NaOH ($0.3\,M$) and Na_2CO_3 ($0.045\,M$) was provided with the use of cyclohexane and the surfactant Marlipal O13/40. The reaction was carried out at a constant pH value (pH $= 8 \pm 0.7$) at $30\,°C$ – pH and temperature were controlled by an automated lab reactor system (Labmax from Mettler Toledo). By constant dosing of the aqueous Cu^{2+}/Zn^{2+}/Al^{3+} nitrate solution (Cu:Zn:Al $= 50{:}17{:}33$, total metal concentration: $c(M) = 0.43\,M$) together with the basic microemulsion to a template water-in-oil microemulsion the hydrotalcite was formed within the water droplets. The product was isolated by centrifugation, washing with acetone and drying at $100\,°C$ for around $15\,h$. Upon calcination in air at $330\,°C$ for $3\,h$ the blue-green

hydrotalcite was converted into the dark green mixed oxide. The Cu based catalyst was obtained by reduction of the oxidic sample in 5% H_2/Argon (6 K/min).

3.3 Conventionally prepared reference catalyst

The reference $Cu/ZnO/Al_2O_3$ catalyst is a laboratory reproduction of the industrial system conventionally prepared according to the industrial recipe from zincian malachite, $(Cu,Zn)_2(OH)_2CO_3$, which was developed by in the 1960s [7, 8]. Within this thesis the calcined state (labeled conv-calc) as well as the reduced state after reduction in hydrogen at 250 °C (labeled conv-red) are investigated.

3.4 Synthesis of Zn,Al spinel as reference material

Analogous to Valenzuela et al. [67] the synthesis of $ZnAl_2O_4$ spinel was done by co-precipitation of Zn and Al nitrate solution ($Zn : Al = 1 : 2; \approx 0.1\,M$) with 0.6 M NaOH solution at pH 7.5 at 25 °C (controlled by Labmax system). After filtration and washing the solid was dried and calcined in air at 800 °C for 8 h.

3.5 Catalyst characterization

The choice of the precipitation pH was based on titration curves measured with an automated titrator (Mettler Toledo). For that 10 mL of the original nitrate solution (concentration of the metals as used in catalyst synthesis) were diluted with 20 mL water. This diluted solutions were acidified with 2-3 drops of 65% HNO_3 to start from pH ≈ 1 and were titrated at 25 °C with the basic mixture of 0.15 M NaOH and 0.025 M Na_2CO_3.

The dynamic light scattering (DLS) measurements for droplet and particle size distributions within the study of microemulsion synthesis (Chap. 5) were carried out using a Malvern ZetaSizer NS.

For the determination of the elemental composition x-ray fluorescence anaylsis (XRF) measurements were performed in He-atmosphere on a Sequential Pioneer S4 Spectrometer (Bruker) and the K lines were analyzed. For the evaluation of the measured data corresponding mixtures of the metal oxides were prepared as

calibration standards. In case of the products obtained by microemulsion (Chap. 5) the average composition of the precipitates was determined by ICP-MS (inductively coupled plasma mass spectroscopy).

X-ray diffraction (XRD) patterns were recorded on a STOE Stadi-P diffractometer in transmission geometry using Cu Kα_1 radiation, a primary Ge monochromator and a 3° linear position sensitive detector. Most XRD pattern were recorded in the 2θ range $4-80°$.

The BET surface areas of precursor and calcined sample were determined by measuring the nitrogen adsorption-desorption isotherms with a Quantachrome Autosorb automatic BET-sorptometer at $-196\,°$C with nitrogen as the analysis gas. Prior to the analysis, the samples were outgased for $2\,$h at $100\,°$C.

TG analyses were performed on a Netzsch STA449 thermobalance. Evolution of gas phase during reaction was monitored with a quadrupole mass spectrometer (Pfeiffer, QMS200 Thermostar). For the calcination experiment the precursor was heated in synthetic air with $2\,$K/min to 700 or $1000\,°$C. The reduction behavior was observed during heating in $5\,\%$ hydrogen with $5\,$K/min to $500\,°$C.

IR spectra were collected on a FTIR Perkin Elmer 2000 using the KBr disc technique.

Calcined samples were reduced in $5\,$vol$\,\%$ H$_2$ in Ar at a heating rate of $6\,$K/min ($80\,$mL/min, end temperature $350\,°$C, holding time $30\,$min) by temperature programmed reduction (TPR) in a fixed bed reactor (TPDRO-1100, CE instruments). The H$_2$ consumption was monitored with a TCD. Sequential temperature programmed reduction (TPR) and oxidation (TPO) studies have been conducted on the same instrument (CE Instruments). The temperature was increased linearly to $330\,°$C with a heating ramp of $6\,$K/min and maintained isothermal for $30\,$min at $330\,°$C (hydrogen flow conditions see TPR). Subsequent temperature programmed re-oxidation of the reduced samples (TPO) was performed by heating up to $330\,°$C with a rate of $6\,$K/min under a flow of $5\,\%$ O$_2$ in He ($50\,$mL/min), and held at $330\,°$C for $3\,$h to maintain a complete oxidation. This temperature program during re-oxidation was similar to the calcination performed. Analogous to TPR for TPO the oxygen consumption was measured by a TCD.

The copper surface area (Cu SA) was determined in the same machine using the principle of N$_2$O reactive frontal chromatography (N$_2$O-RFC) [51]. The experiments were carried out at $30\,°$C to avoid subsurface oxidation [52]. A stainless-steel micro-

reactor was used, which had an inner diameter of 4 mm and was filled with 95 mg of the sieve fraction ($100 - 200\,\mu$m). The measurement was started by switching from pure He to 1 vol.-% N_2O in He (Westafalen) by means of a four way valve. The amount of evolved N_2 upon decomposition of N_2O at the Cu(0) surface was monitored with a mass spectrometer (Pfeiffer, QMS Omnistar). Prior to each experiment the catalysts were reduced in hydrogen according to the reduction treatment described above (catalyst preparation Chap. 3.2).

In situ X-ray absorption and photoelectron spectroscopies (XAS and XPS, respectively) were performed at ISISS beamline at BESSY II in Berlin, in a setup described elsewhere [56, 68]. About 15 mg of calcined catalyst powder were pressed forming a ca. 0.5 mm thick and 8 mm diameter pellet and placed on a sample holder, which could be heated from the rear by an IR laser (cw, 808 nm). The temperature was measured by a K-type thermocouple fixed on the sample surface and the heating rate was 2 K/min. The H_2 gas flow into the reaction cell was controlled using mass flow controllers and leak valves. A differentially pumped quadrupole mass spectrometer (Balzers) was connected through a leak valve to the experimental cell and the gas phase composition was monitored by on-line mass spectrometry, while simultaneously characterizing the surface by XPS or XAS. The soft X-ray absorption spectra of the Cu L3 and Zn L3 edges were recorded in the TEY mode during heating in hydrogen. XAS peaks of Cu were fitted using line shapes recorded on reference samples (Cu, Cu_2O, CuO). Photoemission spectra were recorded after reduction at stationery conditions. For the calculations all spectra were normalized by the storage ring current and the energy-dependent incident photon flux, which was measured prior to the measurements using a gold foil with known quantum efficiency. The binding energy (BE) scale was calibrated with respect to the Fermi level of the electron analyzer.

In-situ XRD measurement was performed on a STOE Theta/Theta diffractometer (Cu-Kα radiation, secondary monochromator, scintillation counter) operating at 50 kV and 30 mA in a reflection scan mode. The diffractometer was equipped with a *Paar* XRK 900 high temperature cell. The calcined catalyst precursor was used for in situ measurements. The XRD pattern was recorded after reduction in 5 % H_2 at 300 °C (2 K/min) in the 2θ range $20 - 100°$.

SEM images were taken in a Hitachi S-4800 (FEG) system. A Philips CM200FEG microscope operated at 200 kV and equipped with a field emission gun and the

Gatan imaging filter was used for TEM. The coefficient of spherical aberration was Cs = 1.35 mm. The information limit was better than 0.18 nm. High-resolution images with a pixel size of 0.016 nm were taken at the magnification of 1'083'000x with a CCD camera, and selected areas were processed to obtain the power spectra (square of the Fourier transform of the image), which were used for measuring inter planar distances ($\pm 0.5\,\%$) and angles ($\pm 0.5°$) for phase identification. Prior to TEM measurements (expect for the investigation of calcined material) the reduced samples were transfered to a glove box immediately after the reduction procedure to prevent an exposure to air. Afterwards, the samples were dispersed in acetone and deposited on a vacuum TEM transfer sample holder.

3.6 Testing for catalytic activity

Methanol synthesis was carried out in a fixed bed micro reactor with an inner diameter of 2 mm filled with 180 mg of the sieve fraction ($100 - 200\,\mu$m). Prior to the activity measurements, the samples were activated by reduction in H_2. The samples were first treated for 12 h in a mixture of $5\,\%$ H_2 in He at 200 °C using a heating rate of 0.3 K/min and then for 4 h in pure H_2 at 250 °C. Methanol synthesis was performed at total pressure of 60 bar at different temperatures. The synthesis gas was composed of $72\,\%$ H_2, $10\,\%$ CO, $4\,\%$ CO_2 and balanced by He. Total flow was kept at 60 mL/min by mass flow controllers. Methanol synthesis activity was measured under steady state conditions. Therefore, the sample has been aged for 48 h at 250 °C at 60 bar. Afterwards, steady state activities were determined for each temperature (250 °C, 210 °C, 250 °C, 210 °C) after 24 h on stream by on-line GC analysis (Varian MicroGC 4900) equipped with a TCD using a PPU column, a COx column, and a molsieve 5 Å column for separating polar products, such as water, methanol, CO_2 and CO. The results are given in weight time yield (WTY) of methanol.

In case of the catalyst obtained by microemulsion (Chap. 5) the catalytic activity was tested in the methanol steam reforming reaction ($CH_3OH + H_2O \longrightarrow CO_2 + 3\ H_2$) within a plug-flow reactor system (PID Eng & Tech, $CH_3OH : H_2O = 1 : 1$) using a GC (CP 4900, Varian, columns: molsieve, PPU) for product analysis. The educt gas mixture contained nitrogen as a carrier gas and helium as an internal standard to

calibrate the gas volumes, because unconverted water and methanol were removed prior to the GC using a cooling-trap and a Nafion membrane. A sieve fraction of $100 - 200\,\mu\mathrm{m}$ of the calcined samples was diluted with $200\,\mathrm{mg}$ of inert graphite. Both samples were reduced in hydrogen ($12\,\mathrm{h}$ at $180\,^\circ\mathrm{C}$ and $3\,\mathrm{h}$ at $260\,^\circ\mathrm{C}$) before starting the steam reforming reaction which was carried out at $260\,^\circ\mathrm{C}$. Conversion of methanol was calculated using the amount of formed carbon oxides. Selectivity of CO_2 was defined as $CO_2/(CO_2 + CO)$ – CO was most likely produced by reverse WGS reaction.

4 Microstructure of Cu,Zn,Al LDH material and resulting catalyst

For understanding the role of Cu,Zn,Al LDH in industrial applied catalysts the preparation history of the resulting catalyst is investigated carefully starting from the synthesis of the LDH precursor phase. As described in Chapter 1.3 a nominal composition $Cu:Zn:Al = 50:17:33$ was used for the preparation of the nitrate solution.

4.1 Choice and influence of precipitation pH

For the simultaneous precipitation of all metal components the precipitation pH has to be higher than the one of each component – so called constant pH co-precipitation. To choose the pH for the present system, precipitation curves were recorded at $25\,°C$ using the increasing pH titration (see Chap. 3.5) [69]. To decrease the complexity of the ternary system, the precipitation of pure Cu nitrate solution, Cu,Zn nitrate solution, Zn,Al nitrate solution and, finally, Cu,Zn,Al nitrate solution with a basic mixture of NaOH and Na_2CO_3 were investigated, using the concentration of the metals as used in catalyst synthesis.

It has to be mentioned that a titration of precipitation is dominated by gradients of the formed solids, which are not controlled under titration conditions. In the present system all titration curves (Fig. 4.1) are more or less characterized by the S-shaped neutralization of HNO_3 at pH 7, which was added to start below pH 2. Increasing the complexity of the investigated solutions the precipitation pH of Cu, Zn and Al can be analyzed. The precipitation of gerhardtite $Cu_2(OH_3)NO_3$ [69] takes place around pH 4.5 leading to an interruption of the neutralization curve with a plateau (see Fig. 4.1(a)). The titration of the Cu,Zn solution (Fig. 4.1(b)) showed that Zn

is precipitating at pH 6.5. According to the titration curve of the Zn,Al solution
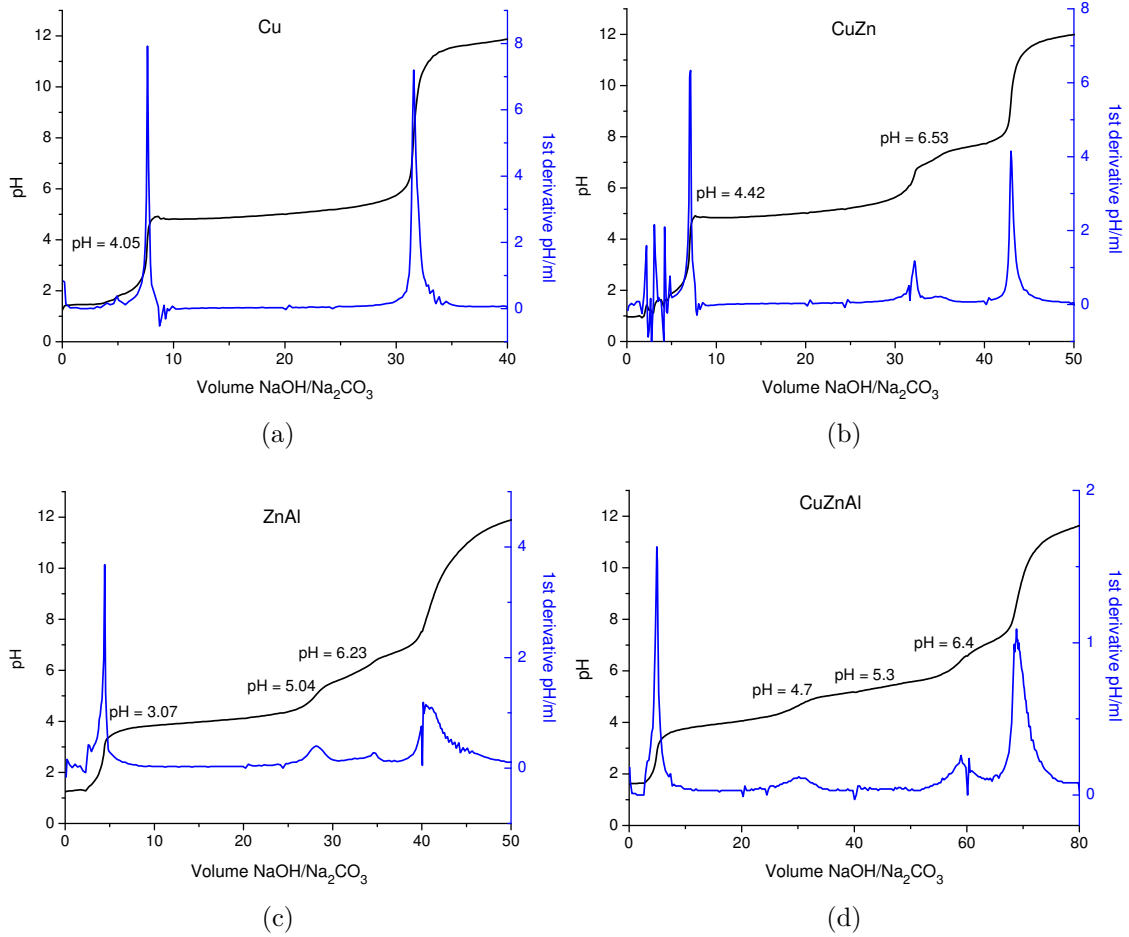
Figure 4.1: Titration curves of (a) pure Cu solution, (b) mixed Cu,Zn solution, (c) mixed Zn,Al solution, and (d) mixed Cu,Zn,Al solution titrated at $25\,^{\circ}\mathrm{C}$ with NaOH/Na$_2$CO$_3$.

(Fig. 4.1(c)), Al is precipitating around pH 5. The first pH jump probably belongs to the well known olation process of Al-species [69]. Within the titration curve of the ternary solution (Fig. 4.1(d)), the precipitation of Al is not distinguishable from the precipitaion of Cu and Zn. But nevertheless, the pH of the co-precipitation of Cu,Zn and Al by NaOH and Na$_2$CO$_3$ to form a LDH structure is necessary to be above 6.5. The step-like shape of the precipitation curve indicates that also in the ternary solution all three components are solidified seperately with increasing pH and that the formation of a ternary LDH is a secondary process. Consequently, the precipitation of defined LDH material is necessary to perform with constant pH.

To investigate the influence of the synthesis pH on the properties of the LDH precursor and the final catalyst, four samples were prepared with different pH values, labeled as pH7-LDH, pH8-LDH, pH9-LDH, pH10-LDH. In general, a low pH is desired to favor olation (formation of bridging -OH) over oxolation (formation of bridging -O). On the other hand, it has to be high enough to ensure the complete precipitation of all elements. From the titration curve of the ternary solution (Fig. 4.1(d)) pH 8 was suggested to fulfill these conditions, pH7-LDH to countercheck the obesrvation. The XRD patterns in Figure 4.2 show that all four pH values resulted in precursors with hydrotalcite-like structure reported for a sample $Cu_3Zn_3Al_2(OH)_{16}CO_3 \cdot 4H_2O$ (ICSD 37-629) [26].
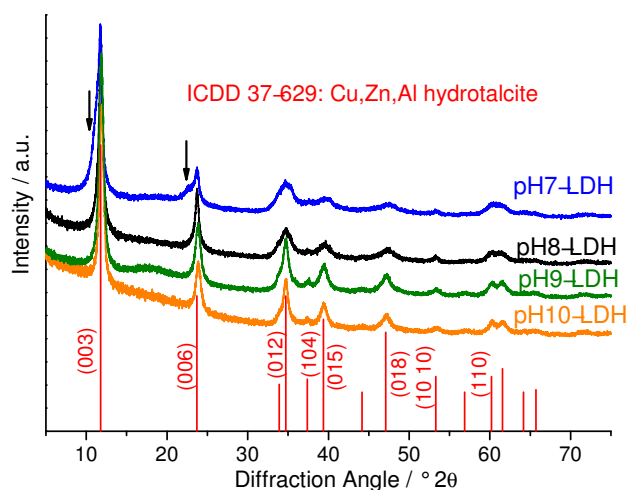
Figure 4.2: XRD patterns of Cu,Zn,Al LDH precursors precipitated at different pH values.

As already mentioned (Chap. 2.1), a typical diffractogram of a LDH compound consists of sharp basal reflections at small values of 2θ corresponding to successive orders of the interlayer spacing [18]. Additionally, relatively weak non-basal reflections are present at higher angles. The spacing is mainly controlled by the size and concentration of the anions in the interlayer space (see also Fig. 1.4 in Chap. 1.2). Accordingly, from the observed decreasing $d(00l)$-values, shown in Figure 4.3(a), a decreasing interlayer distance with increasing pH can be concluded (compare Chap. 2.1). As illustrated by Figure 4.3(b) (sections of IR spectra), this finding is explainable by the decreasing amount of nitrate present in the interlayer of the LDH for increasing pH. As nitrate needs more space than carbonate (compare Fig. 1.4 in
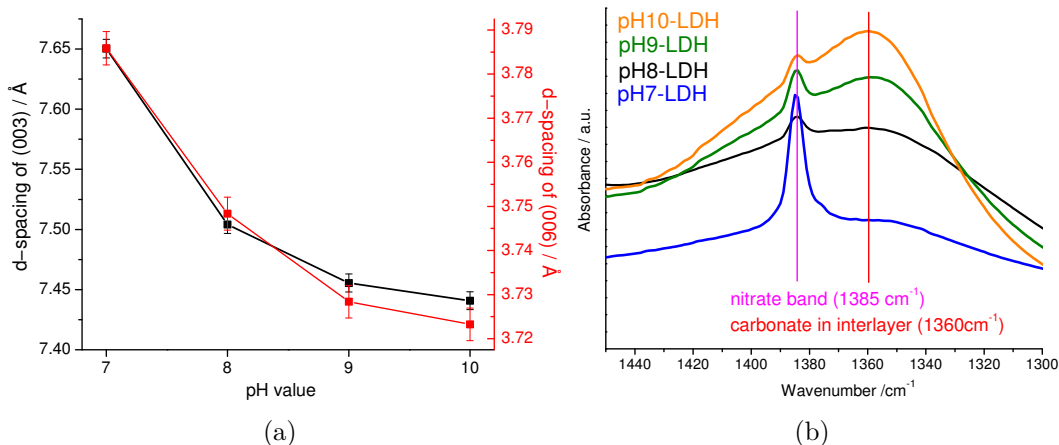
Figure 4.3: Characterization of pH series: (a) XRD peak analysis: d-spacing and accordingly interlayer distance decreases with pH, (b) extract of IR-spectra: the lower the pH the more NO_3^- included in interlayer.

Chap. 1.2) pH7-LDH is characterized by the high interlayer space observed. According to the XRD pattern of pH8-LDH, pH9-LDH and pH10-LDH the presence of nitrate does not result in additional phases besides hydrotalcite. Conversely to pH7-LDH where changes in the (00l)-reflection profiles (shoulder at the low angle side, see arrows in Fig. 4.2) are indicating the presence of a second LDH phase.

Table 4.1: Properties of precursor and calcined samples of the pH series: metal contents determined by XRF of calcined samples (nominal composition: $Cu : Zn : Al = 50 : 17 : 33$) – deviances for all samples: Cu ± 0.08, Zn ± 0.04 and Al ± 0.04; particle size of precursors determined by SEM (range of PSD: max - min particle size); BET surface area of precursors and calcined samples (3 h at 330 °C).

Sample	M content /mol%			Particle Size /nm		SA_{BET} /m^{2}g^{-1}	
	Cu	Zn	Al	mean	range of PSD	prec	calc
pH7	50.9	14.6	34.5	77	169	4	35
pH8	50.7	15.6	33.7	65	91	89	81
pH9	50.4	16.5	33.1	71	115	78	75
pH10	50.15	16.4	33.4	88	143	65	65

The composition, measured by XRF, was just slightly influenced by the pH, where pH 7 resulted in the highest deviance from the nominal composition (see Tab. 4.1), which was used to prepare the starting solution. Evaluation of SEM images resulted in the smallest particles and narrowest particle size distribution (PSD) for pH8-LDH,

which has as well the highest BET surface area (SA) (Tab. 4.1). On the other hand, pH9-LDH showed similar surface area and particle sizes but a slightly broader PSD. pH 10 resulted in the biggest particles and broader PSD, whereas for pH7-LDH smallest surface area and most inhomogeneous PSD were found, which makes it again unfavourable.

Additional to the findings of XRD, SEM, XRF and BET, the reduction behavior of the sample prepared at pH7 (in this case pH7-calc) is changed significantly (Fig. 4.4) indicating again a high inhomogeneity of this material. On the other hand, the TPR
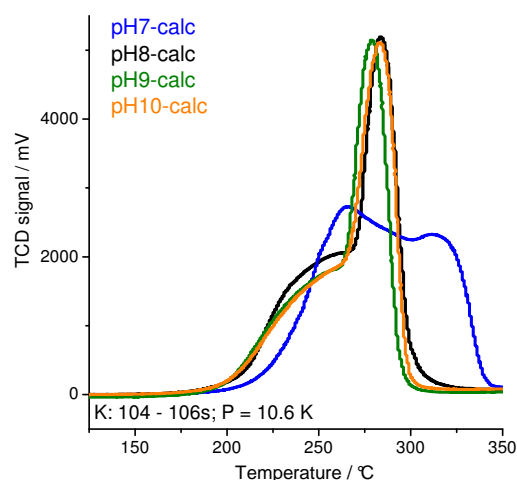
Figure 4.4: TPR profiles of Cu,Zn,Al catalysts resulting from LDH precursors precipitated with different pH values.

profiles of pH8-calc, pH9-calc and pH10-calc (calcined at $330\,^\circ$C for $3\,$h) are quite similar, only the reducibility (i.e. the fraction of reduced CuO) is slightly influenced (Tab. 4.2). A detailed analysis of the TPR of the Cu,Zn,Al ex-LDH system can be found in Chap. 4.3. To characterize the active phase of the catalysts the Cu surface area was measured by N_2O-RFC resulting in the highest value for the catalyst prepared at pH 9 (see Tab. 4.2).

All applied analytics have shown that a precipitation at pH 7 results in inhomogeneity in structure and particle sizes, as well as a small surface area, nicely proving that a higher basicity is necessary. Furthermore, considering that pH 8 resulted in a LDH structure with high homogeneity in elemental distribution, higher interlayer space, and smallest particles with narrowest PSD compared to pH 9 and 10, as well as a high reducibility, pH 8 was used as standard condition for all syntheses of the

Table 4.2: Results of TPR and N$_2$O RFC of pH variated samples: CuO reduced determined by calibration using bulk CuO; n.m.: not measured.

Sample	CuO reduced /%	Cu-SA /m^{2}g^{-1}
pH7-calc	96	n.m.
pH8-calc	98	7.2 ± 0.7
pH9-calc	85	8.3 ± 0.8
pH10-calc	84	7.5 ± 0.75

Cu,Zn,Al system, despite the fact that pH 9 resulted in the highest copper surface area.

4.2 Characterization of Cu based LDH and materials after calcination

4.2.1 XRD, SEM and BET of precursor material

After choosing the precipitation pH, this LDH as well as the calcined material were characterized in detail. Throughout this thesis pH8-LDH (synthesized at 25 °C) is called CZA. As already mentioned above, the product of the co-precipitation at pH 8 has a hydrotalcite-like structure (Fig. 4.2) – no other crystalline phase was detected. By SEM the expected platelet-like morphology of LDH compounds was observed, as presented in Figure 4.5, with an average particle size of 65 nm.

(a)   (b)
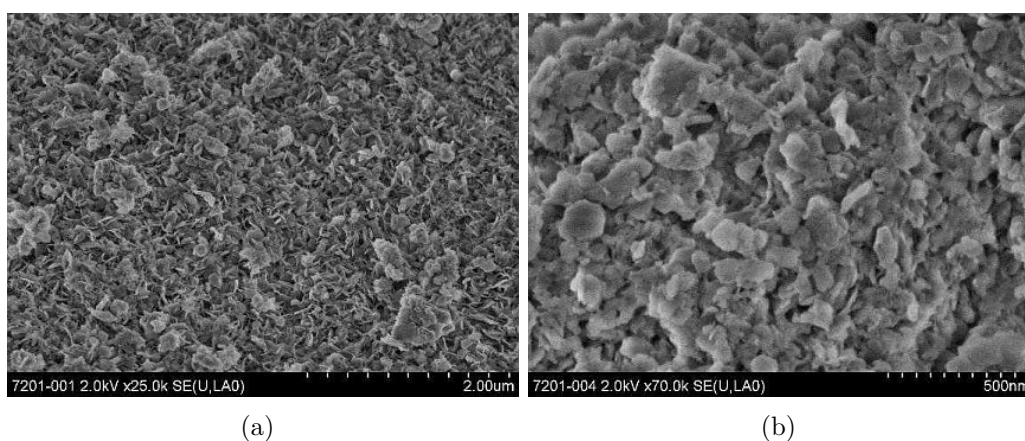
Figure 4.5: SEM images showing typical platelet-like morphology of LDH.

(a)

(b)

(c)

(d)

(e)
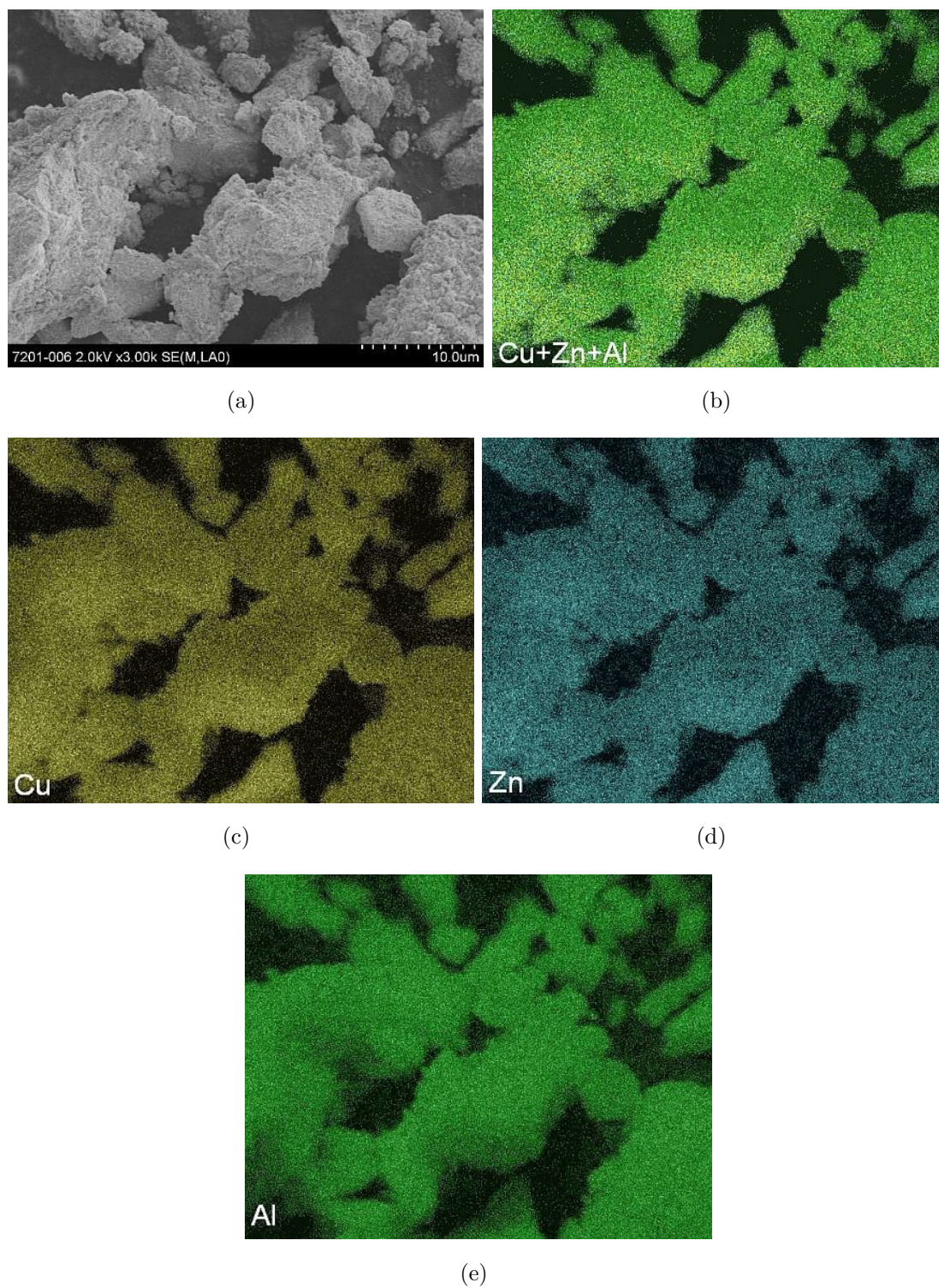
Figure 4.6: Elemental mapping of CZA by SEM (a) SEM image, (b) overview of distribution, (c) Cu, (d) Zn, (e) Al.

Furthermore, the homogeneous distribution of Cu, Zn and Al was proven by elemental mapping, presented in Figure 4.6.

The adsorption behavior of the sample was investigated by N_2 physisorption. According to IUPAC (International Union of Pure and Applied Chemistry) [60], the isotherm of CZA is a type IV isotherm (Fig. 4.7(a)), which is typical for mesoporous materials. The initial part of the isotherm is dominated by monolayer adsorption (Langmuir type), followed by multilayer adsorption starting at a certain pressure. Characteristic for this isotherm is the presence of the hysteresis loop, which is associated with the occurrence of pore condensation. Also according to IUPAC classification [60], CZA is characterized by a type H1 hysteresis which can be associated to particles with well-defined cylindrical pore channels or to agglomerates of uniform particles [63]. Considering the (uniform) platelet-like morphology observed by SEM, LDH compounds are not characterized by pores but by spaces between the platelets where multilayer adsorption and, finally, "pore" filling can occur. As a mono-modal distribution curve (see Fig. 4.7(b)) was determined applying the BJH model (see Chap. 2.6.1) a homogeneous distribution of the spaces between the platelets can be assumed with an averaged distance of 25 nm.

(a)   (b)
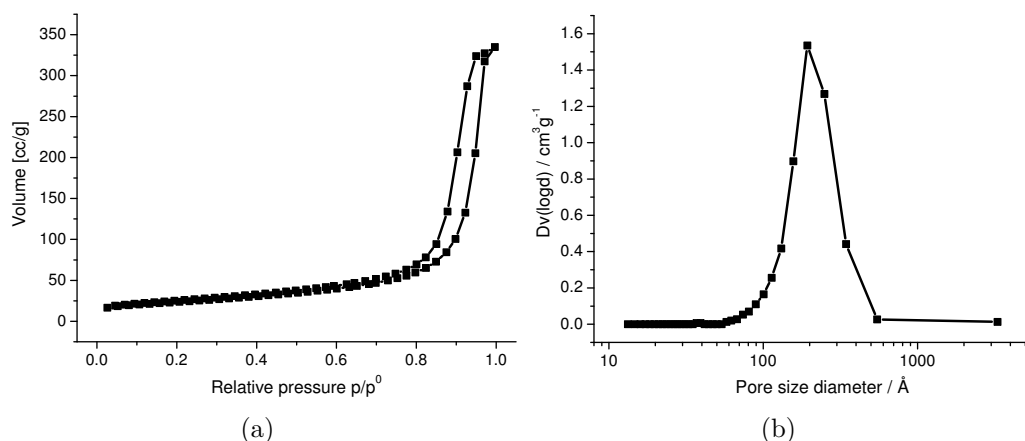
Figure 4.7: Nitrogen adsorption-desorption results: (a) adsorption-desorption isotherm measured at $-196\,°C$, (b) mono modal "pore" size distribution.

The thermal behaviour of the catalyst precursor samples was investigated by thermogravimetric measurements in synthetic air coupled with mass spectrometry (MS). In general, the typical 3-step decomposition of LDH compounds [19] was observed (see Fig. 4.8): i) loss of surface water molecules around $70\,°C$, (ii) evaporation
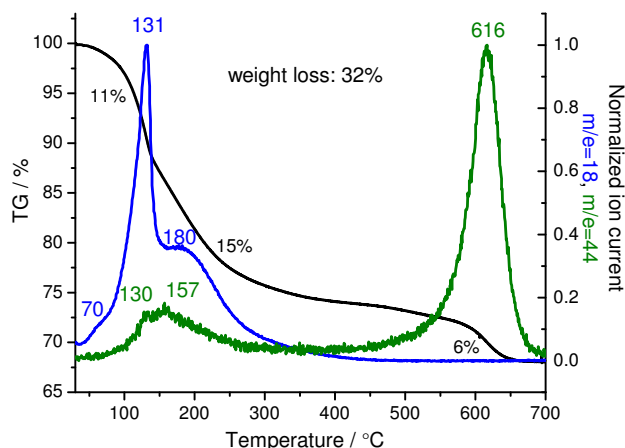
Figure 4.8: Weight loss and MS traces (blue = H_2O and green = CO_2) of LDH compound during heat treatment.

of interlamellar water molecules between 100 °C and 140 °C, (iii) dehydroxylation of the brucite-layer and loss of carbonate of the interlayer space between 130 °C and 220 °C. Additionally, CO_2 formation at higher temperatures was observed, which is attributed to the stabilizing, strongly bounded, (so called) high temperature carbonate (HT-CO_3^{2-}), which is well known for Cu based catalysts [14, 70]. The overall weight loss adds up to 32 %, 6 % belonging to the HT-CO_3^{2-}. The fraction of carbonate being decomposed at high temperature is calculated to 70 % from the ratio of the areas under the two MS peaks at m/z 44. In agreement to earlier results [29], the dehydroxylation and decarboxylation of the hydrotalcite is completed around 330 °C.

4.2.2 Characterization of calcined material

To complement these data, the precursor was calcined at different temperatures resulting in the XRD patterns shown in Figure 4.9. As can be seen, the LDH structure partially still exists after calcination at 200 °C (see Fig. 4.9(a)), where the shift of the (003) reflection to higher angles indicates a decrease of the interlayer space due to the emission of interlayer water and starting decarboxylation. During dehydroxylation and decarboxylation, at a calcination temperature of 260 °C, the LDH structure collapses leading to nearly X-ray amorphous material, which can be described as an amorphous carbonate-modified mixed CuZnAl oxide. The oxide
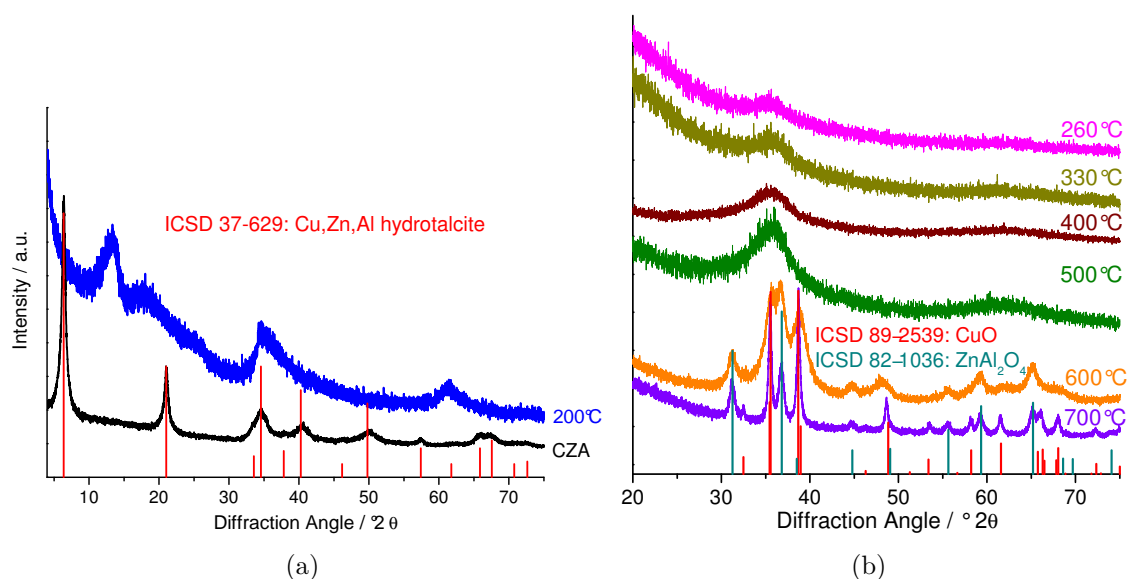
Figure 4.9: XRD patterns of CZA after calcination at different temperatures. (a) At 200 °C the LDH structure is partially still present. (b) The final product after calcination at 700 °C can be identified as a mixture of CuO (red, ICSD: 89-2529 [71]) and $ZnAl_2O_4$ (dark green, ICSD: 82-1036 [72]).

phases do not crystallize until the decarboxylation step (HT-CO_3^{2-}) at temperatures above 500 °C. Calcination at 600 °C leads to the formation of CuO (ICSD: 89-2529 [71]) and spinel-type $ZnAl_2O_4$ (ICSD: 82-1036 [72]). After calcination at 700 °C no clear indication of the presence of crystalline ZnO besides $ZnAl_2O_4$ can be found. It can be seen in the SEM images, shown in Figure 4.10, that the general platy morphology was maintained during calcination until higher temperatures where crystallization occurs (above 500 °C). Even after heating up to 700 °C, the platelets can be vaguely discerned.

As was shown by TG-MS and XRD the dehydroxylation and decarboxylation of the brucite layers is finished around 330 °C, accordingly, this temperature is used as calcination condition for CZA for further investigations towards the final catalyst, applying a heating rate of 2 K/min and a holding time of 3 h. The calcination product is labeled as CZA-calc in the following. This temperature is also in accordance with calcination treatments applied in literature for Cu based catalysts [14, 73].

CZA-calc as starting point for further reduction treatments is a, so called, carbonate-modified mixed CuZnAl oxide and characterized by its nearly amorphous structure
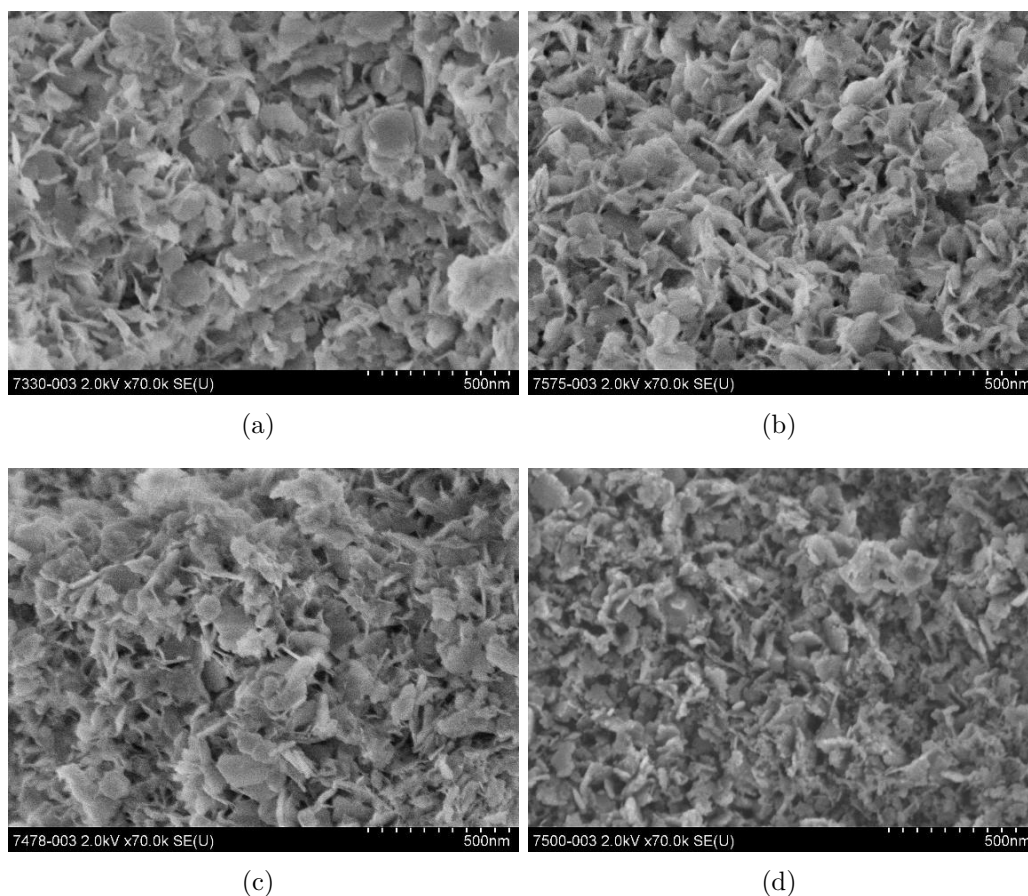
Figure 4.10: SEM images of CZA after calcination at different temperatures: (a) 330 °C, (b) 400 °C, (c) 500 °C, (d) 700 °C.

and the platy morphology, as shown in Figure 4.9(b) and Figure 4.10(a) respectively. It still contains $8\,\text{wt}\%$ HT-CO$_3^{2-}$ (compare Fig. 4.8: $6\,\text{wt}\%$ relative to LDH precursor) and has a BET surface area of $81\,\text{m}^2/\text{g}$ (Tab. 4.1 pH8). The calcination had no influences on the homogeneity of the elements (see Appendix A.1 Fig. A.3) and the nitrogen adsorption-desorption isotherm type and porosity (see Fig. A.1(a) in Appendix A.1), whereas the averaged distance between the platelets of $29\,\text{nm}$ is just slightly increased compared to CZA. In general, it is expected for LDH compounds to increase their surface area upon calcination [19]. The constant adsorption-desorption behavior observed for CZA-calc compared to CZA, is probably caused by the formation of HT-CO$_3^{2-}$. Thus, in agreement with the high decomposition temperature of the HT-CO$_3^{2-}$ a strong interaction of the Cu phase with the Zn-Al matrix can be

(a)   (b)
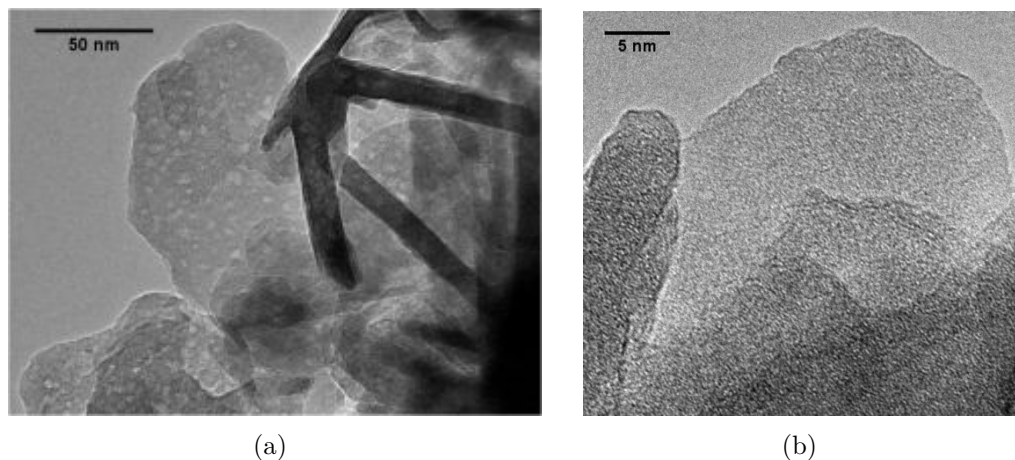
Figure 4.11: TEM investigation of CZA-calc: The material consists of amorphous platelets.

concluded. By TEM, images depicted in Figure 4.11, no indication for crystalline phases was found. Furthermore, no separation of Cu and Zn-Al oxide was observed, thus the elemental composition is completely homogeneous.

Comparing these results to a conventionally prepared reference catalyst (see Chap. 3.3), the differences are quite obvious. The conventionally prepared catalyst in the calcined state is characterized by crystalline particles of CuO in needle-like morphology well separated from ZnO and Al_2O_3 (see Appendix A.2 Fig. A.8) thus the phase separation already occurred during calcination.

Investigation of oxide matrix

On the basis of our previous study the formation of $ZnAl_2O_4$ in spinel-like structure during calcination was expected for a Zn : Al ratio of 1 : 2 [29], at least locally. As reference material phase-pure $ZnAl_2O_4$ spinel (see XRD pattern in Fig. A.2 in Appendix A.1) was synthesized by co-precipitation (Chap. 3.4).

NEXAFS of ZnL_3 edge was measured to investigate the near-surface structure of CZA-calc. The information depths for transition metal oxides with TEY is estimated to approximately 4 nm [57] in comparison to the platelet thickness of $5 - 20$ nm (compare Fig. 4.11). The obtained NEXAFS spectrum is depicted in Figure 4.12 in comparison to the reference $ZnAl_2O_4$ spinel as well as the conventionally prepared catalyst precursor (conv-calc). The differences between the oxide structure of the
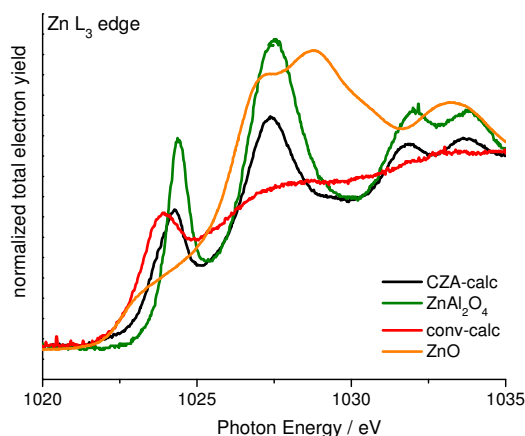
Figure 4.12: NEXAFS spectra of Zn L$_3$ edge of CZA-calc and conv-calc compared to reference spectra of phase pure ZnAl$_2$O$_4$ and ZnO.

conventionally prepared reference system and CZA-calc are quite obvious as the latter has a pronounced fine-structure, indicating a well ordered and homogeneous oxide matrix. Furthermore, by comparison with the spectrum of ZnAl$_2$O$_4$, the spinel structure is clearly proven to be present in the ex-LDH compound.

4.3 Investigation of reduction behavior in comparison with conventionally prepared catalyst

4.3.1 TPR and XAS investigations

Figure 4.13 compares changes in the thermal conductivity of the flowing gas phase (proportional to the hydrogen consumption) during TPR of CZA-calc and a conventionally prepared CuO/ZnO/Al$_2$O$_3$ precursor (conv-calc), which was obtained from a hydroxycarbonate phase mixture after co-precipitation (see Chap. 1.1.1).

First, the whole reduction process occurs at higher temperatures for the ex-LDH catalyst. As shown in Figure 4.11 "CuO" is completely distributed within the Zn-Al-oxide matrix. This strong contact has to be broken before reduction. It is likely to see this interaction as Cu^{2+} ions which are bridged through O^{2-} anions to ZnAl$_2$O$_4$, as similarly described in [74]. Upon heating in hydrogen, the well dispersed Cu^{2+} cations separate from the Zn-Al-oxide matrix, form clusters and finally start
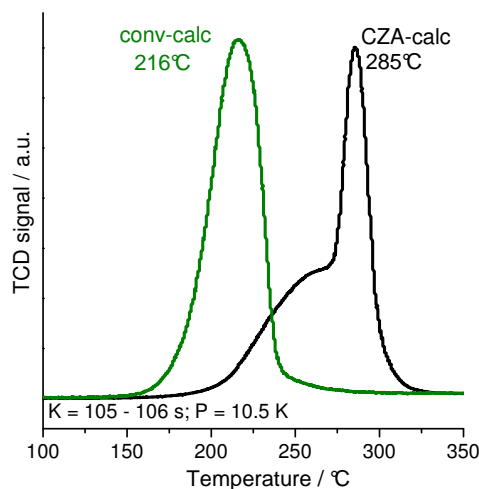
Figure 4.13: Reduction profile of CZA-calc in comparison to conv-calc, measured with a heating rate of 6 K/min.

to reduce. Thus, during reduction of CZA-calc the controlled separation of reducible and irreducible species leads to the pronounced shift of the reduction temperature.

The apparent activation energy for the catalyst reduction was derived by measuring the displacement of the temperature of the highest reduction rate T_{max}, so called maximal reduction temperature, in the corresponding TPR profile in dependence of different heating rates (1, 2, 4, 6, 8, and 10 K/min) according to Equation (2.8) (see Chap. 2.2) [50]. The obtained value of 60 ± 2.9 kJ/mol (compare the temperature modified "Arrhenius plot" in Fig. A.1(b) in Appendix A.1) is characteristic for the reduction of bivalent CuO to its metallic form [75, 76]. Thus, a CuO-like identity is preserved in CZA-calc although the Cu^{2+} species behave as isolated cations in the Zn-Al matrix.

Furthermore, whereas the conventionally prepared precursor has a nearly symmetric profile, CZA-calc is characterized by a bimodal TPR profile. As already known, the reduction of Cu based catalysts, in general, is a multistep process and, hence, not characterized by a single TPR peak [74, 77]. However, there are two possible explanations for the pronounced shoulder in the TPR profile of CZA-calc: Either the reduction is diffusion limited or runs through a quite stable intermediate.

To deconvolute the phenomenon of the pronounced shoulder on the low temperature side, a TPR profile with a high heating rate of 15 K/min was recorded additional to the multiple heating rate experiments, which were used for the apparent activation
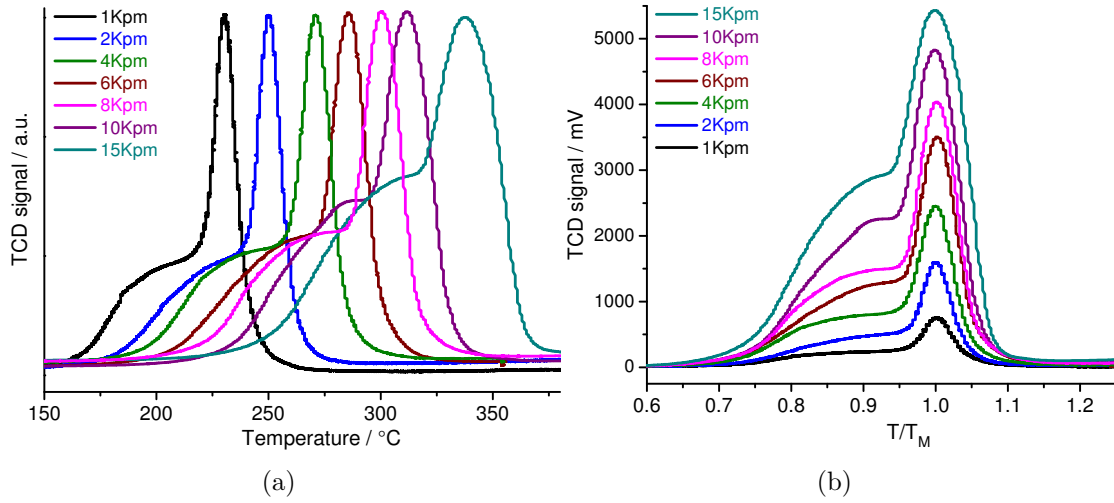
Figure 4.14: Heating rate dependent TPR profiles of CZA-calc: (a) temperature profiles with normalized intensities, (b) profiles normalized on T_{max}.

energy determination. As described by Monti and Baiker [47] higher heating rates result in higher reduction temperatures (see Fig. 4.14). Furthermore, it is expected for diffusion limited reduction that the shoulder at lower temperatures would get significant smaller with decreasing heating rates, whereas at high heating rates the gas phase diffusion dominates the reaction rate. A two-step reduction, on the other hand, would result in two separated peaks for high heating rates like observed by Bosch et al. [78] for the multiple-step reduction of V_2O_5 to V_2O_3. The experimental results in Figure 4.14 (time profile in Appendix A.1 Fig. A.4) show that an increasing heating rate has a significant but small influence on the shape of the reduction profile at the lower temperature side, but no separation of the peaks is observed. This indicates that the reduction is, indeed, diffusion limited but this is obviously not the only effect responsible for the bimodal profile.

A detailed analysis of the multiple heating rate TPR experiments was done using the NETZSCH Thermokinetics software package. The evolution of hydrogen consumption was found to be characteristic for a two-step consecutive reaction (A $\rightarrow$ B $\rightarrow$ C) as exemplary shown in the qualitative peak deconvolution in Figure 4.15(a). This knowledge was used as a basis for the determination of characteristic kinetic parameters, where 16 commonly used models have been fitted to the experimental data [79]. The best fitted model for both steps was the Prout-Tompkins
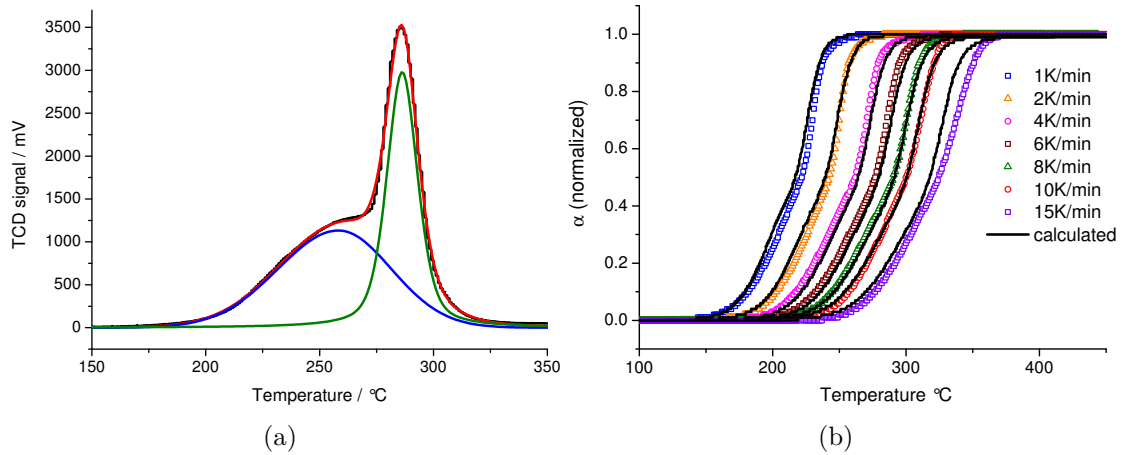
Figure 4.15: Evaluation of TPR data: (a) qualitative deconvolution of TPR profile (6 K/min) of CZA-calc showing a two-step reduction, (b) reduction progress (α) in dependence of temperature: comparison of calculated and measured values for different heating rates.

equation with the corresponding function $f(\alpha) = (1 - \alpha)^n \cdot \alpha^a$. Here, α is the reduction progress, n the reaction order regarding the educt, and a the one of the product. The latter is indicating an autocatalytic reaction, which is thought to be caused by adsorption of molecular hydrogen on the metal which gives rise to chemisorbed hydrogen atoms, and further facilitate the reduction of adjacent oxide particles [80]. All estimated values, apparent activation energy (E_A), pre-exponential

Table 4.3: Kinetic parameters determined from a refinement of TPR profiles of CZA-calc measured with different heating rates; inaccuracy of activation energy results from least square method of the linear regression.

Stage No., i	E_A / $kJmol^{-1}$	lg(A) / s^{-1}	n	a
1	52.9 ± 2.0	3.0 ± 0.2	0.9 ± 0.2	0.6 ± 0.0
2	63.2 ± 3.8	4.1 ± 0.6	1.2 ± 0.4	1.2 ± 0.4

factor (lg(A)) and reaction orders (n, a), are listed in Table 4.3. The calculated α versus temperature plots in comparison to the experimental data are depicted in Figure 4.15(b). The sigmoidal shape of the curves is typical for the nucleation model whose rate is dominated by the formation of the first nuclei (see Chap. 2.2). This behavior is in agreement with investigations in literature, where the reduction of both bulk as well as supported CuO could be described with the nucleation model [46, 80].

Furthermore, the measured data are in good agreement with the calculated ones with the exception of the high heating rate experiment. Here, the reduction progress is slower than expected indicating again an important role of diffusion limitation which is strongly dominating at high heating rates.

Additional to TPR experiments, the evolution of the Cu phase on the surface was investigated by NEXAFS spectroscopy. By comparison of the measured spectra to spectra of reference compounds, CuO, Cu_2O and Cu^0, it can be seen (Fig. 4.16(a)) that the formation of Cu_2O starts at around 175 °C, indicated by the pronounced peak at 933 eV. This temperature corresponds to the starting reduction seen in the TPR profile (Fig. 4.16(b)). The small peaks at the Cu_2O edge jump position in the spectra measured at 75 °C and 100 °C is probably due to partial reduction in the vacuum or by the beam.
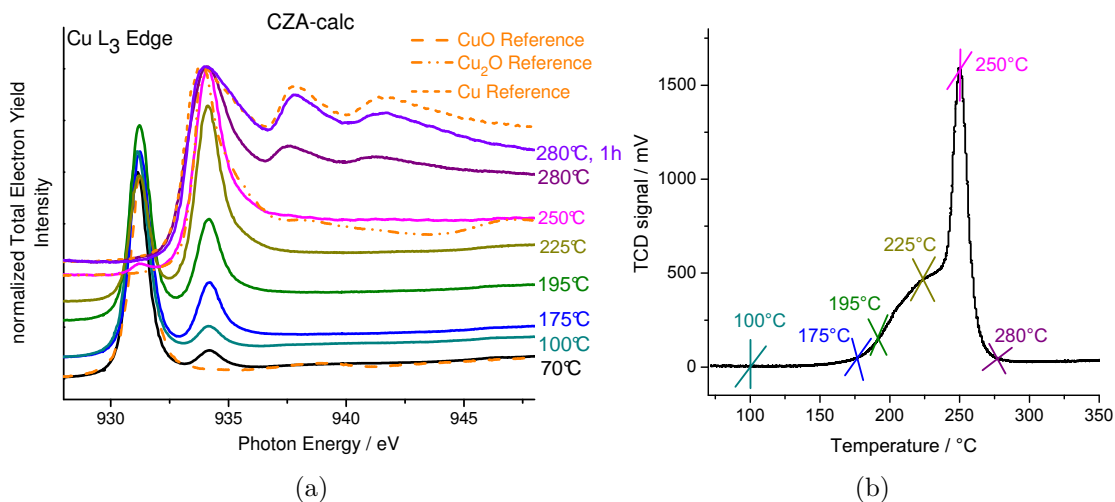
Figure 4.16: Investigation of reduction behavior of CZA-calc in hydrogen with 2 K/min: (a) NEXAFS spectra of evolution of Cu phase, (b) corresponding TPR profile.

For quantification the measured data were evaluated by linear combination of the three reference spectra, and the resulting data are presented in Figure 4.17(a). The CuO content is just slightly decreasing up to 195 °C as expected for a nucleation-growth mechanism, where the formation of first reduced nuclei occurs on top of the oxide particle (see Chap. 2.2). Above 200 °C the CuO phase is reduced to Cu_2O without significant formation of Cu. This observation is in agreement with earlier observations [81], where XANES (x-ray absorption near edge structure) investigations

during the reduction of CuO to Cu metal have shown that metastable Cu_2O species were formed as intermediate. After reduction at $260\,^\circ C$ no CuO is observed anymore, coinciding with the maximum of Cu_2O formation. Reduction at $280\,^\circ C$ for $1\,h$ leads to nearly complete reduction of CuO as just minor amounts of Cu_2O were present.

After all, the analysis of the multiple heating rate experiment proved a two-step reduction mechanism. Furthermore, we have shown by NEXAFS spectroscopy that Cu_2O is formed as metastable intermediate at least at the surface. With the assumption of a similar behavior for the bulk, the kinetic parameters listed in Table 4.3 can be reinterpreted as "step1" belonging to $CuO \rightarrow Cu_2O$ and "step2" describing $Cu_2O \rightarrow Cu$. Accordingly, the reduction of CuO is easier than the reduction of Cu_2O as the latter has the higher activation energy indicating an unexpected "stability" of Cu_2O.
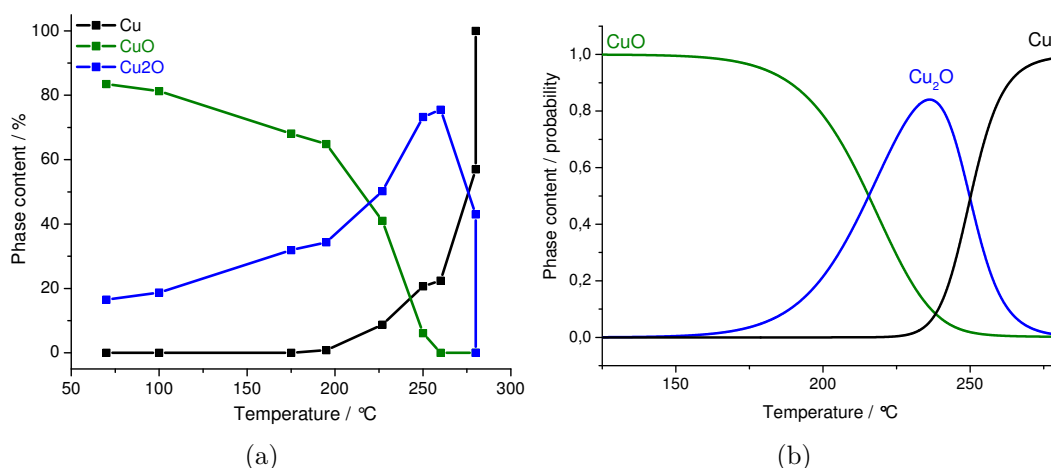
Figure 4.17: Evaluation of the reduction of CZA-calc in hydrogen using $2\,K/min$ heating rate: (a) results of quantification of NEXAFS data – done by linear combination of reference spectra, (b) prediction of phase evolution from TPR data.

From the calculated kinetic models derived from TPR measurements (Fig. 4.15, Tab. 4.3) it is possible to predict the phase evolution during reduction as exemplary shown for $2\,K/min$ in Figure 4.17(b). The measured phase evolution near the surface (NEXAFS) is in qualitative agreement with the prediction made from bulk behavior (TPR). Both showing the parallel existence of CuO, Cu_2O and Cu during reduction as well as the delayed reduction of Cu_2O to metal Cu. Other differences can be attributed to the difference in partial pressure of hydrogen (TPR: $5\,\%$ H_2/Ar at

1.5 bar, NEXAFS: 0.25 mbar H_2). This similarity shows that Cu(I) is indeed formed as intermediate during the reduction of the ex-LDH catalyst.

NEXAFS spectra measured during the reduction of the conventionally prepared reference catalyst (see Fig. 4.18) contain as well an indication for intermediary Cu_2O formation, but the temperature range of its presence without significant formation of Cu^0 ($\Delta T < 50 \,°C$) is much smaller than for CZA-calc ($\Delta T > 80 \,°C$). Besides, this observations indicates that Cu(I) is a kinetic stabilized intermediate which is favored in the ex-LDH system, as already seen in the difference of both TPR profiles. Nevertheless, the high "stability" of Cu_2O, leading to the pronounced shoulder of the
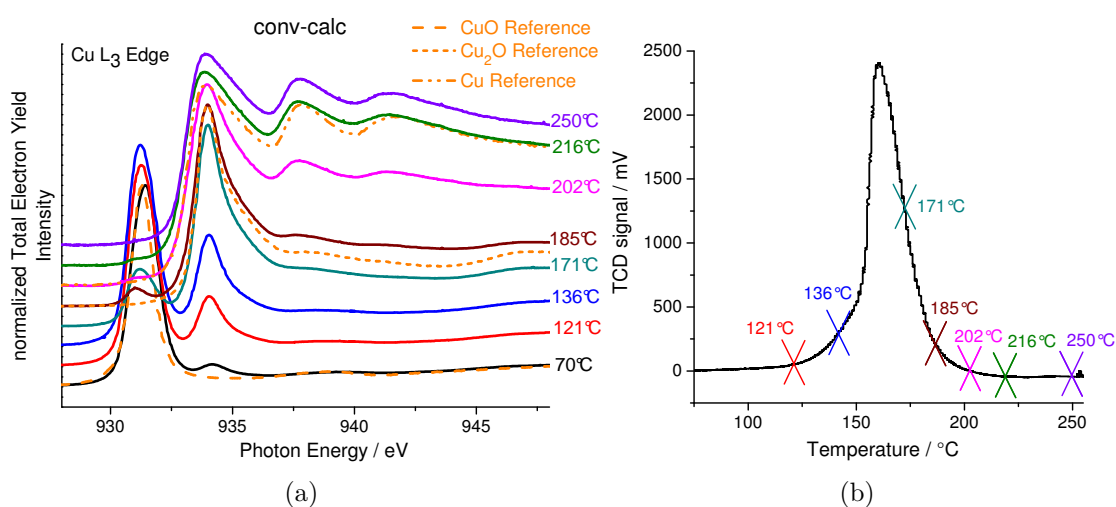
Figure 4.18: Investigation of reduction behavior of conventionally prepared reference catalyst in hydrogen with 2 K/min: (a) NEXAFS spectra of evolution of Cu phase, (b) corresponding TPR profile.

TPR profile of CZA-calc, indicates that the reduction rate of ex-LDH catalysts is not only dominated by the formation of Cu_2O or Cu nuclei as expected for nucleation mechanism [46].

4.3.2 TG-DSC experiment

Additional to the TPR experiment, thermogravimetric analysis of the reduction combined with DSC and MS measurement were performed for three different heating rates, exemplary shown for 5 K/min in Figure 4.19 (compare TG-DSC curves for 2 and 10 K/min in Fig. A.5 in Appendix A.1). This TG-DSC curve show that CZA-calc
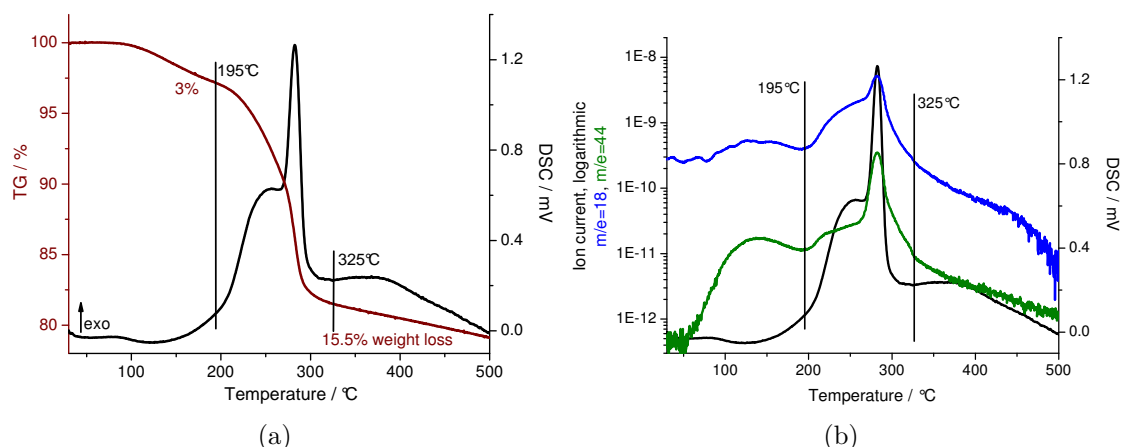
Figure 4.19: DSC curves of reduction in hydrogen of CZA-calc with $5\,\mathrm{K/min}$:
(a) TG-DSC, (b) DSC-MS with MS traces of H_2O (blue) and CO_2 (green).

loses $3\,\%$ weight until $195\,^\circ C$, coinciding with a small decrease in the DSC signal (endothermic effect), explainable by desorption of adsorbed water (compare MS trace in Fig. 4.19(b)). The main weight loss during reduction ($15.3\,\%$) occurs between $195 - 315\,^\circ C$ resulting in the exothermic DSC signal in a similar shape like observed in TPR.

For all three heating rates, during this catalyst activation CO_2 appeared in the corresponding MS spectra (see Fig. 4.19(b)(b) for $5\,\mathrm{K/min}$), where the maximum always coincides with the corresponding maxima of water and DSC signal. This CO_2 evolution is explainable by the weakened interaction of the $HT\text{-}CO_3^{2-}$ with the oxide present in CZA-calc (compare TG-MS in Fig. 4.8) due to the reduction of Cu^{2+}. As the hydrogen consumption is very close to that required for the stoichiometric reduction of Cu^{2+} to Cu, we suggest that these carbonate anions only undergo a decomposition process under reduction conditions without influencing the thermal conductivity measured by TPR. Nevertheless, the resulting catalyst still contains $\approx 4.8\,\mathrm{wt}\%$ of carbonate independent of the applied heating rate (the theoretical weight loss during reduction amounts to $11.5\,\%$ and $8\,\mathrm{wt}\%$ carbonate were present in CZA-calc). In contrast to pure CuO, the decomposition of the $HT\text{-}CO_3^{2-}$ during the reduction of CZA-calc occurs in parallel to the segregation of the Cu phase. Thus, we assume that the combination of both steps due to the strong interaction of Cu and the Zn-Al matrix is hindering the reduction and increasing the stability of the Cu(I) intermediate.

4.3.3 Conclusion

In summary, the reduction of the Cu species in CZA-calc follows a two-step mechanism as expected for CuO and as observed in the conventionally prepared reference catalyst including the formation of a kinetic stabilized Cu(I) intermediate. Combining the information gained from TPR, NEXAFS and TG-DSC the special shape of the reduction profile is explicable by the homogeneous distribution of Cu in combination with the strong interaction to the Zn-Al matrix implemented by the hydrotalcite phase of the precursor. Due to the homogeneous distribution and the strong interface contact the reduction is delayed as the migration of Cu^{2+} needs to be activated first. Furthermore, the strong interaction (already seen by the high decomposition temperature of the HT-CO_3^{2-} in CZA-calc) leads to hindered diffusion within the solid state which is necessary to form metallic Cu. Thus, the "stability" of Cu_2O, which leads to the pronounced shoulder of the TPR signal, is mainly caused by mass transfer limitations within the solid state. In conclusion, the nanostructuring by phase separation and segregation takes place during reduction and not during calcination as observed for the conventionally prepared reference catalyst (Fig. A.8).

Besides, the calculated kinetic model (Tab. 4.3) allows for the prediction of the phase evolution as shown in Figure 4.17(b). The complete reduction (for 6 K/min) is also achieved after reduction at 300 °C, meaning $10 - 15$ °C above T_{max}, and an isotherm period of 30 min as shown in Figure 4.20. Accordingly, these conditions were used to prepare the reduced catalyst CZA-red, e. g. for TEM investigations and N_2O-RFC.
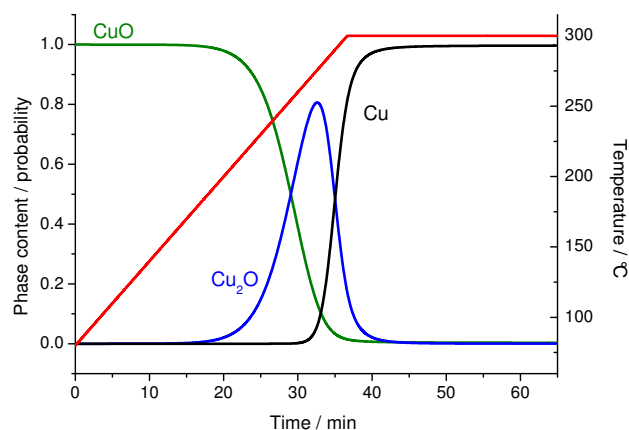
Figure 4.20: Calculated phase evolution during reduction in hydrogen with a heating rate of 6 K/min to 300 °C and an isotherm period of 30 min.

4.4 Microstructural characterization of catalyst resulting after reduction

In the catalyst resulting from the Cu,Zn,Al LDH precursor only Cu (ICSD: 4-0836 [82]) is present as crystalline phase as shown by in-situ XRD after reduction, presented in Figure 4.21. This is also confirmed by TEM, which shows small Cu
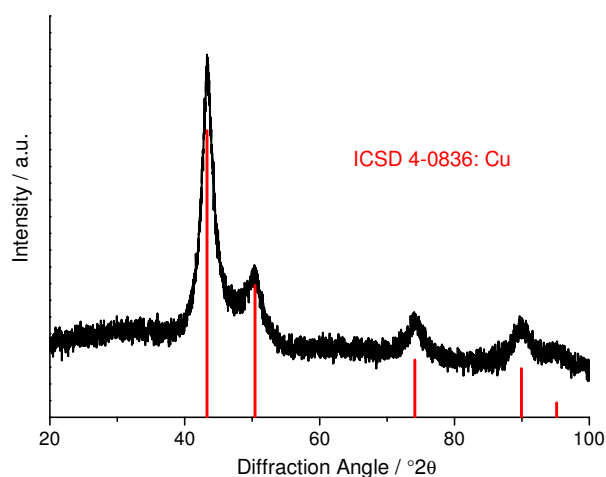
Figure 4.21: XRD pattern after reduction in in-situ XRD cell: 6 K/min to 300 °C for 30 min.

particles with an average diameter of 7 nm (compared to 10 nm for the conventionally prepared reference catalyst), Cu particle size distribution is presented in Fig. 4.22(b). Furthermore, the TEM image in Figure 4.22(a) illustrates that the Cu particles are highly embedded within a mostly amorphous, oxidic matrix, which was already observed for some regions in the samples of a previous study [29]. The presence of a continuous embedding oxide matrix can be seen as the major difference to the conventionally prepared $Cu/ZnO/Al_2O_3$ catalyst, whose microstructure is characterized by much more free-standing Cu particles with less interface area to the oxide particles (see Appendix A.2 Fig. A.9).

4.4.1 XPS and XAS measurement

To gain information about the surface composition of CZA-red, an analysis of the Cu species was done in relation to Zn by XPS data. By NEXAFS (Chap. 4.3.1)

(a)

(b)
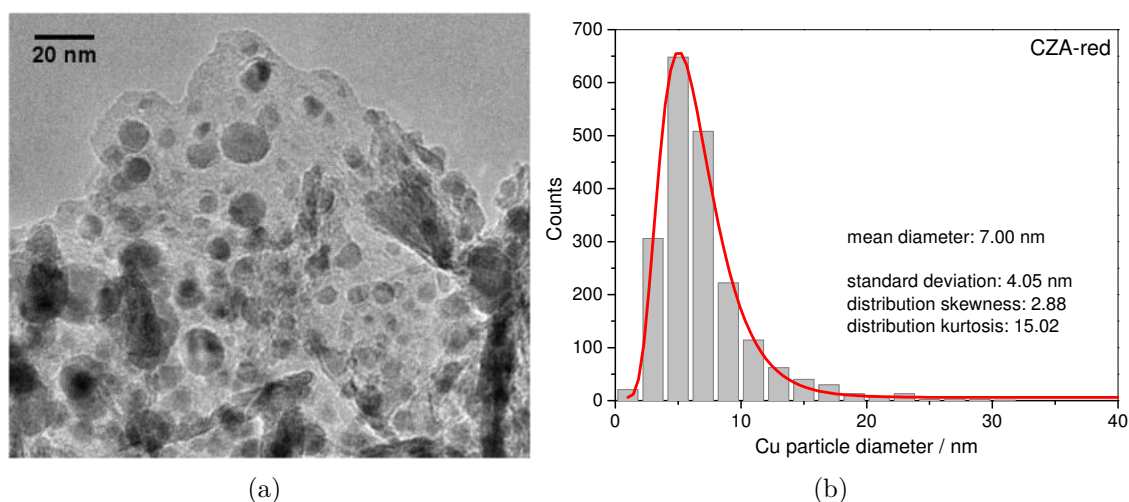
Figure 4.22: TEM investigation of CZA-red: (a) TEM image: highly embedded Cu^0-particles (dark spots) in oxidic matrix, (b) Cu particle size distribution (1995 particles measured).

just minor amounts of oxidic Cu were found after reduction for $1\,h$ at $280\,°C$ in the in-situ cell (at BESSY). Accordingly, oxidic Cu was found by XPS (Fig. 4.23) in the reduced CZA catalyst, labeled as CZA-red-XPS. According to literature [83–85] and the knowledge from NEXAFS data that CuO is disappeared at this temperature (Fig. 4.17(a)), the oxidic species is assigned to Cu_2O.
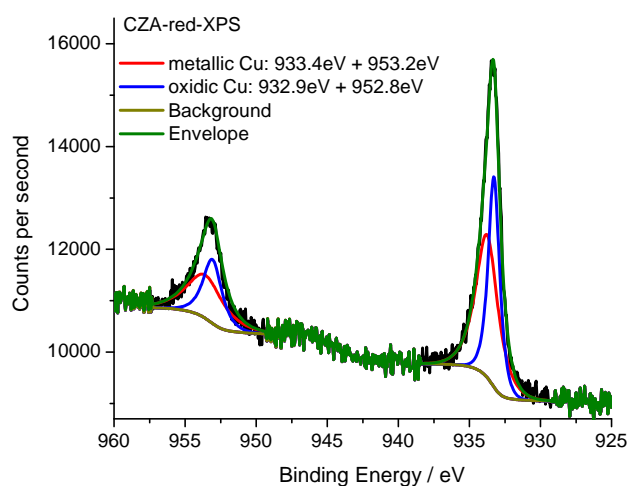
Figure 4.23: XPS of CZA catalyst measured in in-situ XPS cell at $280\,°C$ in $0.25\,mbar\ H_2$: peak deconvolution of Cu2p core level showing metallic and oxidic Cu species [83–85].

NEXAFS measurement of Zn L_3 edge, shown in Figure 4.24(a), proves again (like in calcined state, Fig. 4.12) the presence of $ZnAl_2O_4$ spinel. On the other hand, the peak deconvolution of Zn2p core level of CZA-red-XPS, illustrated in Figure 4.24(b), show that the majority (62%) of the Zn-oxide is $ZnAl_2O_4$ [86], whereas the second oxide species present is assigned to ZnO [87]. In the conventionally prepared reference catalyst both techniques – peak deconvolution of Zn2p core level (compare Fig. A.7(b) in Appendix A.2) and NEXAFS comparison – just indicate the presence of ZnO.
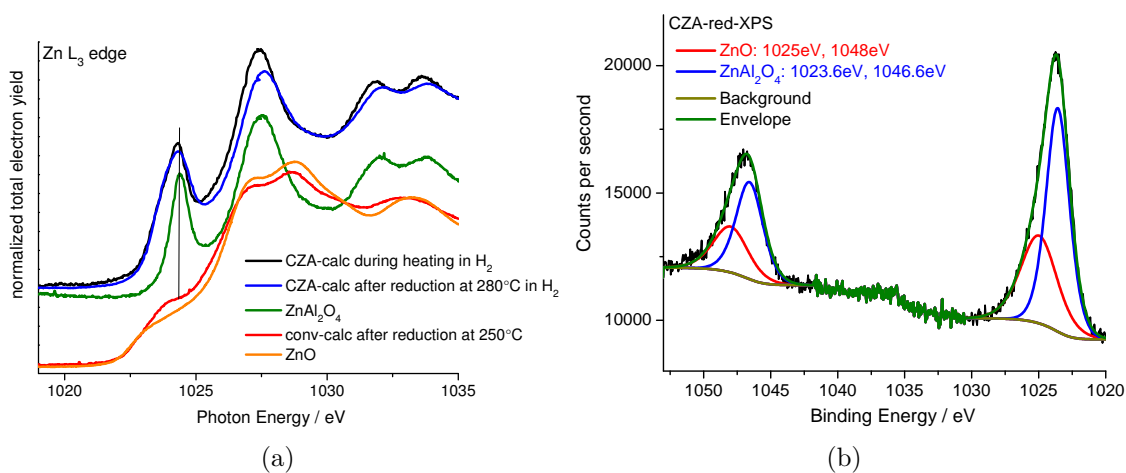
Figure 4.24: Zn environment of CZA catalyst measured in in-situ XPS cell at 280 °C in 0.25 mbar H_2: (a) NEXAFS of Zn L_3 edge compared to $ZnAl_2O_4$ reference compound and conventionally prepared reference catalyst, (b) XPS: peak deconvolution of Zn2p core level showing $ZnAl_2O_4$ and ZnO.

By detailed analysis of Cu2p and Zn2p data just a small Cu content was found on the surface of CZA-red-XPS – Cu : Zn ratio of 22% compared to 75% in the bulk (known from XRF data of the calcined catalyst, Tab. 4.1 pH8). This is in agreement with the conventionally prepared reference catalyst where a decrease of Cu on the surface was observed during reduction (starting from 63% in the calcined state and ending with 29%; see Tab. A.1 and Fig. A.7 in Appendix A.2). This behavior was attributed to the SMSI-induced (strong metal support interaction; see Chap. 1.1.1) coverage of the Cu surface with ZnO as the catalyst is reduced [56]. Unfortunately, it was not possible to measure the change of Cu : Zn ratio during the reduction of CZA-calc, as it was highly charging in the beam until the reduction was nearly completed. Considering the higher Cu : Zn ratio in the bulk of CZA-red-XPS (75 : 25) compared to the conventionally prepared reference catalyst (70 : 30) its Cu content

on the surface is significant lower, explicable by the high embedment of Cu particles observed by TEM (Fig. 4.22(a)).

4.4.2 Cu surface area and activity in methanol synthesis

The Cu surface area of the ex-LDH catalyst was measured after isothermal reduction (labeled as mild) as well as after linear reduction with constant heating rate (labeled as hard) and compared to the conventionally prepared reference catalyst (conv-red). For the isothermal reduction, based on industrial applied catalyst activation, the catalyst was heated in hydrogen to $200\,°C$ with $1\,K/min$ and held for $13\,h$, followed by a heating to $250\,°C$ and holding for $30\,min$. The linear reduction implies a heating in H_2 to $300\,°C$ with $6\,K/min$ and holding for $30\,min$. The measured data in Table 4.4 indicate a thermal stability of the Cu surface area of the CZA catalyst, whereas the conventionally prepared reference catalyst loses $11\,\%$ of Cu surface area due to hard reduction conditions. According to this result, all following Cu surface areas presented throughout this thesis are obtained by applying the hard conditions.

Table 4.4: CZA-red compared to conventionally prepared reference catalyst: Cu surface area using mild or hard reduction conditions, relative Cu-SA = ratio of Cu-SA from hard and mild conditions.

	Cu-SA / m^2g^{-1}		
	mild	hard	relative Cu-SA [%]
CZA-red	7.2 ± 0.6	7.4 ± 0.7	103
conv-red	29.8 ± 0.7	26.3 ± 0.6	88

As described in Chapter 2.5.2, from TEM particle size and known Cu content it is possible to calculate a theoretical Cu surface area (Eq. (2.10)) as well as an interface ratio (Eq. (2.13)). The high embedment of Cu particles in CZA-red results in a high interface ratio of $85\,\%$ and, accordingly, just $15\,\%$ of the Cu surface area are accessible to the reaction gas.

Both catalysts were tested for their catalytic activity in methanol synthesis (see Tab. 4.5). Due to the high embedment, the absolute activity of the ex-LDH catalyst is much lower in comparison to the conventionally prepared one. But the so called intrinsic activity – catalytic activity related to the Cu surface area– is even better. This finding shows, that it is possible to tune on the effectiveness of the exposed Cu

surface area by improving the interface contact during the synthesis of the catalyst. Above all, this indicates that not only small Cu particles are necessary but the surrounding of these particles is essential for the resulting intrinsic activity.

Table 4.5: CZA-red compared to conventionally prepared reference catalyst: normalized activity in methanol synthesis at 250 °C: WTY = weight time yield of methanol, Act_{int} = intrinsic activity (WTY per Cu surface area– mild conditions taken).

	norm. WTY / %	norm. Act_{int}
CZA-red	36.4	5.0
conv-red	100	3.4

4.4.3 "Stability" in air

Industrial applied catalysts are known to be air sensitive after reduction, even spontaneous burning was observed. To get a better idea of the ex-LDH catalyst stability, CZA-calc was reduced and handled in air – labeled as CZA-red-air. For comparison the conventionally prepared reference catalyst was also investigated by XRD after reduction and contact to air (see Fig. 4.25(b)). The XRD pattern (see Fig. 4.25(a)) of CZA-red-air contains reflections of Cu_2O (ICSD: 78-2076 [88]) additional to the ones of Cu metal (ICSD: 4-0836 [82]), indicating a partial oxidation by contact to air. The Cu reflections are characterized by a smaller fhwm compared to the sample reduced in in-situ XRD. The conventionally prepared reference catalyst after contact to air (Fig. 4.25(b)), on the other hand, is mainly oxidized to CuO, where Cu metal is still present but just in small amount. The partial oxidation of CZA-red-air is also confirmed by TEM depicted in Figure 4.26. It reveals that smaller particles are completely oxidized to Cu_2O without an indication of metal lattice, whereas bigger particles consist of metal and partially oxide islands or layers, comparable to a core-shell situation. Accordingly, the oxidation of the smaller Cu particles explains the smaller fhwm of Cu metal observed in the XRD pattern (Fig. 4.25(a)) as just larger particles remain reduced.

This partial oxidation has no visible influence on the embedment as well as the Cu particle size (7.22 nm, PSD in Appendix A.1 Fig. A.6) indicating that the oxidation upon air contact does not affect the microstructure of the catalyst.

Due to this quasi air stability, it was possible to record SEM images as well as an adsorption isotherm without special sample treatment to avoid air contact. By SEM (Fig. 4.27) it is nicely illustrated that the reduced state is still dominated by the platelet-like morphology of the precursor system, but a few roundish particles (up to 20 nm) are visible on top of the platelets. Furthermore, the adsorption properties are almost unchanged for the reduced sample compared to the calcined one, meaning a just slightly decreased surface area (BET surface area 81 m^2/g for CZA-calc and
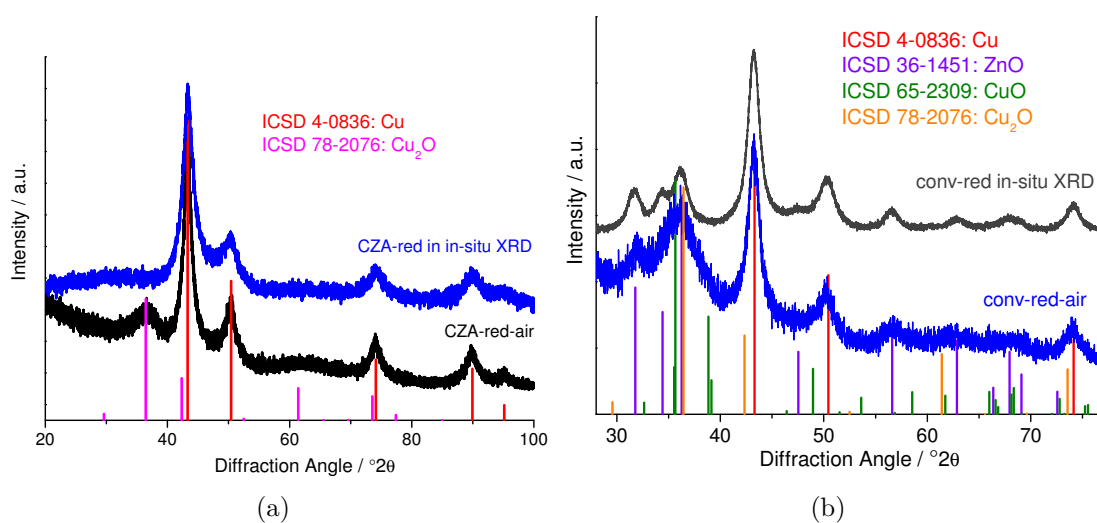
Figure 4.25: XRD pattern of (a) CZA-red and (b) conv-red after contact to air in comparison to pattern obtained in in-situ XRD.
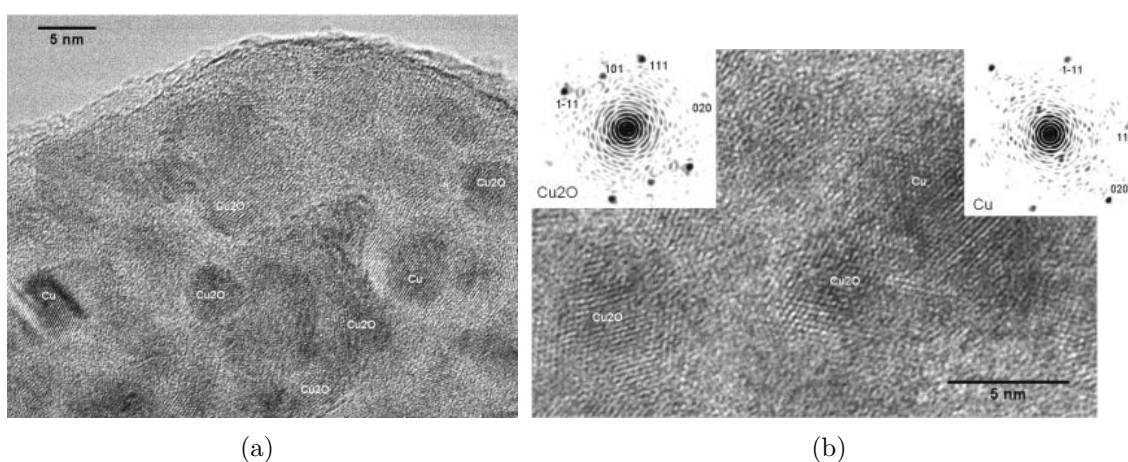
Figure 4.26: TEM images of CZA-red after contact to air.

(a)   (b)
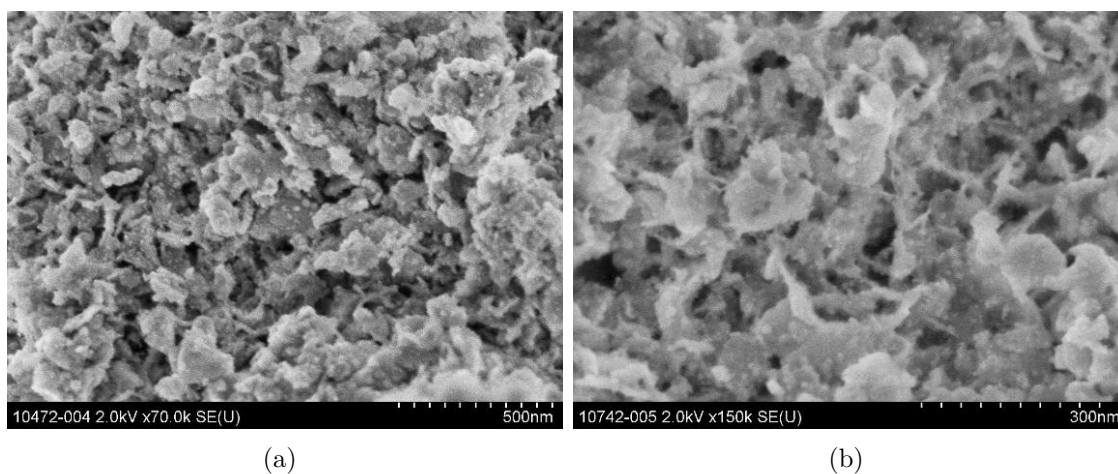
Figure 4.27: SEM images of CZA-red-air: platelet-like morphology with some roundish particles on top.

$78 \, \mathrm{m^2/g}$ for CZA-red-air) as well as still mesoporosity (Fig. 4.28(a), type IV isotherm, H1 hysteresis).

(a)   (b)
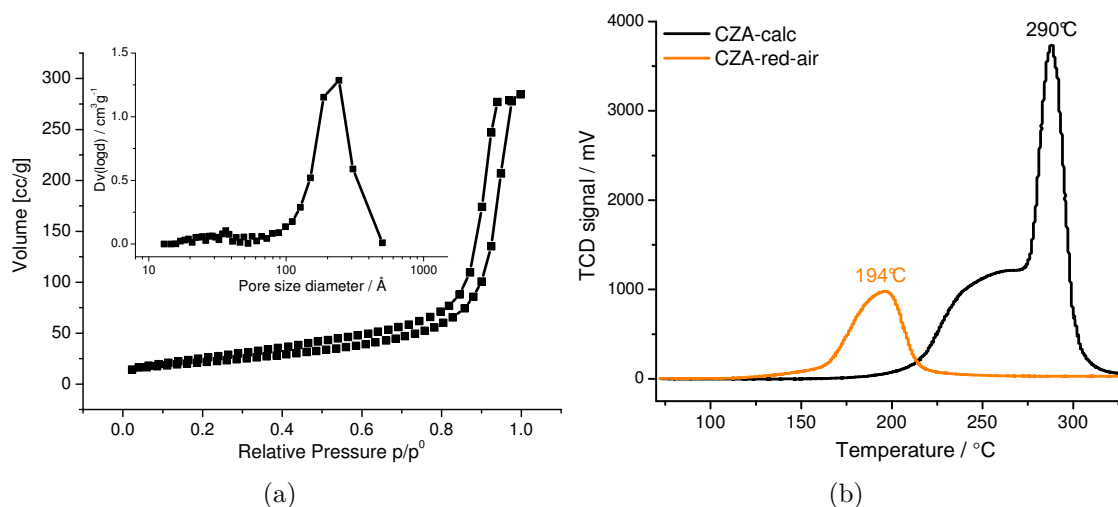
Figure 4.28: Characterization of CZA-red-air: (a) N_2 adsorption-desorption isotherm measured at $-196\,^{\circ}\mathrm{C}$ inserted with BJH "pore" size distribution, (b) TPR profile.

Interestingly, the reduction behavior of this partial oxidized catalyst, investigated by TPR (Fig. 4.28(b)), is changed significantly: The reduction temperature is shifted by 96 °C to lower temperature and the profile itself is broader without the pronounced

shoulder on the low temperature side resulting from Cu_2O as intermediate as well as diffusion limitation as discussed before (Chap. 4.3). The Cu surface area, on the other hand, is nearly unchanged giving a value of $6.5 \, m^2/g$ – proving that the partial oxidation has no influence on the degree of embedment (still 85% interface ratio) as it was already assumed from TEM images. Additionally, the TPR of CZA-red-air makes a quantification possible: 75% of the present Cu were reoxidized by contact to air under the assumption that Cu_2O was formed and fully reduced. Consequently, the XRD pattern in Figure 4.25(a) is dominated by 25% of the larger particles, which are still reduced. After all, this quasi air-stability opens the possibility to prepare a catalyst which can be activated before it is inserted into the reactor system of methanol synthesis.

4.4.4 TPR-TPO measurements - cyclization experiment

For further investigation of the catalyst stability and the interaction of Cu with the oxidic matrix TPR-TPO cycles were recorded. The TPO profiles (see Fig. 4.29(a)) show significant changes for TPO2 (reoxidation after TPR-TPO-TPR) compared to TPO1 (reoxidation of CZA-red without contact to air), whereas the profiles of TPO2 and TPO3 are nearly identical. The profile of TPO1 is characterized by two peaks
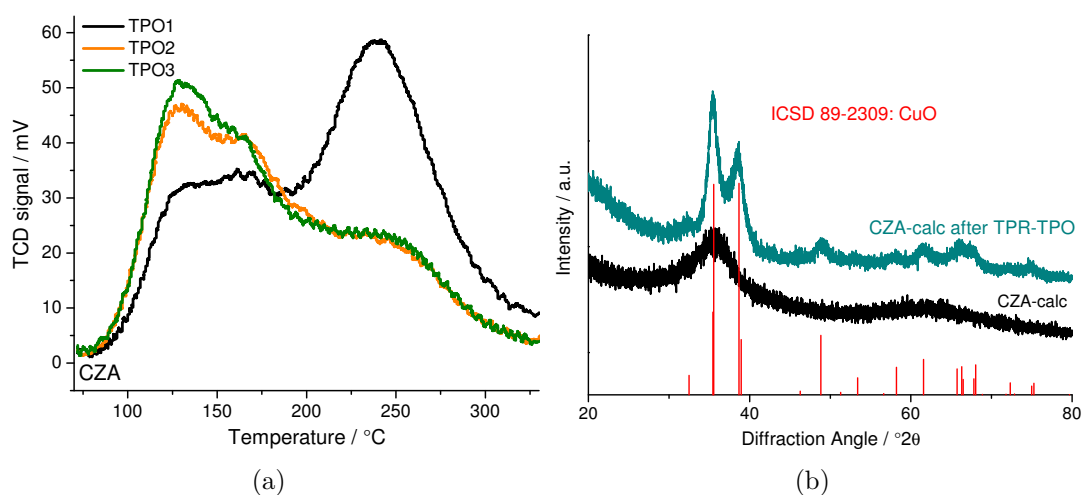
Figure 4.29: (a) TPO profiles of TPR-TPO cyclization experiment; (b) XRD pattern of CZA-calc compared to CZA-red after reoxidation: formation of crystalline CuO.

probably caused by Cu species exhibiting a different degree of interaction with the

oxidic matrix. In TPO2 and TPO3 the low temperature peak is more pronounced, whereas the high temperature signal is less intense. After the first reoxidation crystalline CuO (ICSD 65-2309 [71]) was observed by XRD (see Fig. 4.29(b)). As after calcination CuO was nearly amorphous this observation proves defined microstructural changes during the reduction-reoxidation process.

(a)   (b)
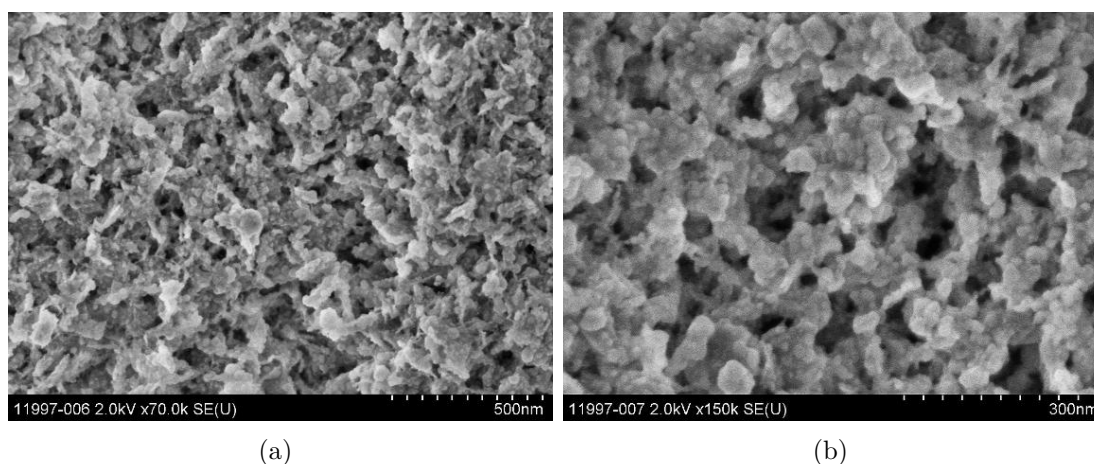
Figure 4.30: SEM images of CZA-red after reoxidation: platelet-like morphology with some roundish particles on top.

It is well known that during oxidation of Cu first an oxide layer is formed [89] on the metal particle, where a further oxidation is not occurring by oxide immigration but by metal emigration. This mobility of metal atoms and crystallites facilitates the migration of the small Cu particles in CZA-red under oxidizing conditions at high temperatures (high temperature peak in TPO1 signal). By this sintering effect the embedment is partially destroyed during the reoxidation process leading to crystalline copper oxide particles.

On the other hand, the obtained TPR profiles (Fig. 4.31(a)), show similar changes of the reduction behavior for TPR1 to TPR2 (profile of sample after first reoxidation) like observed before for CZA-red-air. The reduction temperature is $85\,°C$ lower than in TPR1 (profile of CZA-calc) and also the shape of the profile is again significantly different indicating a changed reduction mechanism. A comparison of these results with TPR-TPO experiments of the conventionally prepared reference catalyst (see Fig. 4.31(b)) exhibits the specialty of the ex-LDH catalyst system. For the conventionally prepared catalyst the temperature is shifted just slightly from
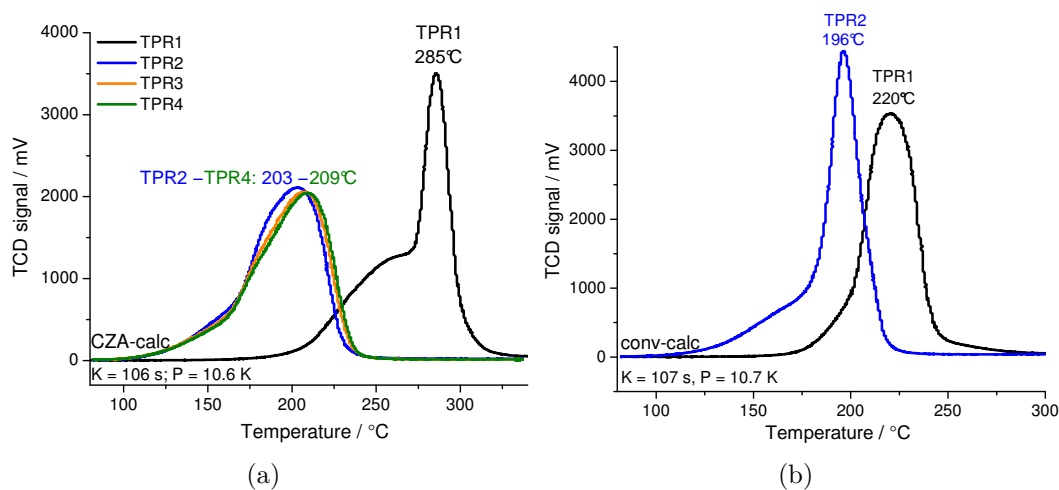
Figure 4.31: TPR profiles obtained by TPR-TPO cyclization experiment: (a) ex-LDH catalyst, (b) conventionally prepared reference catalyst.

TPR1 to TPR2 whereas the shape of the profile is sharpened with a more pronounced shoulder on the low temperature side. The reduction degree of the conventionally prepared catalyst is increasing for the second reduction procedure (see Tab. 4.6) indicating a more complete reduction after reoxidation. Surprisingly for the ex-LDH catalyst is the smaller hydrogen consumption in TPR2 (Tab. 4.6), indicating either an incomplete oxidation or an incomplete reduction afterwards. As TEM of this sample (see Fig. 4.32), labeled as CZA-TPROR, provides no information about crystalline CuO, which was observed after TPO1 (Fig. 4.29(b)), the incomplete oxidation is more likely. Additionally, TEM shows both the smaller embedded particles as well as larger particles with less embedment resulting in an increased averaged Cu particle size (see Tab. 4.6), in which all particles are still well-separated. The oxide matrix has changed slightly as also crystallites of $ZnAl_2O_4$ spinel as well as ZnO were observed (TEM-CZA-Spinell). Interestingly, the "stability" to air seems to be preserved during the reoxidation-reduction process as by XRD of CZA-TPROR-air (see Fig. 4.33(a)) just partial oxidation is observed after contact to air like before in CZA-red-air. The changed embedment did not influence the general adsorption behavior or porosity of the whole catalyst – still type IV isotherm and H1 hysteresis (Fig. 4.33(b)) and just slightly decreased ($66 \, \text{m}^2/\text{g}$) BET surface area. The morphology investigated by SEM (Fig. 4.34) is changed compared to CZA-red-air. The platelets are still present but appear less separated and on top of the platelets a lot of roundish

particles (up to 30 nm) are visible, probably due to the changed embedment of Cu. Surprisingly, the Cu surface area is nearly doubled during the reoxidation-reduction process (see Tab. 4.6). Thus, the larger but less embedded particles lead to a better accessibility of the Cu particles to reaction gas. Again a comparison to the conventionally prepared catalyst, which has a slightly decreased Cu surface area after
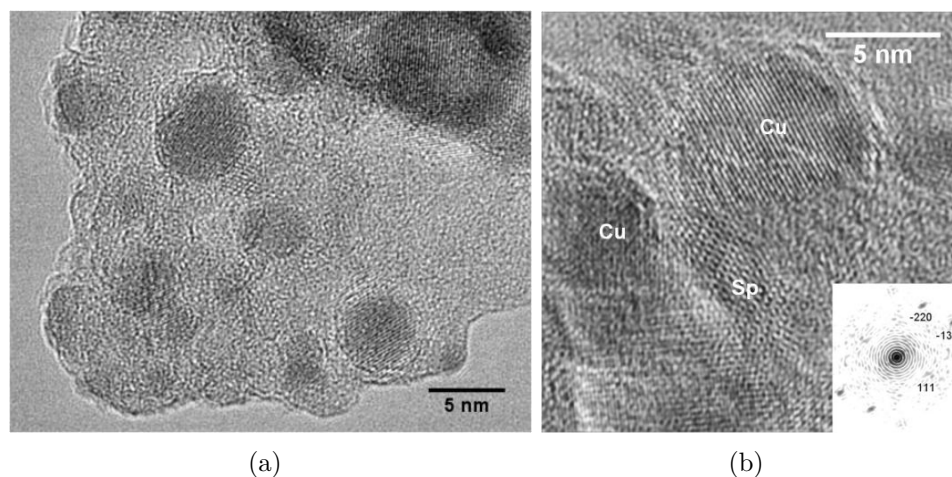
Figure 4.32: TEM images of CZA-red after additional TPO-TPR treatment: (a) small, embedded Cu particles and larger ones with less embedment, (b) oxide matrix show crystalline features: Sp = $ZnAl_2O_4$ spinell structure
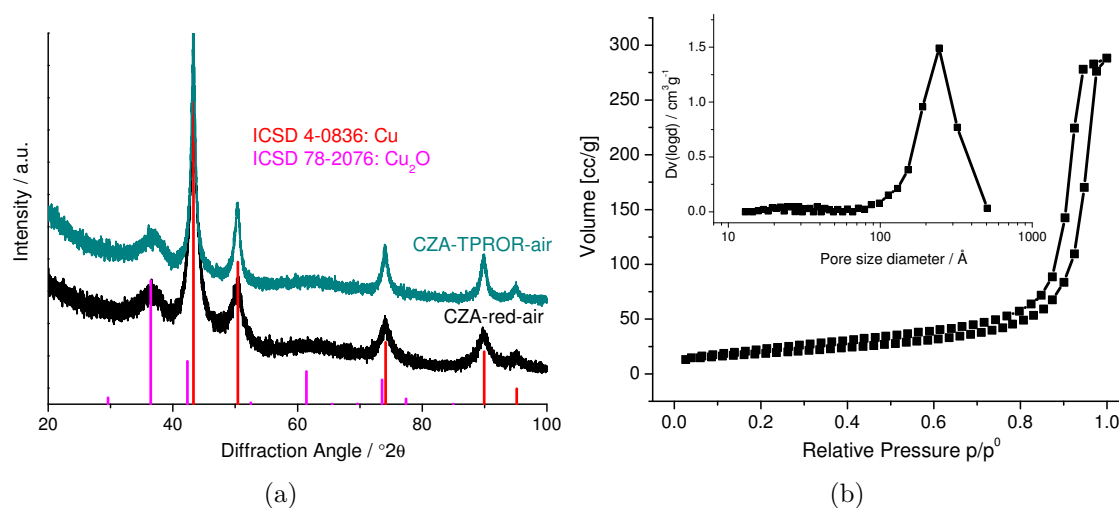
Figure 4.33: Characterization of CZA-TPROR after contact to air: (a) XRD pattern showing partial oxidation of Cu to Cu_2O, (b) N_2 adsorption-desorption isotherm.

<div align="center">(a)   (b)</div>
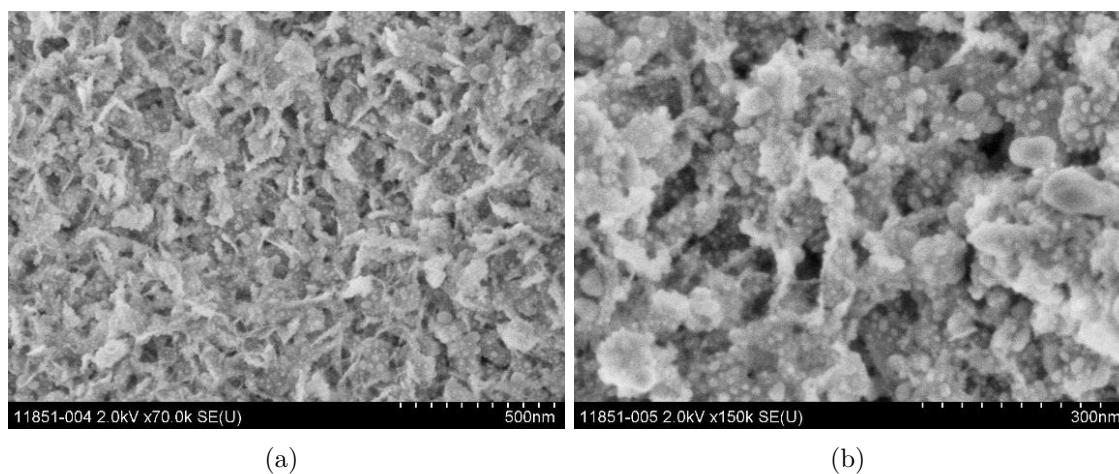
Figure 4.34: SEM images of CZA-TPROR after contact to air: (a) platelet-like morphology still present, (b) but roundish particles on top.

reoxidation-reduction (see Tab. 4.6), is indicating the special characteristic of the ex-LDH system.

As already observed for the TPO profiles, further reoxidation and reduction does not lead to significant changes (see Fig. 4.31(a) and Tab. 4.6). The reduction behavior, meaning the profile shape, the hydrogen consumption as well as the

Table 4.6: Comparison of the characteristics of TPR-TPO cyclization experiment of CZA and conventionally prepared catalyst obtained by TPR, N_2O-RFC and TEM particle size evaluation; interface ratio (IFR) is calculated from theoretic Cu surface area based on TEM particle size.

		TPR1	TPR2	TPR3	TPR4
	T_{max}	285	203	207	209
	H_2 consumption/CuO /%	98	85	84	84
CZA-calc	Cu-SA /m^{2}g^{-1}	7.4 ± 0.7	14 ± 0.7	15.5 ± 0.7	—
	Cu PS /nm	7.0	11.5	—	—
	IFR /%	85	55	—	—
	T_{max}	220	196	—	—
	H_2 consumption/CuO /%	94	99	—	—
conv-calc	Cu-SA /m^{2}g^{-1}	26.3 ± 0.6	23.2 ± 0.6	—	—
	Cu PS /nm	11	—	—	—
	IFR /%	25	—	—	—

65

reduction temperature, is nearly identical for TPR2, TPR3 and TPR4. The same is valid for the Cu surface area after TPR3 compared to TPR2 (Tab. 4.6).

The observations of the TPR-TPO cycles clearly show that the microstructural changes during TPR1 are irreversible, whereas a reoxidation afterwards leads to a reversible redox behavior.

4.5 Discussion and Conclusion

A phase pure Cu,Zn,Al LDH was prepared by co-precipitation at pH 8, resulting in the composition $(Cu_{0.5}Zn_{0.17})Al_{0.33}(OH)_2(CO_3)_{0.17} \cdot m\,H_2O$ and showing the typical platelet-like morphology and homogeneous distribution of all three metal cations. Upon decomposition in air a carbonate containing mixed oxide was formed, without any crystal lattice found by XRD or TEM. Furthermore, no phase separation and segregation was observed in the calcined state, and the platelet-like morphology of the precursor was maintained. The local environment around Cu^{2+} and Zn^{2+} in this homogeneous, amorphous oxide was similar to CuO and $ZnAl_2O_4$ as shown by NEXAFS. Thus, the mixed oxides can be described as well dispersed CuO within $ZnAl_2O_4$ still containing stabilizing $HT\text{-}CO_3^{2-}$ and the strong interaction of Cu^{2+} ions with the Zn-Al matrix via O^{2-} bridges, as similarly described in [74]. Accordingly, the calcination of CZA can be understood as preformation step, meaning formation of spinel structure and high dispersion of Cu phase, determined by the homogeneity of the elements implemented by the LDH precursor. The reduction of CZA-calc leads to the separation of reducible and irreducible species and the formation of small, highly embedded Cu particles. Consequently, this controlled phase separation and segregation represents the main nanostructuring step.

The reduction profile itself is characterized by a shift to higher temperatures (compared to a conventionally prepared reference catalyst) and a pronounced shoulder at the low temperature side. The temperature shift is explicable by the homogeneous distribution of Cu^{2+} as well as the strong interface contact which have to be overcome before reduction. Upon heating, the well dispersed Cu^{2+} cations separate from the Zn-Al-oxide matrix, form clusters and finally start to reduce. Furthermore, the deconvolution of the TPR profile proved a two-step reduction mechanism, where Cu_2O was found to be formed as a metastable intermediate by NEXAFS measurements.

Besides, the analysis of the multiple heating rate and TG-DSC experiment showed that the "stability" of this intermediate, which leads to the pronounced shoulder of the TPR signal, is mainly caused by mass transfer limitations within the solid state most probably due to the strong interaction of Cu^{2+} with the Zn-Al-matrix.

The resulting Cu based catalyst can be described as Cu dispersed in a $ZnAl_2O_4$ spinel-like matrix. Due to the high embedment of the small Cu particles (7 nm) it exhibits only a small absolute activity in methanol synthesis compared to the conventionally prepared reference catalyst but a high intrinsic one (relative to the Cu surface area).

To gain further information about the stability of the system and the interaction of Cu with the oxidic matrix TPR-TPO cyclization experiments were done. By that it was shown that the reduction of the well dispersed, amorphous CuO (TPR1) is an irreversible process. During reoxidation the embedment is partially destroyed by a sintering effect leading to crystalline copper oxide particles also observed by XRD. After all, the described strong interface interaction in CZA-calc was broken during reduction and not reinforced during reoxidation. Thus, the rereduction (TPR2) is not longer dominated by the migration of Cu^{2+} and accordingly the observed lower reduction temperature results.

Beside this, the intermediate Cu_2O is obviously less stable in the second reduction process as the pronounced shoulder of TPR1 is vanished. As the strong interaction of Cu with the Zn-Al matrix is already broken in CZA-TPRO the decreased "stability" of Cu_2O can be seen as proof for the assumption that the hindered diffusion within the solid state is causing the shoulder in the profile for TPR1. Accordingly, the complete reduction is faster and just the formation rate of the first Cu nuclei (temperature of beginning reduction) is dominating the reduction as typically described for nucleation mechanisms. Obviously the annihilation of embedment is limited as during further cyclization of oxidation and reduction no additional changes are observed. Thus, the state resulting after the first reduction and reoxidation cycle is reversible.

The rereduction of CZA-red-air, the catalyst handled in air, is in agreement with the findings and explanations of the TPR-TPO cycles. The interaction was already broken during reduction, accordingly the lower reduction temperature and the less pronounced shoulder are resulting.

This system is interesting for industrial application as, despite a low absolute activity, a high intrinsic activity in methanol synthesis was obtained for the catalyst

resulting after first reduction showing the high importance of the interface contact of Cu and its surrounding. Furthermore, this catalyst was shown to be oxidation stable under air contact.

As a general conclusion, we assume that the characteristics of the LDH precursor are largely reflected in the properties of the catalyst after the initial thermal treatment (so called chemical memory) and that the complete development of the catalyst´s final microstructure is finished only after repeated TPR-TPO treatment. Thus, in case of the ex-LDH catalyst, the redox cycling can be regarded as a part of the preparation rather than a deactivating stress test as in case of the conventionally prepared catalyst.

5 pH-controlled LDH synthesis by microemulsion technique

In this chapter the microemulsion (ME) synthesis of Cu,Zn,Al-LDH by pH-controlled co-precipitation within the ME-droplets using simultaneous dosing of metal salt solution and precipitation agent is presented. By applying the microemulsion technique to the present LDH precursor system (Chap. 4) it is supposed to influence the particle growth during the precipitation process. Furthermore, the present study aims for small Cu particles with improved accessibility to the reactant gas, but still show a good stability during reaction.

5.1 Introduction to the Microemulsion technique

The principle of microemulsions was shown to be a promising approach for the synthesis of nanoparticles in general [90] and of Cu based catalysts in particular [91]. A microemulsion is defined as a system of two non-miscible liquids, e. g. water and oil (typically an organic solvent), and a surfactant with a small droplet size (5 - 100 nm). These droplets can be used as "nano-reactors". This technique has been utilized to synthesize hydrotalcites [92–94] and was already applied using pH-adjusted microemulsions [93, 95].

A microemulsion is characterized by thermodynamic stability, transparency or weak opalescence and a low viscosity. The composition of the mixture is specified by the weight proportion of the oil in the mixture water and oil α (Eq. (5.1)) and by the weight fraction of the surfactant in the ternary mixture γ (Eq. (5.2)).

$$\alpha = \frac{m_{oil}}{m_{water} + m_{oil}} \qquad (5.1)$$

$$\gamma = \frac{m_{surfactant}}{m_{water} + m_{oil} + m_{surfactant}} \tag{5.2}$$

For the synthesis of nanoparticles W/O-microemulsions are generally used. They consist of small water droplets dispersed within an oil phase, as illustrated in Figure 5.1. In such a mixture new particles are formed by the fast exchange between the kinetic instable micelles [90]. For applying the microemulsion technique for the
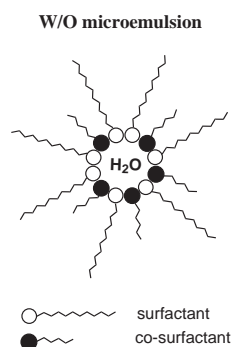
Figure 5.1: Schematic image of W/O-microemulsion.

precipitation of nanoparticles you can mix two microemulsions – one containing the metal salts and one containing the precipitating agent. The second possibility is to work with just one microemulsion containing the metal salts or the precipitating agent and add the second reactant directly to this one. Inspired by literature reports [90, 96, 97] the technical non-ionic surfactant Marlipal O13/40 (Fig. 5.2) was chosen for applying the microemulsion technique to the synthesis of Cu,Zn,Al-LDH.
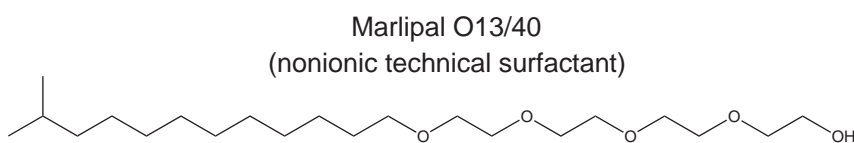
Figure 5.2: Structure of Marlipal O13/40.

5.2 Phase behaviour of the reactants

In order to determine suitable values for γ, α and T, the phase diagrams of all prepared microemulsions were explored by visual observation of the phase boundaries upon gradual change of the temperature. Herein, only was investigated the oil-rich

part of the phase prism (w/o-microemulsions). In this part of the Marlipal O13/40 system an optically clear and isotropic w/o-microemulsion region is present [96].

In Figure 5.3 the one-phase domain (hatched area) for two surfactant ratios of both reactants is shown as a function of temperature T and oil weight fraction α. As the higher surfactant ratio ($\gamma = 0.25$) shows the bigger overlap of the microemulsion regions of both solutions, this ratio was chosen for the synthesis. Furthermore, to work with a water content as high as possible and to make sure that the microemulsion is stable during reaction, the oil weight fraction should be approximately $\alpha = 0.9$ (8 % H_2O) and the reaction has to be carried out at 30 °C (see ellipses and arrows in Fig. 5.3).
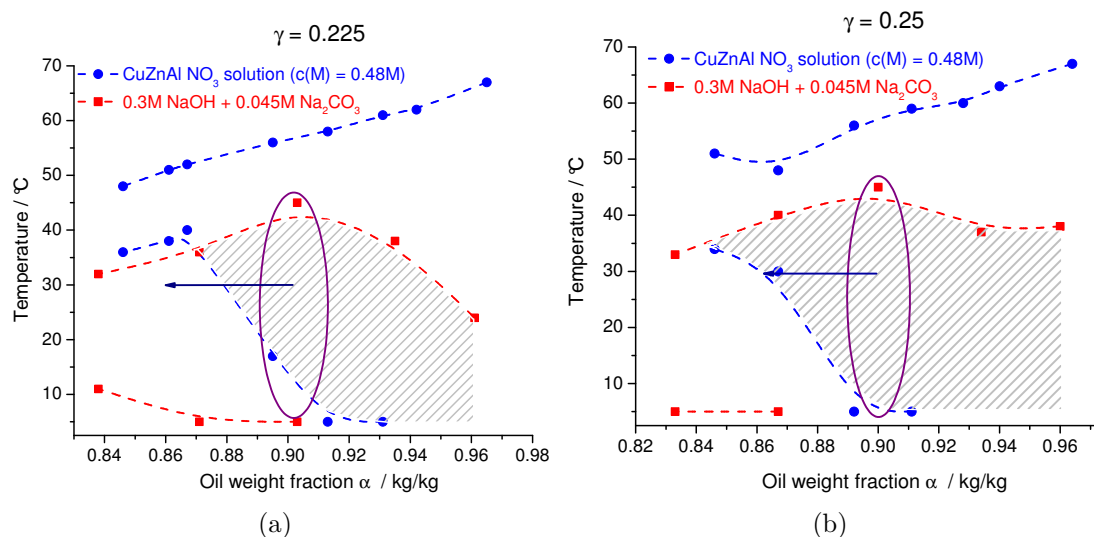
Figure 5.3: Oil-rich part of the phase prism of the quaternary system water/salt/ cyclohexane/Marlipal O13/40: (a) $\gamma = 0.225$, (b) $\gamma = 0.25$; c(M) = 0.43 M, c(Na_2CO_3) = 0.3 M, c(NaOH) = 0.045 M; the hatched area is suitable carrying out the precipitation within the microemulsion droplets.

The droplet size of different microemulsions was investigated by the dynamic light scattering (DLS). As illustrated in Figure 5.4 the applied microemulsion is a mono dispersed system with an average size of the water droplets of approximately 20 nm (see Tab. A.2 in Appendix A.3).
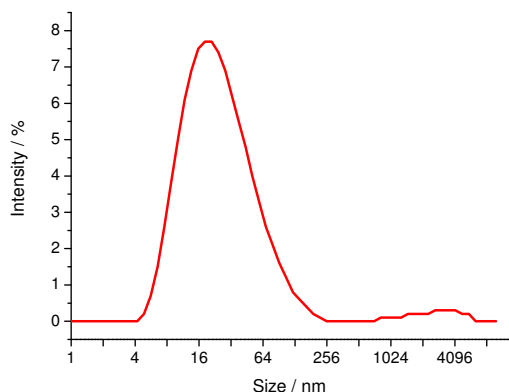
Figure 5.4: Size distribution of the water droplets of the template microemulsion measured by DLS.

5.3 Characterization of LDH precursor and calcined sample obtained from ME technique

The course of reaction of a Cu,Zn,Al hydrotalcite synthesis by using the microemulsion technique is shown in Figure 5.5. As the metal salt solution was added continuously
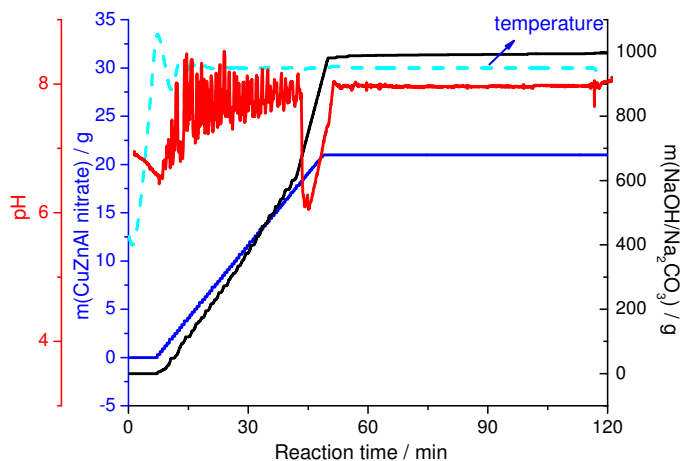
Figure 5.5: Protocol of microemulsion synthesis (Labmax).

the basic microemulsion was added simultaneously to control the pH. During reaction the composition of the ME changes due to a higher water content to approximately $\alpha = 0.86$ and $\gamma = 0.24$ which also leads to a smaller range of stability – on the limits regarding the metal salt solution. Accordingly, the observed pH drop (see Fig. 5.5)

at the end of the dosing could be explained by reaching the stability limit of the microemulsion of the product.

The product obtained by synthesis in microemulsion droplets, labeled as ME-LDH, is characterized in comparison to the conventional co-precipitated one, prepared under identical conditions, meaning the precipitation temperature, labeled as co-LDH. It has to be mentioned that the only difference to CZA (Chap. 4) is the precipitation temperature.

Table 5.1: Metal composition of investigated samples measured by ICP-MS (nominal composition: $Cu:Zn:Al = 50:17:33$) and d-values of (00l) reflections of XRD patterns.

Precursor	mol% Cu	mol% Zn	mol% Al	d(003)/Å	d(006)/Å
ME-LDH	50.29 ± 0.05	16.23 ± 0.01	33.48 ± 0.05	7.44 ± 0.007	3.72 ± 0.004
co-LDH	49.74 ± 0.16	16.14 ± 0.09	34.12 ± 0.07	7.48 ± 0.007	3.74 ± 0.004

The average composition of both precursors was determined by ICP-MS and was found to be close to the nominal values (Tab. 5.1). Like described for CZA, as example for the conventional co-precipitation, also the microemulsion-synthesis results in a crystalline material with hydrotalcite-like structure (see XRD pattern in Fig. 5.6) reported for a sample $Cu_3Zn_3Al_2(OH)_{16}CO_3 \cdot 4H_2O$ (ICSD 37-629) [26]. The reflec-
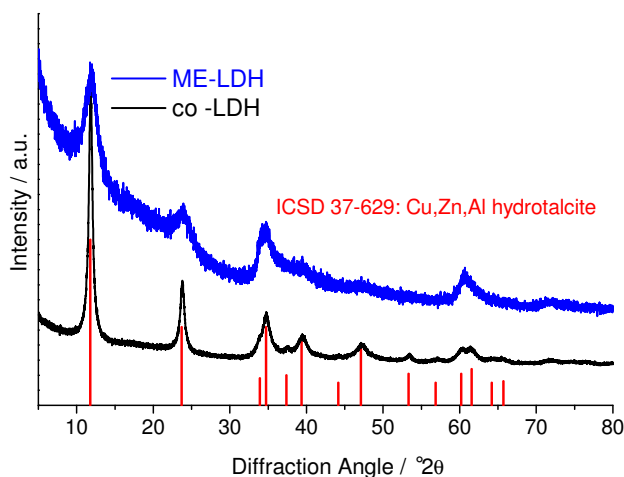
Figure 5.6: XRD patterns of reference precursor (co-LDH) and the product obtained by microemulsion synthesis (ME-LDH).

tions of the ME-LDH sample are clearly broadened either due to lower crystallinity or

smaller crystallites compared co-LDH. Furthermore, the (00l) reflections are slightly shifted to higher angles and accordingly lower d-values (see Tab. 5.1), indicating a smaller interlayer space (compare Chap. 2.1). In the SEM images (Fig. 5.7) it was
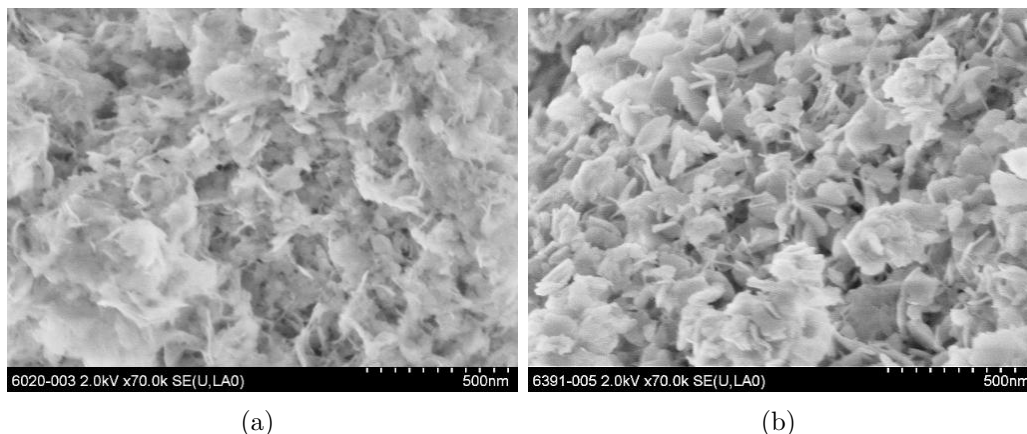
Figure 5.7: SEM images of the precursors: (a) ME-LDH and (b) co-LDH.

visible that both products show the typical platelet-like morphology of hydrotalcites. In agreement with the broader XRD reflections of ME-LDH its particles are smaller in comparison to co-LDH (see Tab. 5.2). Accordingly, ME-LDH has a significant higher BET surface area (Tab. 5.2).

Table 5.2: Lateral particle sizes (PS) of the platelets determined from SEM (>100 platelets), BET surface areas measured by N_2 physisorption.

microemulsion			co-precipitation		
label	PS / nm	S_{BET} /m^2g^{-1}	label	PS / nm	S_{BET} /m^2g^{-1}
ME-LDH	54	151	co-LDH	64	80
ME-calc	52	128	co-calc	59	83

The thermal behaviour of the ME precursor was investigated by TG-MS (see Fig. 5.8). Like described for CZA in Chapter 4.2.2, ME-LDH shows, in general, the same features for the decomposition of the hydrotalcite structure. This behaviour is another indication for the phase pure LDH structure in ME-LDH. The decomposition temperature of the HT-CO_3^{2-}, on the other hand, is significantly lowered for ME-LDH (515 °C) compared to co-LDH (for CZA: 615 °C, see Fig. 4.8). Additionally, the ME-LDH shows an exothermic event at 230 °C (Fig. 5.8) which correlates with the
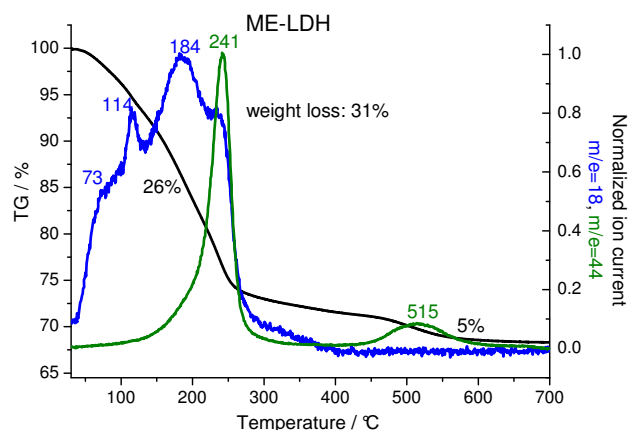
Figure 5.8: Weight loss and MS spectra during calcination of ME-LDH.

formation of CO_2 and H_2O and can be assigned to the combustion of adsorbed and/or intercalated organic residues (e. g. acetone from washing). For ME-LDH the MS signal of the interlamellar water loss at $114\,°C$ exhibits a significant lower intensity compared to the dehydroxylation step. As the weight loss is, furthermore, similar for both samples organic molecules are assumed to substitute some water molecules in the interlayer of ME-LDH compared to the amount in co-LDH.

By IR spectroscopy this is confirmed (see Fig. 5.9), as the water band of co-LDH at $1650\,cm^{-1}$ is replaced by a vibrational band at $1550\,cm^{-1}$ which is assigned to
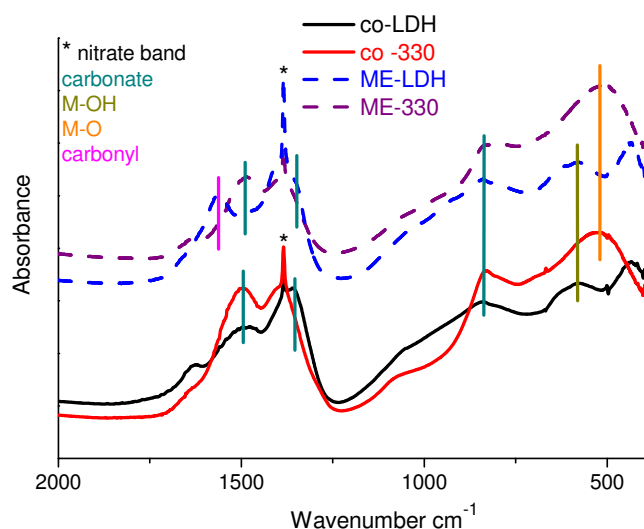
Figure 5.9: IR spectra of precursor and calcined samples.

coordinated carbonyl – probably acetone (used for washing before drying) which remained within the interlayer during the drying process . Besides, this is also the most likely explanation for the difference of the interlayer spaces observed by XRD. Furthermore, the other peaks of the spectra ($570\,\mathrm{cm^{-1}}$ – metal-OH deformation; $1360\,\mathrm{cm^{-1}}$, $840\,\mathrm{cm^{-1}}$ – interlayer CO_3^{2-} deformation [98]), all belonging to the LDH compound, show a similar signature for both precursors. All spectra contain a nitrate band at $1385\,\mathrm{cm^{-1}}$ which results from co-intercalated nitrate anions in the LDH interlayers. According to the TG-MS curve, all organic molecules are finally decomposed at $250\,^\circ\mathrm{C}$. As we have shown before, a calcination temperature of $330\,^\circ\mathrm{C}$ (for $3\,\mathrm{h}$) is suitable to dehydroxylate and decarboxylate the hydrotalcite [29] and is also practicable for the one resulting from microemulsion.

During calcination in air at $330\,^\circ\mathrm{C}$ both products, labeled as ME-calc and co-calc, were converted into nearly amorphous, carbonate containing mixed oxides (Fig. 5.10) as described for CZA-calc (Chap. 4.2.2). These transformations were also observed by IR spectroscopy (see Fig. 5.9), where the M-OH band was replaced by the M-O band ($510\,\mathrm{cm^{-1}}$) and the carbonate band at $1360\,\mathrm{cm^{-1}}$ disappeared, whereas a
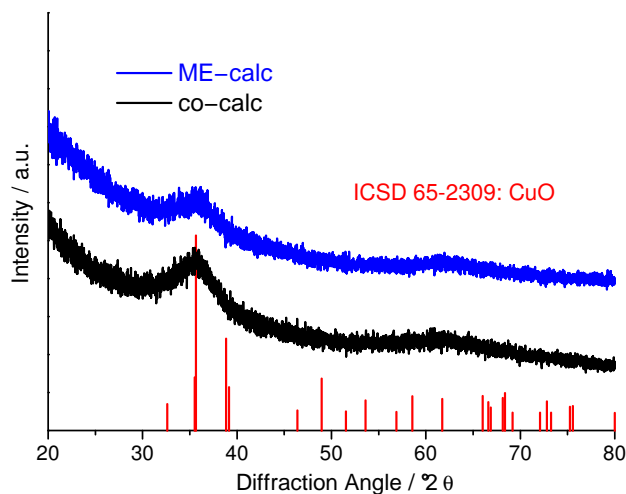
Figure 5.10: XRD patterns of samples after calcination: ME-calc and co-calc.

shoulder at $1480\,\mathrm{cm^{-1}}$ remained or evolved in the case of the ME sample which is assigned to HT-CO_3^{2-}. Furthermore, as the carbonyl band can not be observed in the IR spectrum of ME-calc, all remaining organic is, indeed, decomposed during calcination, as expected from TG-MS. ME-calc still shows the higher BET-SA (see Tab. 5.2), but a significant decrease was observed during the calcination process,

whereas the particle size stays nearly constant for both samples. Hence, the loss in surface area during calcination of ME-LDH is due to the decomposition of organic compounds probably sticking on the surface of the precursor (and increasing the surface area). Furthermore, SEM (Fig. 5.11) revealed that both samples maintained their morphology (Tab. 5.2) during calcination, showing again the similarity of the two materials.
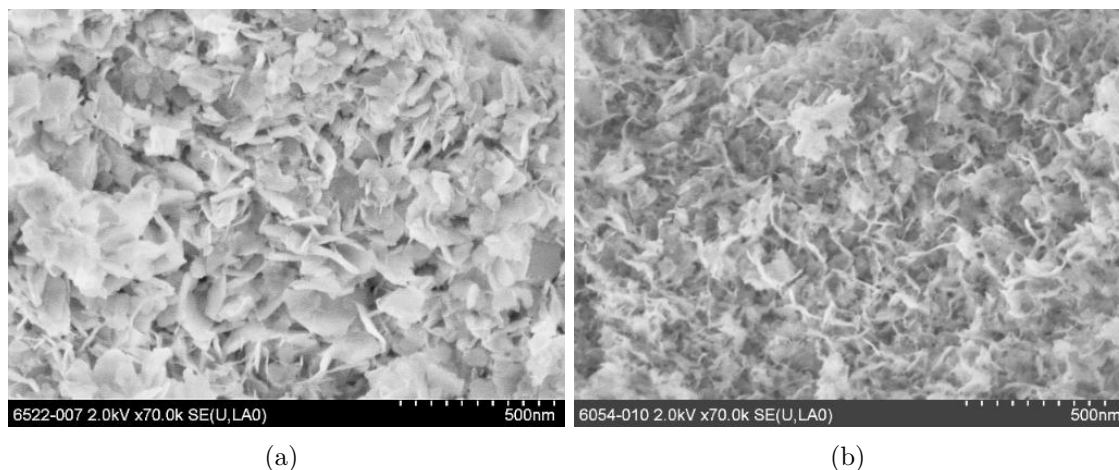
Figure 5.11: SEM images of calcined samples: (a) co-calc and (b) ME-calc.

In agreement with the observations in Chapter 4.2.2, after thermal treatment to 700 °C a crystalline product results for both samples (see Fig. 5.12) which only contains CuO (ICSD: 89-2529 [71]) and $ZnAl_2O_4$ (ICSD: 82-1036 [72]).

5.4 Characterization of reduced catalyst

The final Cu based ($Cu/ZnAl_2O_4$) catalyst, labeled as ME-red as well as co-red, resulted upon reduction of the Cu component of the calcined samples in hydrogen. The TPR profiles of both samples are depicted in Figure 5.13. Both profiles have a similar shape, but the temperature of the maximum reduction rate is significant lower for ME-calc, whereas the onset temperature is approximately the same. This observation is an indication for a particle size effect, as ME-calc, which is resulting from the calcination of the LDH precursor, exhibits the smaller secondary particles (aggregates of CuO nanoparticles and oxide matrix). The similar shape of the TPR profiles shows that the same Cu phase is present in both samples. By calibration
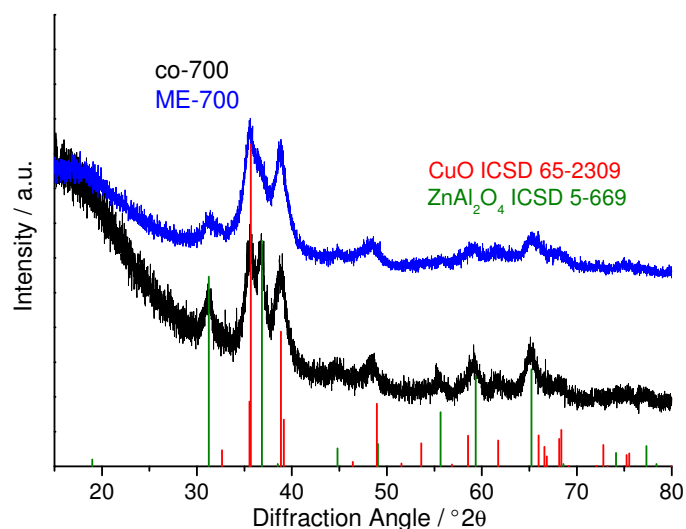
Figure 5.12: XRD patterns of samples after calcination in air to 700 °C.

using crystalline CuO it is possible to calculate the degree of reduction from the hydrogen consumption (ratio of formed Cu(0) to remaining oxidized Cu). Where co-calc is nearly completely reduced (98 %), a significant amount of CuO is not reduced for ME-calc (90 % reduced). In agreement to CZA-red (Chap. 4.4), the TEM images show that the small Cu particles are embedded within the oxide matrix (see Fig. 5.14). Whereas the Cu particles have a similar size of below 8 nm for both
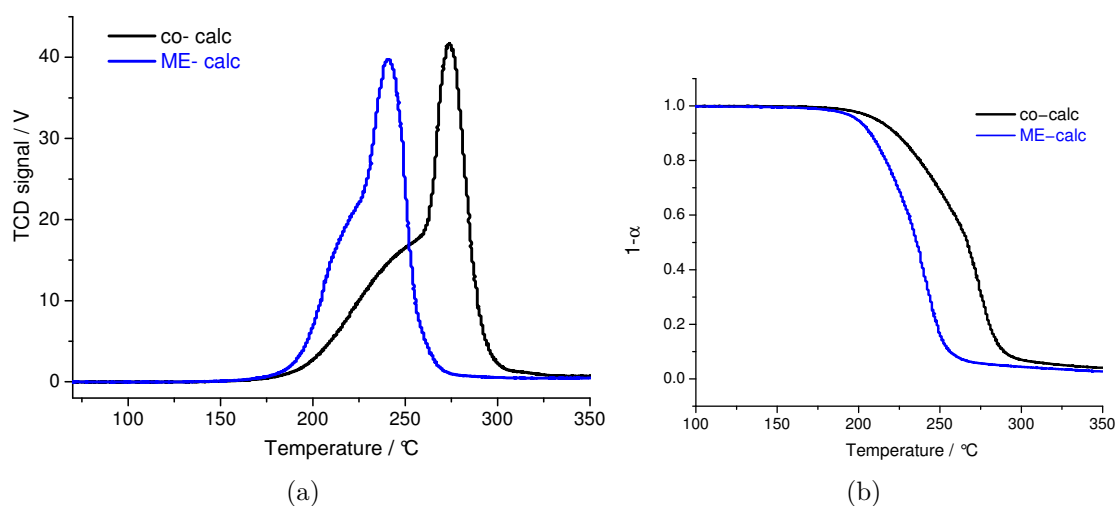
Figure 5.13: TPR of investigated samples: (a) reduction profiles, (b) reduction progress.
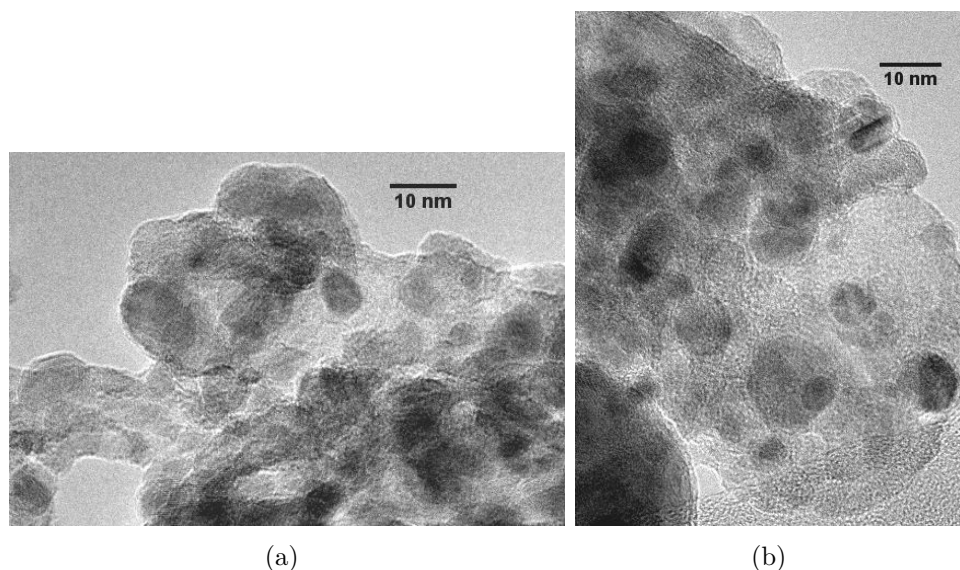
Figure 5.14: TEM images of reduced samples: (a) ME-red and (b) co-red; Cu^0-particles appear as dark spots, while the oxidic Zn-Al-oxide matrix is brighter.

samples (see Tab. 5.3 and Fig. 5.15), the secondary particles (aggregates of Cu nanoparticles and oxide matrix) appear less bulky for ME-red.
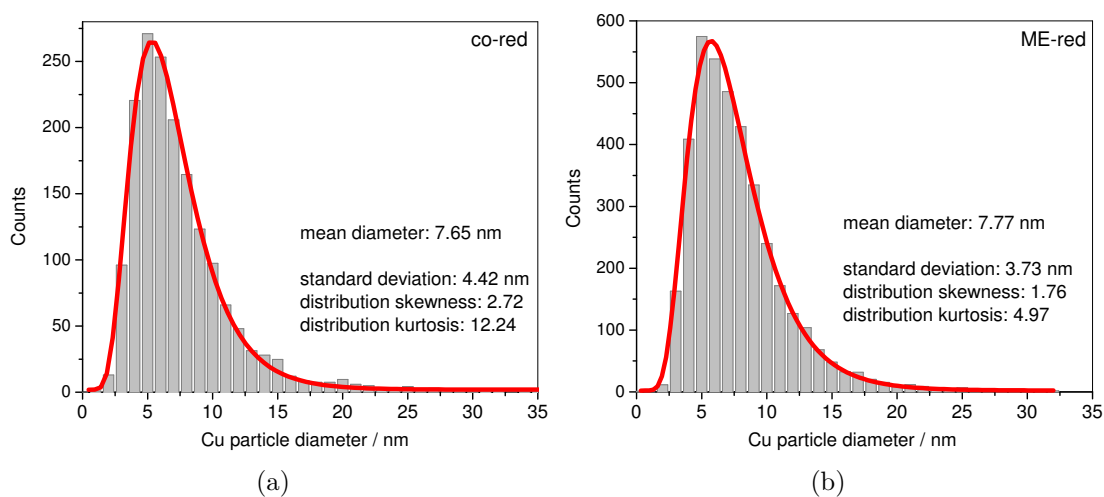
Figure 5.15: Cu particle size distribution after reduction determined from TEM images: (a) ME-red (3863 particles) and (b) co-red (1727 particles).

The Cu surface area (determined by N_2O-RFC [51]) of ME-red, is significantly higher (see Tab. 5.3) than the one of co-red. As described in Chapter 2.5.2, the

Table 5.3: Cu particle size (PS) measured by TEM (>1000 particles), Cu surface area measured by N_2O-RFC, interface ratio (IFR) and Cu surface area exposed to gas (Cu SA_{exp}) calculated from TEM images.

	Cu PS /nm	Cu SA /m^2g^{-1}	IFR /%	Cu SA_{exp} /%
ME-red	7.8	13.8±1.1	69	31
co-red	7.7	8.3±0.8	83	17

interface ratio (Eq. (2.13)) can be calculated from the experimentally measured Cu surface area and the average Cu particle diameter determined by TEM, values given in Table 5.3. In ME-red a higher fraction of the Cu surface is exposed to gas. Thus, by confining the growth of the LDH precursor particles, the microstructure of the resulting catalyst was modified to increase the exposed Cu surface area at the region of "buried" interfaces.

To compare their catalytical performance both catalysts were measured in methanol steam reforming. The results in Table 5.4 show a higher activity of ME-red, which is attributed to the improved microstructure implied by the application of the ME-technique during precursor preparation. However, the increase of activity (7 %) is low in relation to the difference in Cu surface areas (66 %). This result indicates

Table 5.4: Catalytic properties in methanol steam reforming.

	H_2 yield /$mmolg^{-1}h^{-1}$	X^1/%	S^2/%
ME-red	232.4	41.1	99.0
co-red	215.7	39.9	99.5

[1] conversion compared to feed methanol in %, [2] selectivity to CO_2 in %

that the intrinsic activity is not constant for a given Cu particle size, but depends heavily on the microstructure of the catalyst. In particular the interface interaction with the $ZnAl_2O_4$ matrix beneficially affects the exposed Cu surface. A stabilization of a very active form of non-equilibrium copper has been proposed as the reason for an analogous effect in methanol synthesis [38]. The present study suggests that a similar relation also exists for methanol steam reforming, which is also known as inverse methanol synthesis reaction.

5.5 Conclusion

We have demonstrated the possibility to apply a pH-controlled and scalable microemulsion technique to synthesize Cu,Zn,Al hydrotalcite by co-precipitation within ME-droplets. All organic compounds, which may remain during synthesis, are removed by calcination showing no detectable influence on the resulting catalyst. The BET surface area of the ME products (precursor and calcined one) is higher and the LDH particles are smaller than the ones of the conventionally co-precipitated reference catalyst. But the influence onto the particle growth during the precipitation process was not as successful as expected.

Nevertheless, the ME product exhibits less bulky secondary particles after calcination and reduction, i. e. aggregates of CuO or Cu nanoparticles and oxide matrix. The homogeneous distribution of all elements in the precursor state, which was observed for both systems, leads to small Cu particles below 8 nm for both samples. The catalyst resulting from ME exhibits indeed the higher Cu surface area, which is attributed to the smaller size of its $Cu/ZnAl_2O_4$ aggregates. Consequently, the ME product exhibits the higher catalytic activity in methanol steam reforming compared to the co-precipitation product. However, the increase in Cu surface area does not scale with the increase in activity. The lower intrinsic activity of the catalyst resulting from microemulsion indicates that the Cu surface area is not the only influencing parameter to gain high activity.

6 Substitution of Al by Cr and Ga - influence onto the catalyst microstructure and activity

6.1 Introduction

The hydrotalcite-like structure enables the insertion of a broad variety of cations, as just the M(II)/M(III) ratio is relevant to form the phase (see Chap. 1.2.1). Thus, these materials can be seen as a precursor system representing a powerful basis to study the effect of different promoter species on the redox- and catalytic properties of the Cu/ZnO/X catalyst independent of the Cu content preparation history.

Al in its oxidic form is supposed to be a multifunctional promoter, which is working as a separator as well as an important species on the interface to Cu [40, 41]. Two sample series were prepared using Cr and Ga as substituting elements for Al to investigate their effects onto the ex-LDH catalyst system to gain understanding of the functionality of Al and to insert new properties into the system which Al does not have. As already said in Chapter 1.1, the first catalyst applied for methanol synthesis was ZnO/Cr_2O_3 [1, 3], which was later replaced by the $Cu/ZnO/Al_2O_3$ catalyst. Furthermore, Ga_2O_3 was already investigated as replacement for Al_2O_3 [99].

Within this thesis a systematic investigation of the influences of chromium and gallium onto Cu based catalysts obtained from LDH precursors was done. For all prepared samples the general composition $Cu:Zn:(Al+X) = 50:17:33$, which was already used for CZA (see Chap. 4.2), was constant. In both cases CZA as well as the resulting calcined (CZA-calc) and reduced sample (CZA-red) are the starting point for the substitution investigation.

6.2 The effect of Cr substituting Al in LDH and resulting materials

Studies presented in literature [20, 100, 101] have already shown that it is possible to obtain LDH compounds with Cr as trivalent cation. Binary pure and well crystallized Cu/Cr LDH was prepared by Jiao et al. [100] with a molar ratio of $2:1$. Venugopal et al. [101] described ternary Cu-Zn-Cr$_2$O$_3$ catalysts with a constant Cu content of $50\,\text{mol}\%$ which were used for dimethyl ether synthesis. They found highly dispersed Cu species at high Zn/Cr ratios $(43:6)$, whereas a low Zn/Cr ratio $(27:21.5)$ led to the formation of Cu clusters. Nunan et al. [20] presented a Cs-doped Cu,Zn,Cr catalyst obtained from LDH, which was characterized by very poor crystallinity and small crystallites.

6.2.1 Choice of precipitation pH

As done for CZA (Chap. 4.1) the precipitation pH was determined carefully by titration at $25\,°\text{C}$. Figure 6.1 represents the titration curves of a Zn,Cr and a Cu,Zn,Al,Cr solution containing $15\,\%$ Cr. According to the investigation of the synthesis of Cu,Zn,Al-LDH (Chap. 4.1) Cu is precipitating around pH 4.5, Zn at pH 6.5 and Al at pH 5. Based on this knowledge, the data in Figure 6.1 show that Cr is precipitating around pH 5, showing a similar olation behavior like Al until pH 4. Accordingly, the precipitation pH value (pH 8) was not changed compared to Cu,Zn,Al-LDH (CZA). Thus, all resulting samples can easily be compared to each other.

6.2.2 Microstructure of Cr containing LDH precursor and calcined samples

For a detailed investigation of the effect of Cr on the Cu based catalysts, seven Cr containing samples were prepared and compared to the Cu,Zn,Al samples presented in Chapter 4. The overall composition was $\text{Cu}:\text{Zn}:(\text{Al}+\text{Cr}) = 50:17:33$, where Al was substituted in $5\,\%$ steps. The resulting precursor samples are labeled CrX, where X is the Cr content in at%, e.g. Cr5 for $5\,\text{at}\%$ Cr. The XRF results in Table 6.1 (calcined samples measured, for details see Chap. 3.5) show that the composition is
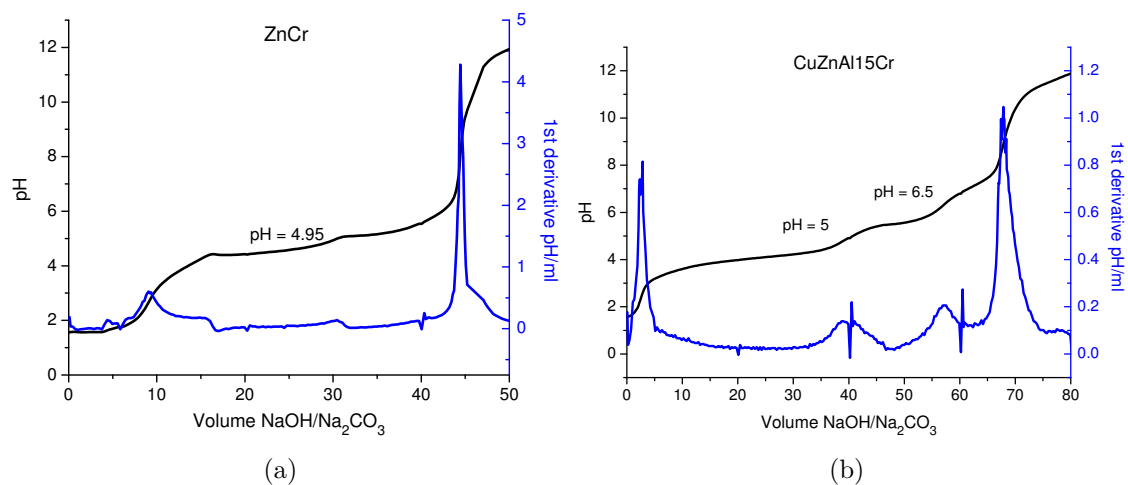
Figure 6.1: Titration curves of (a) mixed Zn,Cr solution and (b) mixed Cu,Zn,Al,Cr solution containing 15 at% Cr titrated with $NaOH/Na_2CO_3$ at 25 °C.

in good agreement with the nominal one used for preparing the starting solutions, especially the herein interesting Cr content. Unfortunately, in Cr20 the Cu content shows a quite high deviance from the nominal value. Furthermore, Cr33 still contains 1.5 at% Al. But nevertheless the small amount of Al is considered as minor influence on the catalyst behavior, especially as the properties are changed significantly.

Table 6.1: Metal contents in at% determined by XRF of calcined samples (nominal composition: $Cu:Zn:(Al+Cr) = 50:17:33$), deviances for all samples: $Cu \pm 0.08$ and $Zn \pm 0.04$.

	Cu	Zn	Al	Cr	Cr nom
CZA	50.6	15.9	33.5 ± 0.37	0	0
Cr5	50.9	15.8	28.7 ± 0.35	4.7 ± 0.08	5
Cr10	49.7	15.4	25.55 ± 0.34	9.35 ± 0.11	10
Cr15	50.9	15.7	19.1 ± 0.29	14.3 ± 0.13	15
Cr20	47.25	17.1	15.25 ± 0.28	20.4 ± 0.16	20
Cr25	50.55	16.2	9.25 ± 0.22	24.0 ± 0.16	25
Cr30	50.3	16.6	4.2 ± 0.16	28.9 ± 0.18	30
Cr33	50.1	16.5	1.5 ± 0.12	31.9 ± 0.19	33

The structural investigation by XRD, presented in Fig. 6.2 indicates a hydrotalcite structure for all samples, showing a significant change of the pattern for Cr contents ≥ 15 at%. By incorporation of Cr into the hydrotalcite lattice an increased M–M distance is expected, as the ionic radius of Cr^{3+} (0.615 Å) is larger than the one of
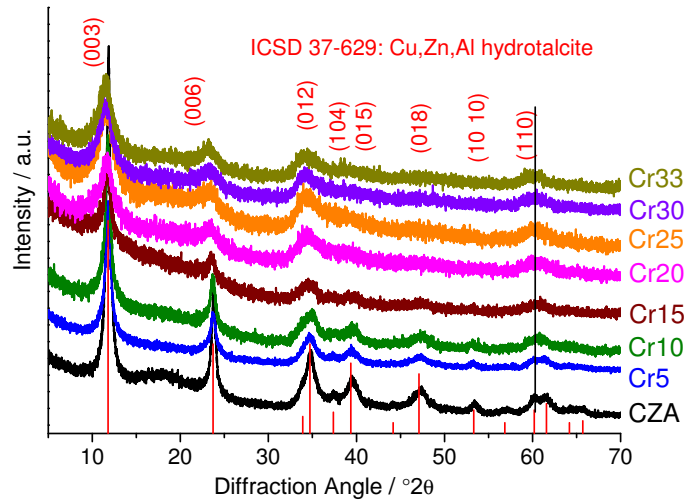
Figure 6.2: XRD patterns of Cr series in comparison to hydrotalcite-like structure.

Al^{3+} (0.535 Å) [102]. The (110) lattice plane is perpendicular to the brucite layer, hence the change of its peak position would give information about the M–M distance within the layers. The crystallinity is decreasing with increasing Cr content, which is in agreement with observations described in literature [20, 101]. Therefore, a quantitative determination of the peak shift is not possible, but one can assume by visual comparison that the (110) reflection is shifted to lower angles or a larger *d*-spacing. Furthermore, as no other crystalline phase is observed the incorporation of Cr into the LDH structure is very likely, especially as Cr33 still shows the hydrotalcite structure. This result shows, together with the composition derived by XRF, that the precipitation is effective, and we can conclude that Cr containing LDH was successfully prepared by co-precipitation.

The average particle size of the LDH platelets (determined from SEM images; see Tab. 6.2) is nearly constant for small Cr contents ($\leq 10 \, at\%$) and decreasing to $\approx 40 \, nm$ for higher Cr contents. This observation is in agreement with the ob-

Table 6.2: Average particle sizes (PS) determined from SEM images (>150 platelets measured); range of PSD: max - min particle size.

	CZA	Cr5	Cr10	Cr15	Cr20	Cr25	Cr30	Cr33
PS / nm	65	69	66	60	43	43	36	39
range of PSD	91	109	132	88	62	85	58	84

servations from the XRD patterns and explains the apparently lower crystallinity manifested in the broader reflections for higher Cr contents. Throughout the sample series, the homogeneity of the elemental distribution is fluctuating slightly, with a higher inhomogeneity for Cr10 and Cr15 (see Fig. A.11 and Fig. A.12 in Appendix A.4). In general, the platelet-like morphology is maintained for the Cr substituted LDH compounds but with higher Cr loadings ($\geq$20 at%) the packing of the platelets is getting more compact; exemplarily shown for Cr5, Cr15, Cr20 and Cr33 in Figure 6.3.
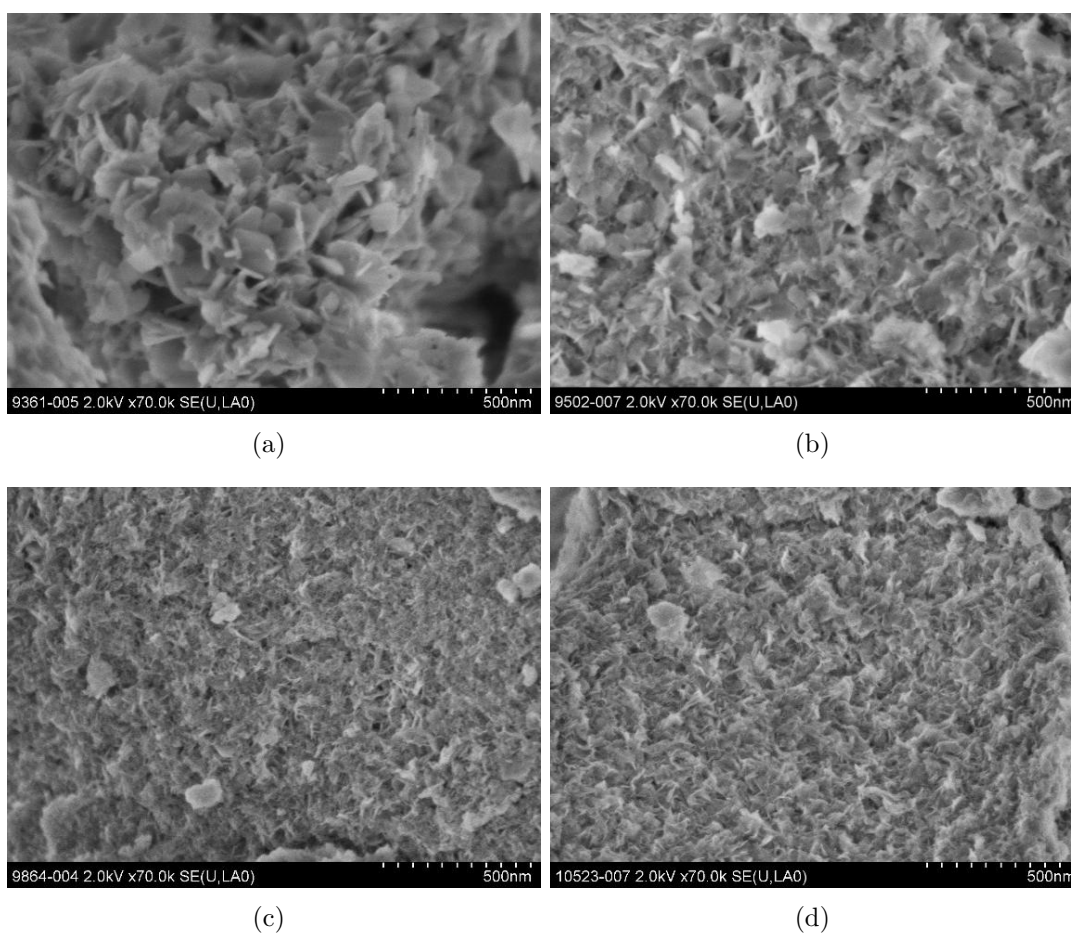
Figure 6.3: SEM images of Cr containing LDH samples: (a) 5 at% Cr, (b) 15 at% Cr, (c) 20 at% Cr, (d) 33 at% Cr.

The plot of BET surface areas versus Cr content, as shown in Figure 6.4(a), results in a volcano-like trend with a maximum for Cr15, which seems to be a contradiction to the particle size evaluation determined from SEM images (Tab. 6.2).
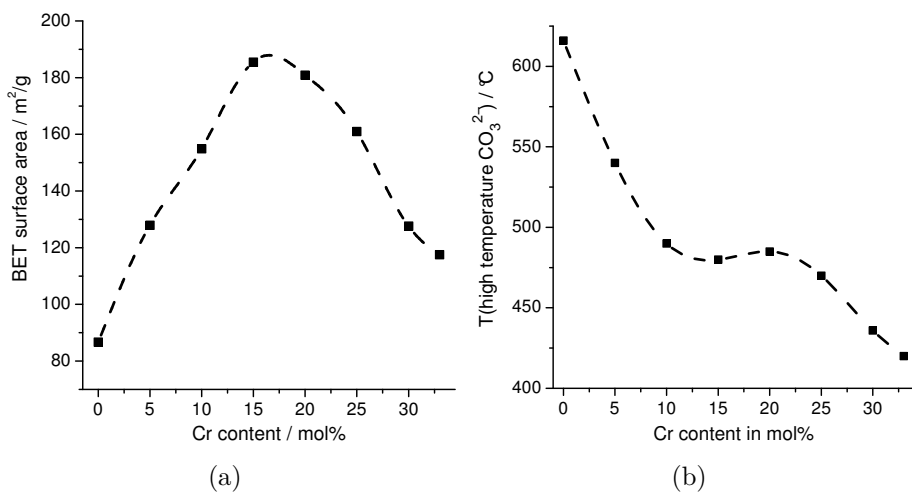
Figure 6.4: Characteristic properties in dependence of Cr content: (a) BET surface area; (b) decomposition temperature of HT-CO$_3^{2-}$.

Inspection of the isotherms reveals that with substitution of Al by Cr the adsorption-desorption characteristics are changed significantly for ≥ 15 at% Cr which is in agreement with the observations of XRD and SEM, suggesting the presence of two groups of samples. The isotherm is changed from type IV (CZA) to type V for Cr ≥ 15 at% (compare adsorption isotherms Fig. 6.5), which is typical for weak attractive interactions between the adsorbent and the adsorbate [63]. Even more pronounced is the change of the hysteresis shape from H1 for small Cr contents to H2 for samples ≥ 15 at%. The latter is described for a disordered pore structure with important network effects [63]. This changed porosity is in agreement with the "compaction" of the platelets observed by SEM (Fig. 6.3). Thus, the trend of BET surface area can be explained with the changes in the adsorption-desorption characteristics. Until a Cr content of 15 at%, where the isotherm is still type IV and the hysteris type H1, the development of the BET surface area is in correlation with the particle sizes as external and internal area are measured. For higher Cr ratios the pore structure gets more and more disorderd yielding in the described compact microstructure as at a certain size of the LDH platelets their packing changes. Probably due to a blocking of the so called internal surface only the external area is measured which results in the decrease of the BET surface area for increasing Cr content.

The investigation of the thermal behavior gives a first direct hint to the drastic influences of Cr onto the LDH system. As observed for CZA, the decomposition
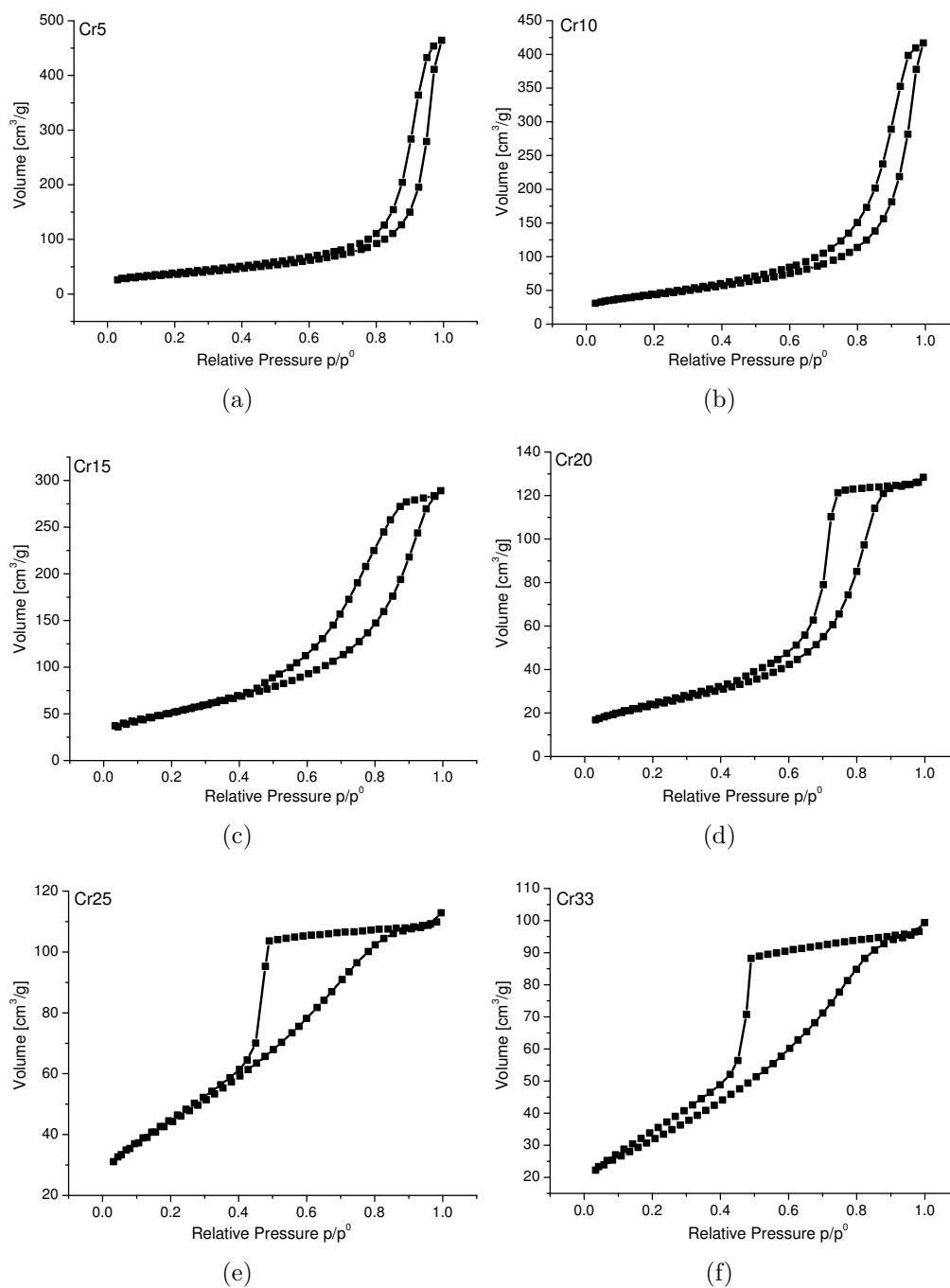
Figure 6.5: N_2 adsorption-desorption isotherms of Cr substituted LDH samples measured at $-196\,°C$: (a) 5 at% Cr, (b) 10 at% Cr, (c) 15 at% Cr, (d) 20 at% Cr, (e) 25 at% Cr, (f) 33 at% Cr; y-axes scaled differently.

of the Cr containing LDH samples (see Appendix A.4 Fig. A.10) are dominated by the decomposition of the hydrotalcite structure at low and the decomposition of the HT-CO_3^{2-} at higher temperatures. As illustrated in Figure 6.4(b) the decomposition temperature of this HT-CO_3^{2-} significantly decreases with increasing Cr content with a local minimum at $15\,at\%$ Cr, while the weight loss is constant at $5 - 6\,\%$. As already claimed elsewhere [31], a higher decomposition temperature is an indicator for strong interfaces and grain boundaries formed during the first decomposition step. Accordingly, the lower thermal stability observed for the Cr containing hydrotalcite results from a weaker interface contact of the Cu phase with the Zn-(Al,Cr) matrix. Thus, Cr seems to loosen the microstructure of the mixed oxides resulting from LDH compounds.

Furthermore, the TG-MS analysis shows that the temperature of $330\,°C$, used for the calcination of CZA (to obtain CZA-calc), is also applicable for this sample series, as for all cases the dehydroxylation and decarboxylation is finished at this temperature. Similar to CZA-calc, the calcined Cr containing samples will be labeled as Cr*X*-calc in the following.
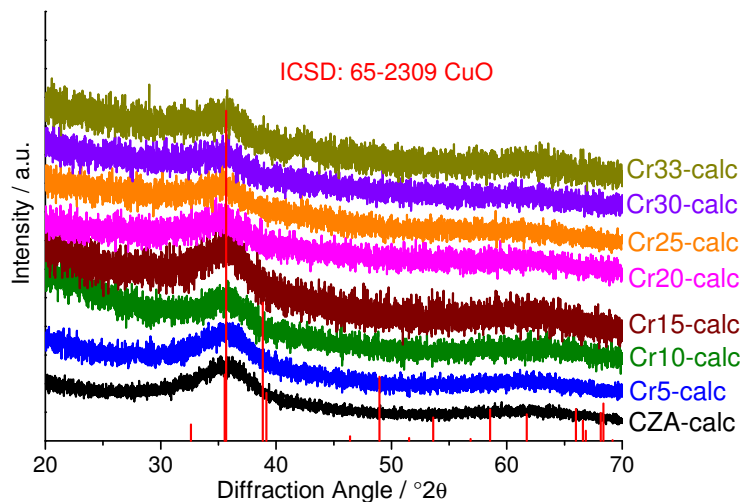
Figure 6.6: XRD patterns of Cr samples after calcination at $330\,°C$.

As shown in Figure 6.6 and presented already for CZA-calc in Chapter 4.2.2 all calcined samples can be described as nearly amorphous mixed oxides, containing $7 - 8\,wt\%$ HT-CO_3^{2-} (calculated from TG-MS curves). By SEM it was shown that there are no significant changes of the morphology compared to the LDH samples, exemplarily depicted in Figure 6.7 for Cr20-calc and Cr33-calc. Additionally, the

(a)   (b)
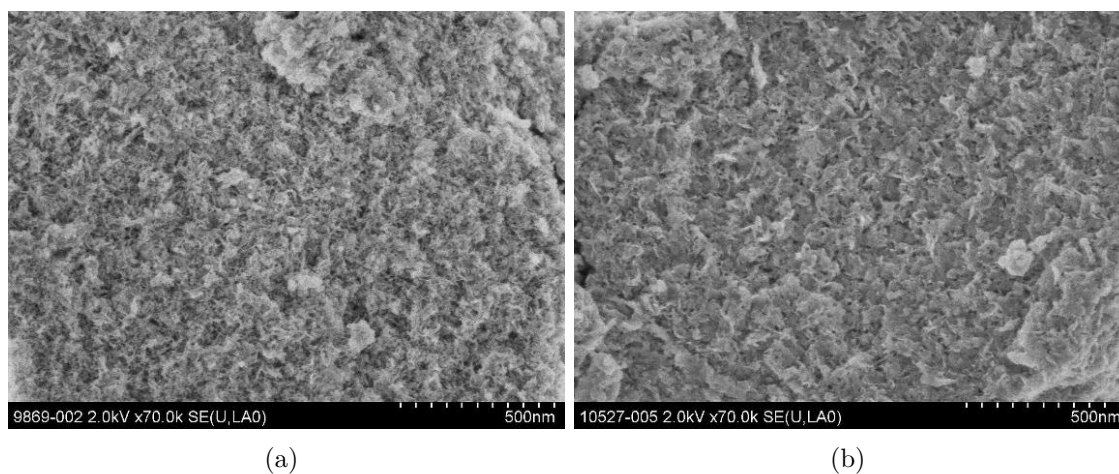
Figure 6.7: SEM images of calcined samples: (a) Cr20-calc, (b) Cr33-calc.

trend of the BET surface area is quite similar to the precursor samples, as again a volcano-like curve is obtained if the BET surface area is plotted versus the Cr content (Fig. 6.8), again with a maximum for 15 at% Cr.
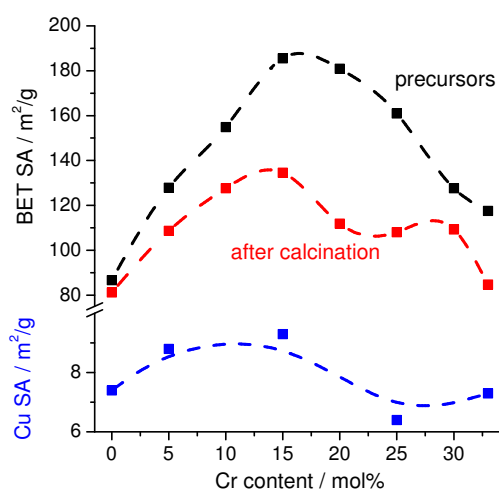
Figure 6.8: BET surface area of LDH and calcined samples and Cu surface area after reduction in dependence of Cr content.

Furthermore, analogous to CZA-700, Cr33-700, the sample after calcination at 700 °C, is characterized by crystalline CuO (ICSD: 89-2529 [71]) as well as $ZnCr_2O_4$ spinel (ICSD: 82-1036 [72]), as illustrated in Figure 6.9. As expected the quaternary samples, exemplarily shown for Cr15 (Fig. 6.9), show a mixed $Zn(Al,Cr)_2O_4$ spinel.

91

In CZA-calc the presence of $ZnAl_2O_4$ spinel was proven by NEXAFS Chap. 4.2.2. Therefore, in analogy to the Cr-free system the local environment of the CrX-calc samples can be described as being CuO and $Zn(Al,Cr)_2O_4$ spinel.
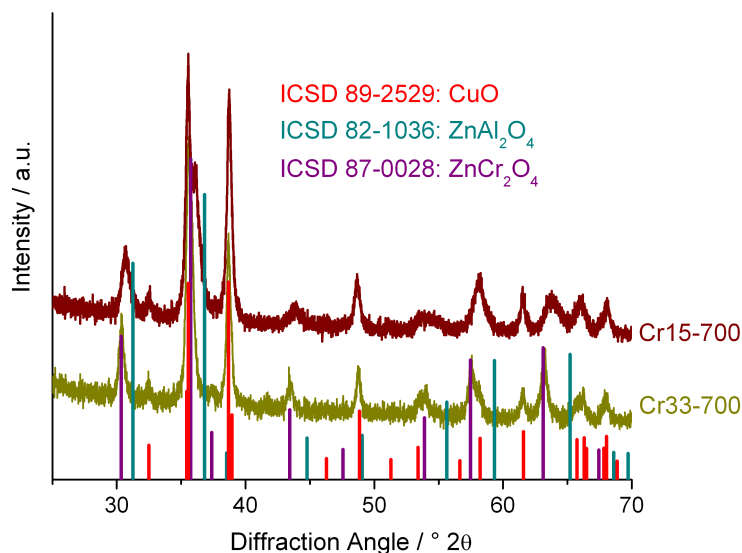
Figure 6.9: XRD pattern of Cr15-700 and Cr33-700, samples after calcination at 700 °C.

6.2.3 Investigation of reduction behavior and microstructure of resulting catalysts of Cr containing ternary and quaternary samples

The investigation of the reduction behavior of CrX-calc samples is based on the knowledge gained from the reduction of CZA-calc (Chap. 4.3). As shown in Figure 6.10 the TPR profiles gradually change with the insertion of Cr. In agreement with the two groups of samples, already observed for the precursor samples (XRD, SEM and N_2 physisorption), a big influence onto the reduction temperature (see Tab. 6.3) and mechanism can be observed for small Cr contents (≤ 15 at%), whereas smaller differences result with increasing substitution of Al.

As described in Chapter 4.3 for CZA-calc the higher reduction temperature (compared to the conventionally prepared catalyst system) is caused by the necessary separation of reducible and irreducible phases due to the homogeneous elemental distribution and the strong interaction of "CuO" with the Zn-Al matrix, which has
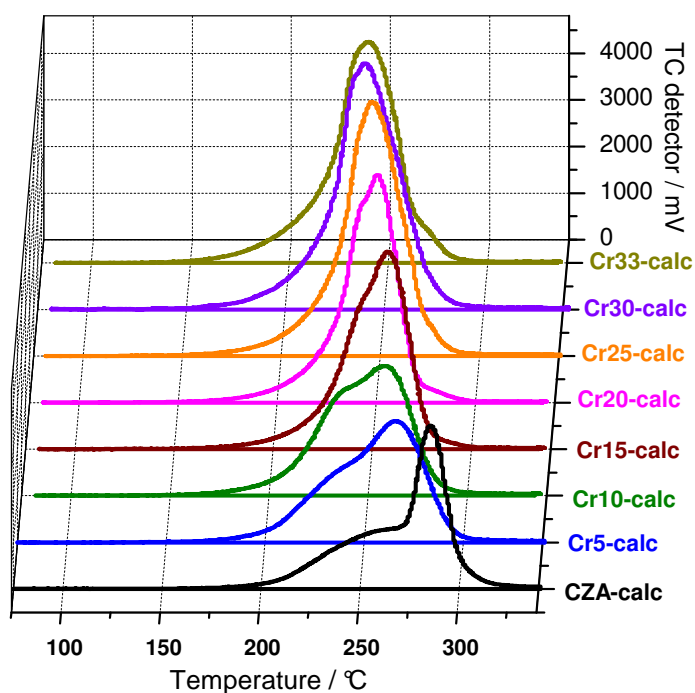
Figure 6.10: TPR profiles of CrX-calc samples (parameters set to K $= 106 - 108\,$s, P $= 10.1 - 10.8\,$K).

to be overcome before reduction. As was already shown by TG-MS this interaction is weaker when Cr is present, and is further weakend with increasing Cr content. Accordingly, the lower reduction temperature is explicable by an easier diffusion within the solid due to the weaker interaction.

Table 6.3: TPR of Cr series: T_{max} and hydrogen consumption in relation to present CuO.

at% Cr	T_{max} / $^\circ$C	H_2/CuO / %
0	285	98
5	266	105
10	258	113
15	258	118
20	251	138
25	246	142
30	241	147
33	240	150

93

Interestingly, the amount of consumed H_2 relative to the present amount of CuO (Tab. 6.3) is higher than 100% already for Cr5-calc and increases to 150% for Cr33-calc, indicating that Cr plays an active role within the reduction process.

The apparent activation energies of the reduction were determined for CrX-calc (with $X = 5, 15, 25, 33$) as described in Chapter 2.2 and as done for CZA-calc in Chapter 4.3. The results are given in Table 6.4. A lower value is observed by the introduction of Cr into the catalyst. But, nevertheless, from the range of the activation energies as well as the similarity of these catalysts with CZA-calc, a CuO-like identity within the $Zn(Al,Cr)_2O_4$ matrix can be assumed.

Based on the two step reduction of CuO proved for CZA-calc (see Fig. 4.15(a) in Chap. 4.3), the qualitative peak deconvolution for the Cr containing samples, depicted in Figure 6.11 for $X = 5, 15, 25$ and 33, shows two additional peaks. Assuming a
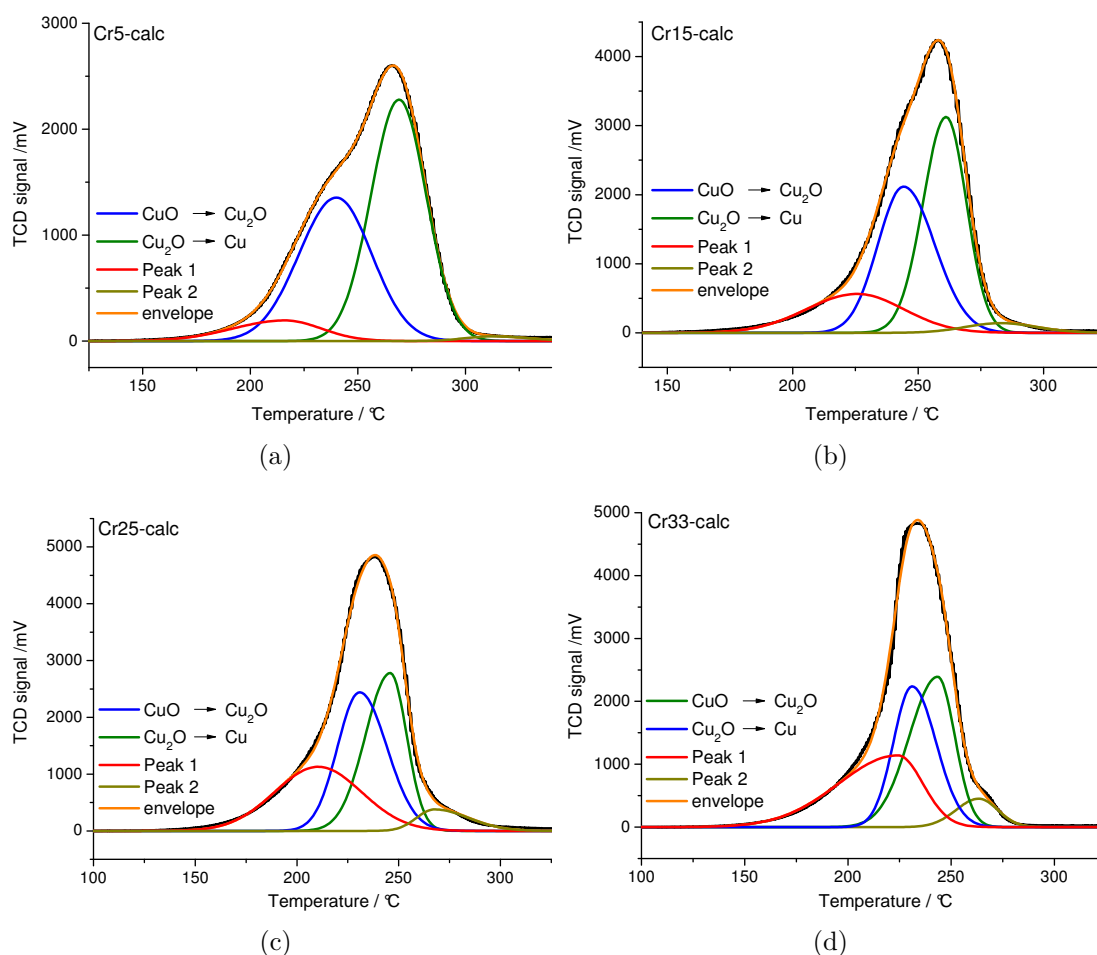
Figure 6.11: Peak deconvolution of TPR profiles: (a) Cr5-calc, (b) Cr15-calc, (c) Cr25-calc, (d) Cr33-calc.

nearly complete reduction of CuO, as observed for CZA-calc, the assignment of the deconvoluted peaks was done by comparison of the experimental and stoichiometric hydrogen consumption. Thus, the main peaks of the TPR signal belong to the CuO reduction and the additional reduction peaks are on the low and high temperature side of the main peaks. There are several studies in literature reporting about Cr containing catalysts as well as the oxidation behavior of Cr_2O_3. For example, Apte et al. [103] reported about the conversion of Cr_2O_3 to hexavalent Cr (CrO_3) when heated in the presence of oxygen at temperatures of $200 - 300\,°C$. Accordingly, for Cr*X*-calc the formation of Cr(VI) seems to be likely, as they were obtained after calcination in air at $330\,°C$. The presence of Cr(VI) was also observed by Gaspar and Dieguez [104] by diffuse reflectance UV-vis spectroscopy in the calcined state of Cr/SiO_2 catalysts. Complete reduction to Cr_2O_3 by hydrogen required temperatures above $350\,°C$. Furthermore, Crivello et al. [105] investigated Cr/Cu/Mg mixed oxides derived from hydrotalcite-like compounds. By XPS they observed the presence of Cr^{6+} besides Cr^{3+} after calcination at $450\,°C$, whereas after reduction in hydrogen at $300\,°C$ just Cr^{3+} was found. Based on these studies the additional reduction peak at the low temperature side of the CuO reduction (peak 1) is attributed to the reduction of Cr^{6+} represented by the reaction $2\,CrO_3 + 3\,H_2 \longrightarrow Cr_2O_3 + 3\,H_2O$. To verify the presence of Cr^{6+} the Cr L-edge NEXAFS spectrum was measured of Cr33-calc. The result is presented in Figure 6.12. By comparison to the spectrum of Cr_2O_3 as
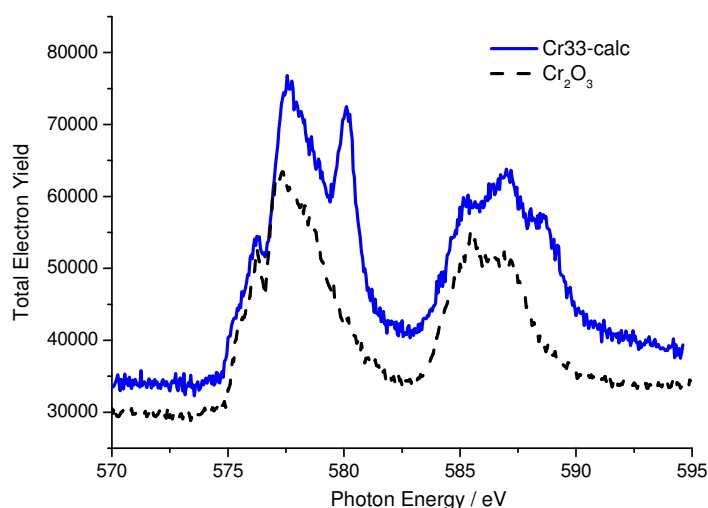
Figure 6.12: Cr L-edge NEXAFS spectra of Cr33-calc and Cr_2O_3 as reference for Cr^{3+}.

reference for Cr^{3+} and a NEXAFS study from literature [106] the presence of Cr^{6+} besides Cr^{3+} is clearly proven. By comparison of the experimental and stoichiometric hydrogen consumption during reduction and assuming the complete reduction of Cr^{6+}, it was possible to estimate the fraction of Cr^{6+} in all calcined catalysts to approximately 50 % of the present Cr content, evaluated by XRF analysis (Tab. 6.1). We suppose that Cr^{6+} is also decomposed in oxygen at higher temperatures, as after calcination at 700 °C no indication was found for its presence.

With regard to the high temperature reduction peak, Venugopal et al. [101] observed a single reduction peak at 325 °C for a ZnO/Cr_2O_3 catalyst which they proposed as the complete reduction of Cr_2O_3 finished at 350 °C. Accordingly, we assume this peak can be assigned to the reduction of Cr^{3+}. The quantification of the deconvolved peak allows for the estimation that in all samples 26 at% of Cr^{3+} were reduced to "CrO".

Moreover, the peak deconvolution showed that the more Cr is present the less stable is Cu_2O which was proven as intermediate during the reduction of CZA-calc. In Chapter 4.3 this stability was attributed to the hindered diffusion within the solid state due to the homogeneous distribution and the strong interaction effect. As already shown, the interaction of Cu and the Zn-X matrix is less strong in the Cr containing samples, therefore the observed lower "stability" of Cu_2O is probably due to an easier diffusion within the solid state. After all, a complete reduction of CuO accompanied by major changes within the oxide phase can be concluded from the TPR investigations.

As done for CZA-calc, the Cr containing samples were also investigated by TG-DSC during the reduction in hydrogen (curves represented in Fig. A.13 in Appendix A.4) to determine the fraction of $HT\text{-}CO_3^{2-}$ present in the reduced catalyst (see Tab. 6.4). Interestingly, both ternary samples are characterized by the same amount of carbonate present in the reduced state. On the other hand, the quaternary samples contain significantly less carbonate after reduction.

Similar to CZA-red, the Cr containing catalysts resulting after reduction of Cr*X*-calc will be labeled as Cr*X*-red in the following. The Cu surface area of Cr*X*-red (X = 5, 15, 25, 33) was determined by N_2O-RFC (Tab. 6.4). In general, it is just slightly influenced by the insertion of Cr, with a similar behavior as observed for the BET surface area as a maximum value results for Cr15-red (see Fig. 6.8). The TEM investigation, exemplaryly done for Cr15-red and Cr33-red, showed an increasing

Table 6.4: Activation energy of reduction and properties of resulting catalysts: HT-CO$_3^{2-}$ content is determined from TG-DSC curves, Cu surface area (SA) and particle size (PS) by N$_2$O-RFC and TEM particle size evaluation, interface ratio (IFR) is calculated from theoretic Cu surface area based on TEM particle size.

at% Cr	E$_A$ /kJ/mol	Cu SA /m^2/g	HT-CO$_3^{2-}$ /wt%	Cu PS /nm	IFR /%
0	60 ± 3	7.4 ± 0.7	4.8	7.0	85
5	57 ± 5	9.0 ± 0.7	2.2	n.m.	n.m.
15	51 ± 4	9.3 ± 0.8	1.3	14.2	61
25	53 ± 3	6.4 ± 0.6	1.9	n.m.	n.m.
33	53 ± 4	7.3 ± 0.7	4.8	24.1	43

Cu particle size with increasing Cr content (see Tab. 6.4 and PSD in Fig. A.14 in Appendix A.4). The easy growth of the Cu particles is again attributed to the weaker interaction of the Cu phase and the oxide. Despite this the microstructure of the TEM images, depicted in Figure 6.13, illustrate a genral similarity of the Cr containing catalysts with CZA-red as the Cu particles are embedded within a mostly amorphous, oxidic matrix. As described in Chapter 2.5.2, the interface ratio

(a)   (b)
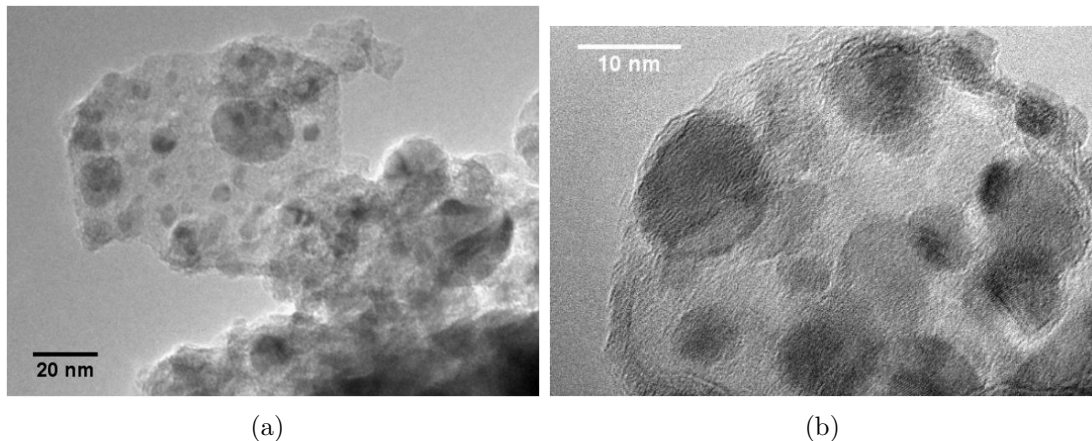
Figure 6.13: TEM images of Cr containing catalysts: (a) Cr15-red, (b) Cr33-red; highly embedded Cu^0-particles (dark spots) in oxidic matrix.

(Eq. (2.13)) can be calculated from the experimentally measured Cu surface area and the average Cu particle diameter determined by TEM, values given in Table 6.4. With increasing particle size the embedment of the Cu particles is partially released as expected from lower reduction temperature and the less strong interaction of Cu

and the Zn-Cr matrix in comparison to Al. Accordingly, in analogy to CZA-red the resulting Cr containing Cu based catalysts can be described as metallic Cu particles dispersed in a $Zn(Al,Cr)_2O_4$ spinel-like matrix, which exhibit a clear trend in Cu particle size and embedment as a function of Cr content. In Chapter 4.4 the "stability" to air of the final catalyst obtained from LDH precursor was shown. For Cr containing catalysts, despite all the changes of the catalyst microstructure, this "stability" is maintained after reduction (compare Fig. A.15 in Appendix A.4).

Furthermore, all catalysts were investigated for their catalytic activity in methanol synthesis, the results are presented in Figure 6.14(a) (comparison of activity versus time on stream presented in Fig. A.16 in Appendix A.4). In other studies it was shown, that the lower the reduction temperature during catalyst activation the higher is the activity of the derived catalyst [74, 107]. Conversely, this sample series,
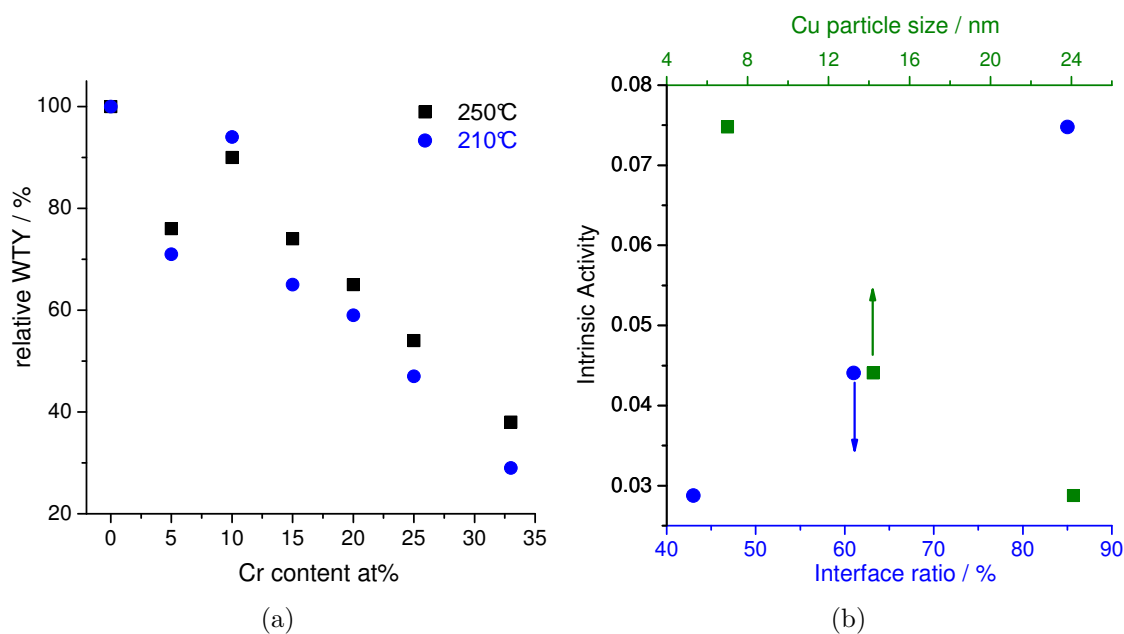
Figure 6.14: Comparison of catalytic activity in methanol synthesis: (a) average weight time yield (WTY), (b) intrinsic activity and interface ratio versus Cu particle size.

characterized by a decreasing reduction temperature, shows a decreasing activity with increasing Cr content. Furthermore, no correlation of the catalytic activity with the exposed Cu surface (Tab. 6.4) could be observed. On the other hand, the catalytic properties can be nicely correlated with the observed decreasing strength

of the interaction of Cu and the oxide matrix. Furthermore, the lower activity of Cr5-red compared to Cr10-red can not be ignored as we already showed that the sample series is composed of two groups of samples. That means that two effects are competing for small Cr contenst: the gradual changes by the stepwise substitution of Al by Cr and the significant changes in their precursor chemistry.

This result indicates that Cu alone is not responsible for catalytic activity, but that also a special interaction to the oxide phase is required. Consequently, by increasing the Cu particle size with increasing Cr content due to the weaker interaction the intrinsic activity (activity normalized by Cu surface area) is decreased, as depicted in Figure 6.14(b). A similar correlation of the intrinsic activity was also observed for the interface ratio (Fig. 6.14(b)). No pronounced loss of Cu surface area occur for the larger particles, because the show a higher fraction of exposed surface relative to the interface to the oxide matrix. However, this effect cannot compensate the lower intrinsic activity of the less embedded particles.

To complete this study TPR-TPO cyclization experiments were carried out for CrX-calc with $X = 5, 15, 25, 33$ (see Fig. 6.15), as presented for CZA-calc in Chapter 4.4. The obtained results (summarized in Table A.3 in Appendix A.4) are good agreement with the described and explained reduction behavior. A large difference in T_{max} of first and second reduction underlines the strong Cu-oxide interactions in the calcined material. With increasing Cr content T_{max} of TPR2 is increasing and for 25 and 33 at% Cr even matches T_{max} of TPR1. The TPO of CZA-red led to an annihilation of the high embedment of Cu particles (compare Chap. 4.4) resulting in a lower temperature and less stable Cu_2O intermediate for the rereduction afterwards. For Cr containing catalysts the embedment is already smaller after the first reduction. Accordingly, with increasing amount of Cr the loss of strong Cu-oxide interactions due to TPO-TPR treatment becomes less significant as the resulting microstructure of the Cu based catalyst does hardly change. The smaller hydrogen consumption observed for TPR2 is attributed to an incomplete oxidation during TPO treatment, as was shown for the CZA catalyst (Chap. 4.4). The Cu surface area after TPO-TPR treatment of Cr33-red, which amounts to $4.5\,m^2/g$, is significant lower in comparison to the freshly reduced catalyst (Tab. 6.4), whereas it was found to be doubled for the CZA catalyst (see Tab. 4.6 in Chap. 4.4). Thus, TPR-TPO-TPR of this catalyst only leads to sintering effects and no other microstructural changes could be observed. Accordingly and in agreement with the
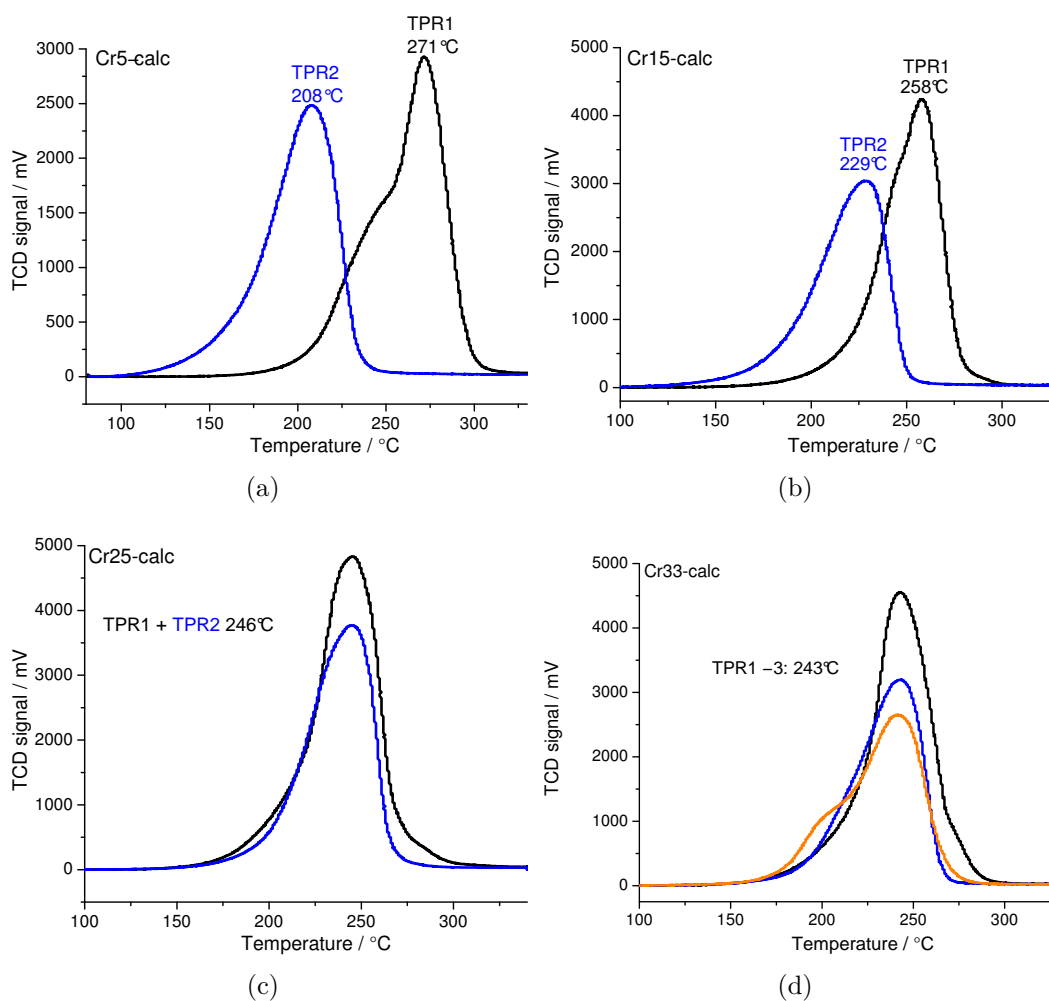
Figure 6.15: TPR profiles of TPR-TPO-TPR experiment: (a) Cr5-calc, (b) Cr15-calc, (c) Cr25-calc, (d) Cr33-calc ($K = 106 - 109\,s$, $P = 10.1 - 10.9\,K$).

observations for CZA-red, repeated TPR-TPO cycles for Cr33-red do not lead to further significant changes, indicating a reversible redox behavior.

6.2.4 Conclusion

The stepwise substitution of Al by Cr has shown that it is possible to prepare quaternary Cr containing LDH precursor for Cu based catalysts. The insertion of Cr is strongly influencing the adsorption-desorption characteristics of the resulting LDH, where the BET surface area shows a volcano-like trend with increasing Cr content. Furthermore, the samples were characterized by a homogeneous distribution

of the elements. Througout the precursor characterization two families of samples were found showing significant different properties for small Cr contents ($\geq 15\,\text{at}\%$) compared to high Cr contents. TG-MS measurements first indicated a lower strength of the interaction of Cu with the mixed oxide matrix, indicated by a decreasing decomposition temperature of HT-CO_3^{2-} with increasing Cr content. After decomposition in air carbonate-modified mixed oxides were obtained, like described for CZA-calc.

Similar to the reduction of CZA-calc, the reduction of CrX-calc led to Cu particles embedded within an $Zn(Al,Cr)_2O_4$ spinel-like matrix. The reduction profiles themselves were gradually changed by the insertion of Cr into the catalyst system. Interestingly, the hydrogen consumption was higher than required for the reduction of the present CuO. The peak deconvolution of the TPR profiles resulted in two peaks additional to the two step reduction of CuO. These peaks were attributed to a reduction of Cr^{6+}, formed during the calcination, as well as a partial reduction of Cr^{3+} occurring besides the CuO reduction by comparison to studies in literature. In the CZA catalyst system the separation of reducible and irreducible phases during hydrogen treatment is mainly determined by diffusion limitation within the solid state. With increasing Cr content this diffusion hindrance is decreased due to the weaker interaction of Cu to the Zn-Cr matrix, resulting in the observed lower reduction temperature. Besides, a lower "stability" of the Cu_2O intermediate was found with increasing Cr content, which is also explicable with the lower interaction implemented by Cr, leading to an easier diffusion within the solid state. In general, the TPR investigation of the Cr containing samples showed that the reduction of CuO is accompanied by major changes of chromium oxide. Compared to the inert matrix in CZA-calc, the reactive Cr matrix promotes the rearrangements in the solid state and does not hinder the Cu reduction as effectively as $ZnAl_2O_4$. This effect is also responsible for a pronounced growth of the Cu crystallites during reduction if Cr is present.

In agreement with the BET surface area, the highest Cu surface area was found for Cr15-red, though the deviances throughout the sample series were small. The loss of Cu surface area due to Cu particle growth is partially compensated by a less strong embedment of the Cu particles. Furthermore, with increasing Cr content a decreasing catalytic activity was observed. Thus, the catalytic activity does not scale with the Cu surface area. The decreasing activity is rather attributed to a decreasing

intrinsic activity. This sample series shows nicely that a high interaction to the oxide is necessary to gain stability and activity of the Cu phase. This necessary interaction is weakened, if during the reduction of CuO, seen as the most important step of the catalyst preparation, the oxide matrix itself is changed significantly by redox processes. Furthermore, the lower activity of Cr5-red compared to Cr10-red shows that the precursor phase is highly influencing the resulting catalyst, so called chemical memory. For small Cr contents two effects are competing: the gradual changes by the stepwise substitution of Al by Cr and the significant changes in their precursor chemistry. As a research perspective a second generation of Cr containing ex-LDH catalysts should be prepared with $< 10\,\mathrm{at\%}$ Cr with smaller steps of the Cr content between each sample.

In contrast to the CZA catalyst system, an additional TPO-TPR treatment is less effective for Cr containing catalysts as the resulting microstructure of the Cu based catalyst does hardly change as the embedment, which was decreased in case of CZA catalyst, is already smaller after the first reduction. Thus, TPR-TPO-TPR of this catalyst only leads to sintering effects and no other microstructural changes could be observed.

To summarize, this sample series shows that it is possible to prepare a series of Cu based catalysts with the same preparation history, characterized by a homogeneous elemental distribution and a similar Cu surface area, but varying interactions between Cu and the oxide, resulting in significant differences in catalytic performance. Correlations of the intrinsic activities with decreasing Cu particle size and increasing interface ratio with the oxide component could be found. These findings are in agreement with recent observations, that the intrinsic activity of Cu is related to defects and strain in the Cu particles [15, 32], which exhibit a larger concentration on small particles and are likely to be "pinned" at the metal-oxide interface [38].

6.3 The effect of Ga substituting Al in LDH and resulting materials

Studies presented in literature have already shown that it is possible to obtain LDH compounds with Ga as trivalent cation. Nunan et al. [20] presented a Cs-doped Cu,Zn,Ga catalyst obtained from LDH, which was characterized by similar properties like an analogous Cu,Zn,Al catalyst. Furthermore, Venugopal et al.[108] reported about quaternary Cu,Zn,Al,Ga catalysts obtained from LDH for the application in dimethyl ether synthesis.

6.3.1 Choice of precipitation pH

As done for Cr (Chap. 6.2.1) the precipitation pH for Ga containing solutions was determined by titration at 25 °C. Figure 6.16 represents the titration curves of a Zn,Ga and a Cu,Zn,Al,Ga solution containing 15 % Ga. Based on the knowledge gained for the Cu,Zn,Al system in Chapter 4.1, the data in Figure 6.16 show that Ga is precipitating around pH 5, showing a similar olation behavior like Al until pH 4.

Accordingly, the Ga containing samples were also precipitated at pH 8. Thus, all resulting samples can easily be compared to CZA and Cr*X*.
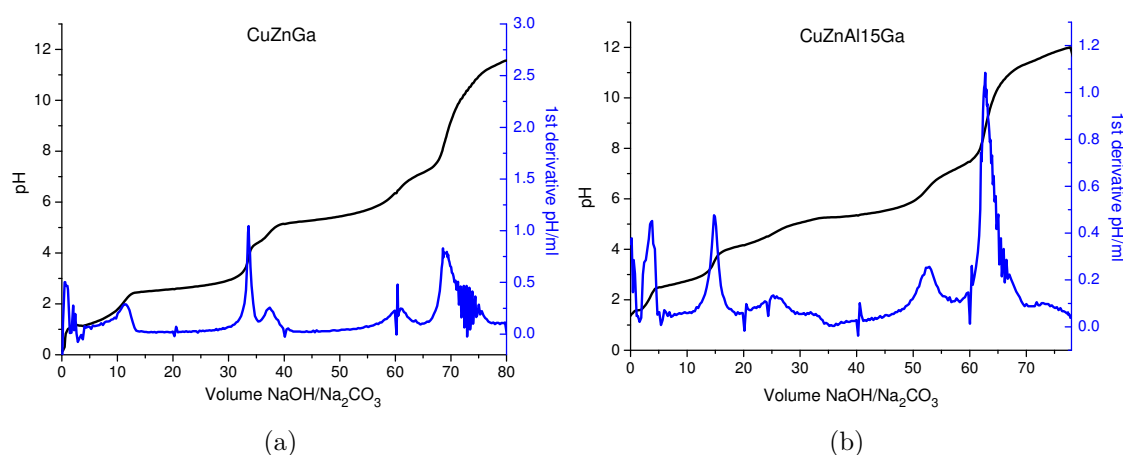
Figure 6.16: Titration curves of (a) mixed Cu,Zn,Ga solution and (b) mixed Cu,Zn,Al,Ga solution containing 15 at% Ga titrated with $NaOH/Na_2CO_3$.

6.3.2 Microstructure of Ga containing LDH precursor and calcined samples

Similar to the Cr series (Chap. 6.2.2) seven Ga containing samples were prepared. Again the overall composition was $Cu : Zn : (Al+Ga) = 50 : 17 : 33$ and Al was substituted in 5% steps. The resulting precursor samples are labeled GaX, where X is the Ga content in at%. The XRF results (calcined samples measured, for details see Chap. 3.5) in Table 6.5 show that their composition is slightly fluctuating, but that especially the Ga content is in good agreement with the nominal one used for the preparation of the starting solutions.

Table 6.5: Metal contents determined by XRF of Ga containing calcined samples, deviances for Cu ± 0.08 and for Zn ± 0.04 for all samples.

	Cu	Zn	Al	Ga	Ga nom
CZA	50.6	15.9	33.5 ± 0.37	0	0
Ga5	49.3	15.3	30.6 ± 0.31	4.8 ± 0.01	5
Ga10	51.3	16.25	22.3 ± 0.28	10.15 ± 0.02	10
Ga15	50.9	16.3	17.4 ± 0.26	15.4 ± 0.02	15
Ga20	51.3	16.3	12.4 ± 0.23	19.9 ± 0.02	20
Ga25	51.65	15.7	7.3 ± 0.18	25.35 ± 0.02	25
Ga30	51.8	16.4	2.4 ± 0.12	29.4 ± 0.02	30
Ga33	51.3	16.55	0	32.15 ± 0.02	33

The structural investigation by XRD, presented in Fig. 6.17(a) indicates a hydrotalcite structure for all samples, where with increasing Ga content the crystallinity is increasing as well. As Ga^{3+} $(0.62\,\text{Å})$ is larger than Al^{3+} $(0.535\,\text{Å})$ [102] an increased M–M distance within the layers is expected by incorporation of Ga into the hydrotalcite lattice. The analysis of the peak position of the (110) reflection, presented in Figure 6.17(b), shows an increased d-spacing for increasing Ga content. As this lattice plane is perpendicular to the brucite layers, this result proves an incorporation of Ga into the LDH structure.

The adsorption behavior of the samples was investigated by N_2 physisorption. In comparison to CZA there are just small changes, as all isotherms are type IV (Fig. 4.7(a)) with type H1 hysteresis which is getting narrower with increasing Ga content, indicating less mesoporosity.
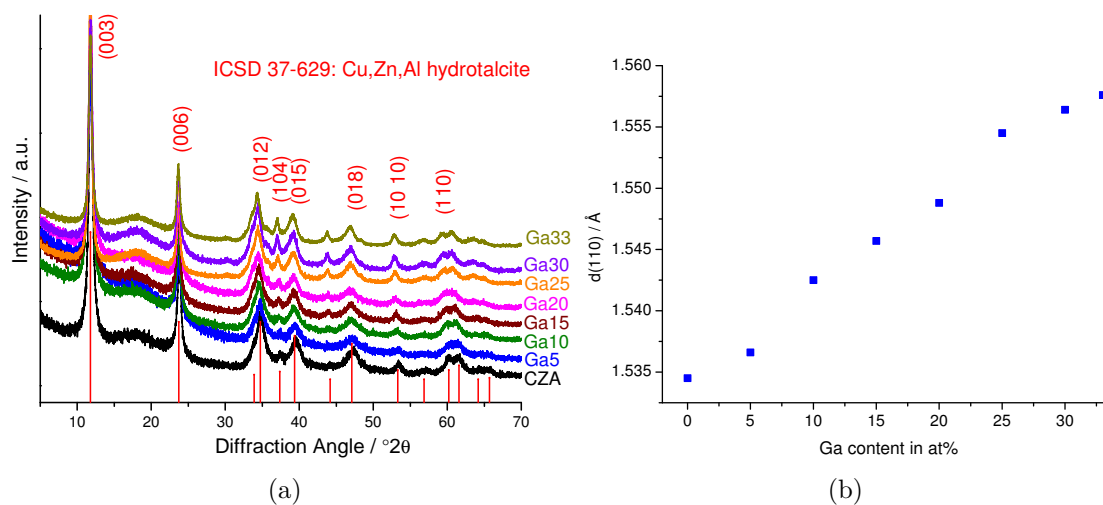
Figure 6.17: XRD of Ga series: (a) patterns in comparison to each other and to the LDH structure, (b) peak analysis of (110) – indicating an increasing M–M distance.

Furthermore, the BET surface area was determined from these adsorption curves. As shown in Figure 6.18 the surface area is decreasing with increasing Ga content with a local minimum for Ga20.
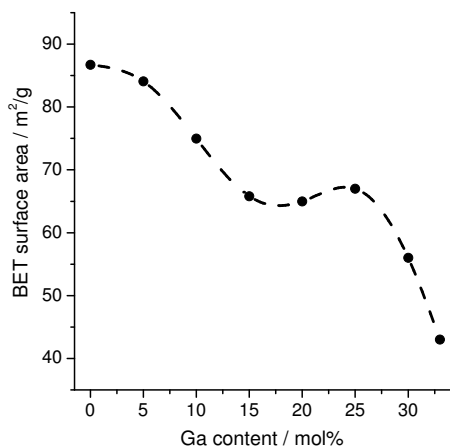
Figure 6.18: BET surface area in dependence of Ga content.

By SEM the platelet-like morphology, which is typical for LDH compounds, was also found for Ga substituted LDH, exemplarily shown for Ga5, Ga15, Ga25 and Ga33 in Figure 6.20. The increasing particle size with increasing Ga content is clearly visible in the images. This is in agreement with the observed decreasing
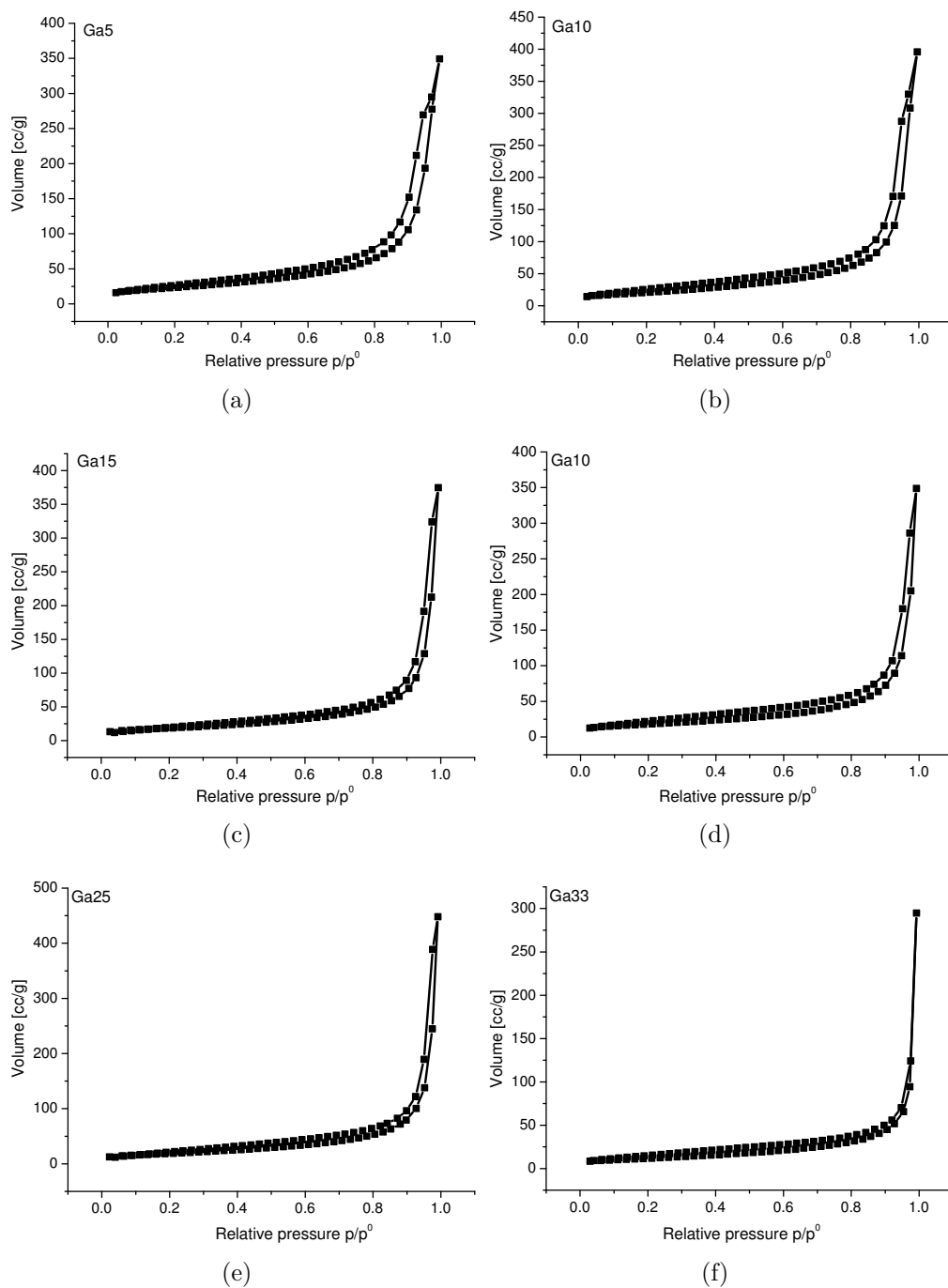
Figure 6.19: N$_2$ adsorption-desorption isotherms of Ga substituted LDH samples measured at -196 °C: (a) 5 at% Ga, (b) 10 at% Ga, (c) 15 at% Ga, (d) 20 at% Ga, (e) 25 at% Ga, (f) 33 at% Ga.
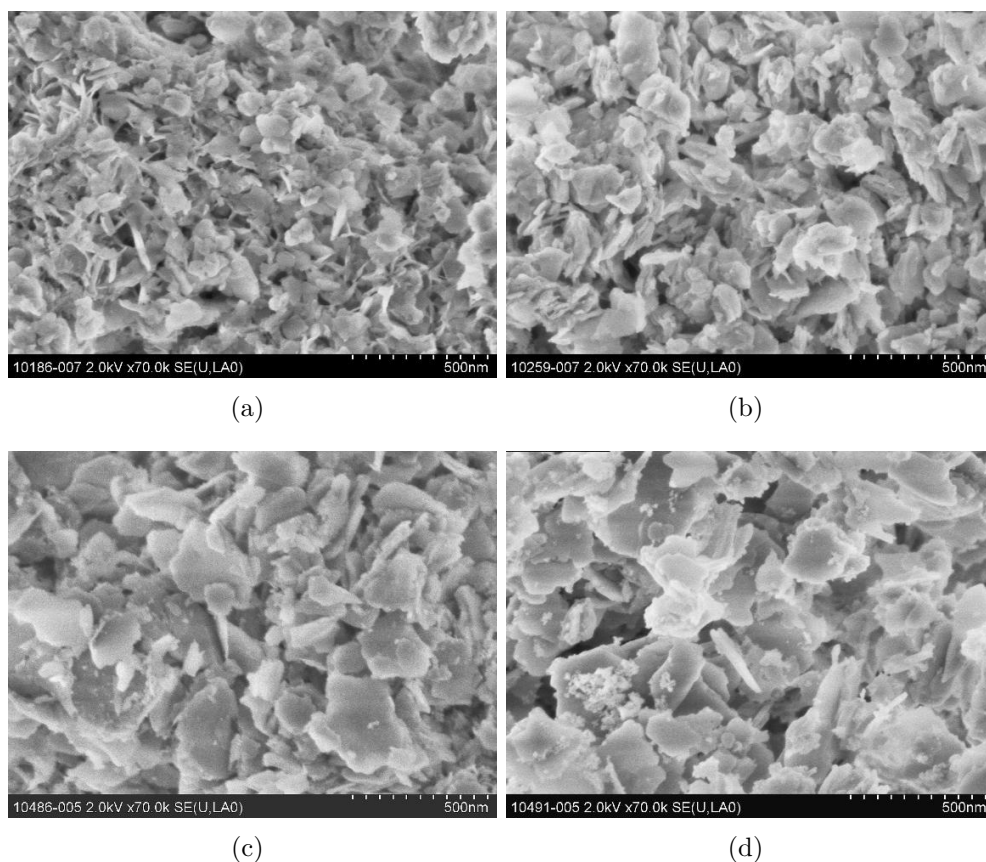
Figure 6.20: SEM images of Ga containing LDH samples: (a) 5 at% Ga, (b) 15 at% Ga, (c) 25 at% Ga, (d) 33 at% Ga.

Table 6.6: Average particle sizes (PS) determined from SEM images (>150 platelets measured); range of PSD: max - min particle size.

	CZA	Ga5	Ga15	Ga25	Ga33
PS / nm	65	61	70	82	99
range of PSD	91	78	83	135	133

BET surface area and the increasing crystallinity observed by XRD. The measured values are presented in Table 6.6. Similar to CZA the elemental distribution of Ga containing LDH is homogeneous throughout the sample series (see Figure A.18 in Appendix A.5).

As observed for CZA, the TG-MS curves of the Ga containing samples, as exemplarly shown for Ga15 and Ga33 in Figure 6.21 (for X = 5, 10, 20, 25 see
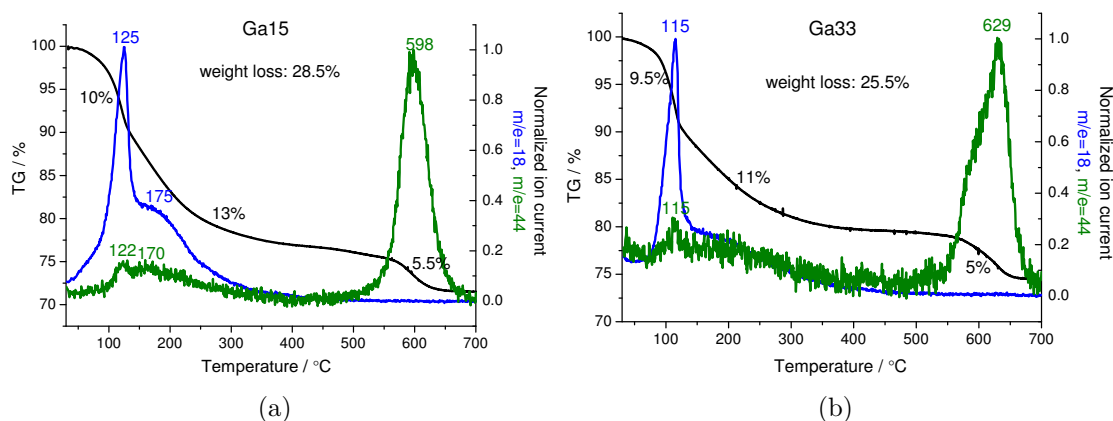
Figure 6.21: Weight loss and MS traces (blue = H_2O and green = CO_2) of Ga substituted LDH compounds during heat treatment: (a) $15\,at\%$ Ga, (b) $33\,at\%$ Ga.

Appendix A.5 Fig. A.17) are dominated by the decomposition of the hydrotalcite structure besides the decomposition of the HT-CO_3^{2-}, whose weight loss is constant with $5-5.5\,\%$. The overall weight loss is decreasing with increasing Ga content, which is in agreement with the higher theoretical weight loss due to the substitution of Al with the heavier homologue Ga. In contrast to the observation of the Cr series (Fig. 6.4(b) in Chap. 6.2.2), the decomposition temperature of HT-CO_3^{2-} (Fig. 6.22) is first decreasing (for Ga5), staying nearly constant for $5-20\,at\%$ Ga and increasing again for higher Ga contents. But in general, the deviance is much smaller than within the Cr series. This decomposition temperature was described to
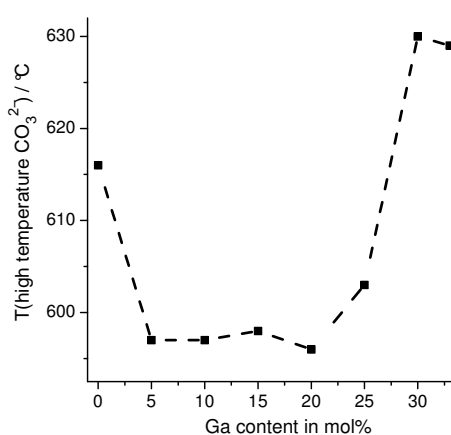
Figure 6.22: Decomposition temperature of HT-CO_3^{2-} in dependence of Ga content.

correlate with the strength of interaction contact of Cu^{2+} with the Zn-X matrix [31]. Accordingly, Al and Ga are quite similar, but substitution results in slightly smaller interface interaction for the quaternary samples. Furthermore, the TG-MS show that the temperature of $330\,^{\circ}C$, used for the calcination of CZA and Cr*X* (to obtain CZA-calc and Cr*X*-calc), is also applicable for this sample series, as in all cases the dehydroxylation and decarboxylation is finished at this temperature. Similar to Cr*X*-calc, the calcined Ga containing samples will be labeled as Ga*X*-calc in the following.

CZA-calc (Chap. 4.2.2) as well as Cr*X*-calc (Chap. 6.2.2) were shown to be amorphous, carbonate-modified mixed oxides. As shown in Figure 6.23 this is also valid for Ga*X*-calc with $\leq 15\,at\%$ Ga, which contain $6-7\,wt\%$ HT-CO_3^{2-} (calculated from TG-MS curves). For higher Ga contents the formation of $ZnGa_2O_4$ spinel
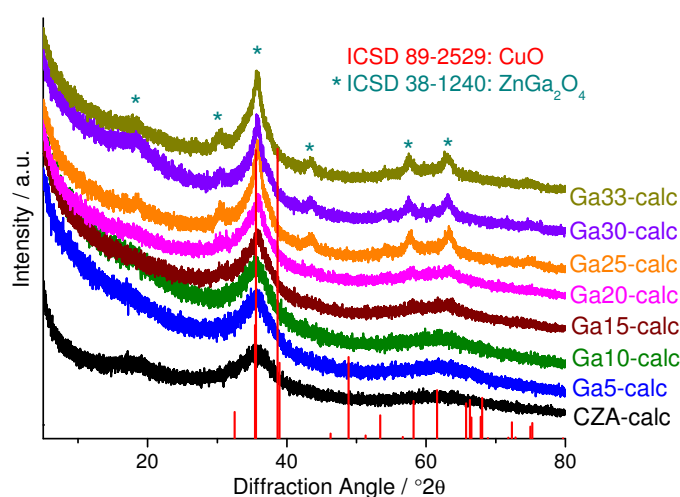
Figure 6.23: XRD patterns of Ga samples after calcination at $330\,^{\circ}C$.

was observed, which is coinciding with an increasing decompostition temperature of HT-CO_3^{2-} (compare Fig. 6.22). In case of CZA the spinel formation occured more or less simultaneously with the decomposition of HT-CO_3^{2-} above $600\,^{\circ}C$. The lower crystallisation temperature of Ga*X*-calc ($X \geq 20$), especially of the spinel, indicates a phase separation during calcination at $330\,^{\circ}C$, which was not observed for CZA-calc. Thus, this sample series can be understood as two groups of samples – $X < 20$ and $X \geq 20$, which is in agreement with the BET surface area evolution as well as the decomposition temperature of HT-CO_3^{2-}.

Analogous to the Cr series, after calcination at 700 °C the quaternary samples of the Ga series, as exemplarily shown for Ga15 (Fig. 6.24), are composed of mixed $Zn(Al,Ga)_2O_4$ spinel. Therefore, the local environment of the GaX-calc ($X \leq 15$) can be described in analogy to CZA-calc (Chap. 4.2.2) as well dispersed CuO within the $Zn(Al,Ga)_2O_4$ spinel-like matrix.
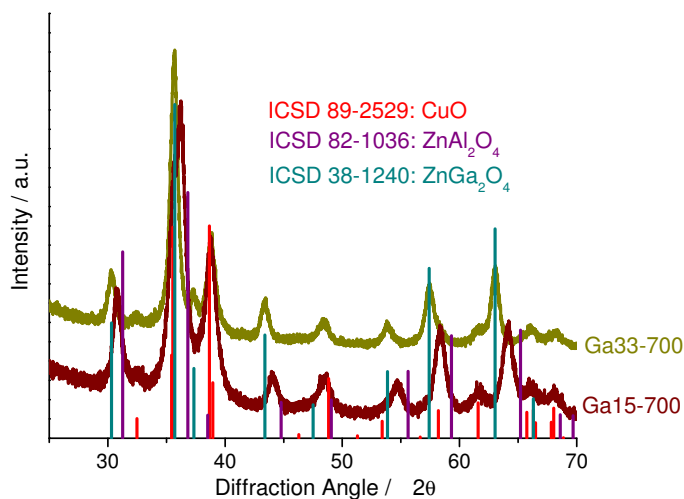
Figure 6.24: XRD pattern of Ga15-700 and Ga33-700, samples after calcination at 700 °C.

Furthermore, by SEM it was shown that there are no significant changes of the morphology of the calcined samples compared to the LDH ones, exemplarily depicted in Figure 6.25 for Ga20-calc and Ga33-calc. Additionally, the trend of the BET

(a)   (b)
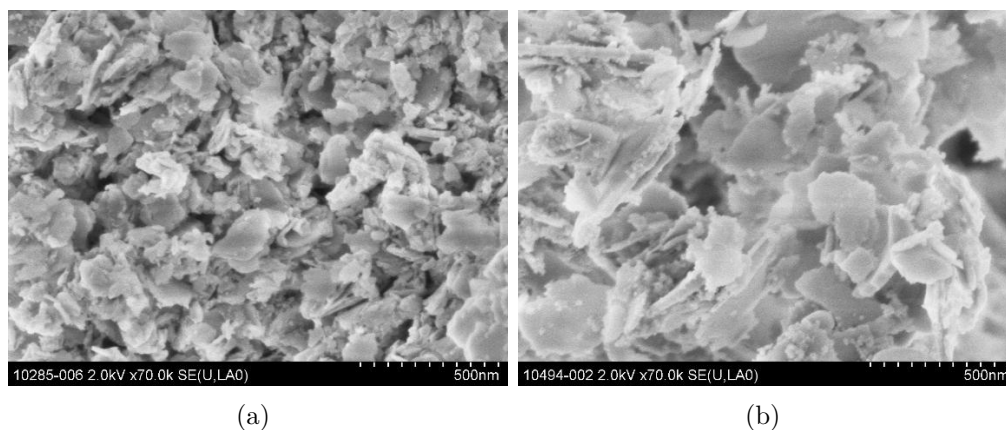
Figure 6.25: SEM images of calcined samples: (a) Ga20-calc, (b) Ga33-calc.

surface area is quite similar to the precursor samples, a decreasing surface area is obtained for increasing Ga contents (Fig. 6.26) with a local minimum for Ga15-calc.
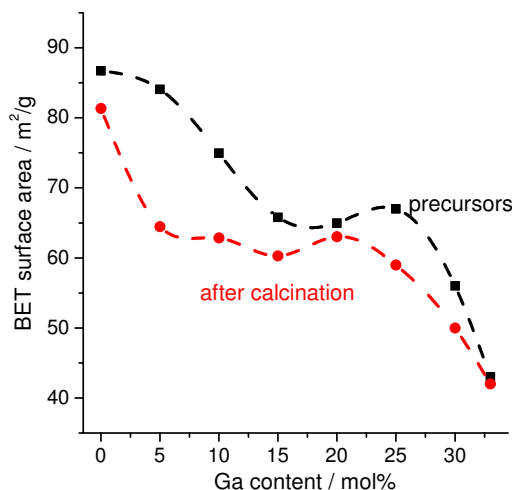
Figure 6.26: BET surface area in dependence of the Ga content for samples after calcination at 330 °C in comparison to precursor samples.

6.3.3 Investigation of reduction behavior and microstructure of resulting catalysts of Ga containing ternary and quaternary samples

The investigation of the reduction behavior of Ga*X*-calc samples is based on the knowledge gained from the reduction of CZA-calc (Chap. 4.3). As shown in Figure 6.27 the TPR profiles gradually change with the insertion of Ga. First of all, for low and high Ga content a decreased T_{max} is observed compared to CZA-calc, whereas for Ga : Al around 1 : 1 (Ga15-calc and Ga20-calc) a higher reduction temperature was found (see Tab. 6.7). The observed changes of T_{max} are much smaller compared to the Cr-substituted sample series (Chap. 6.2.3). The experimental hydrogen consumption is in agreement (Tab. 6.7) with the amount of CuO present in the samples (values from XRF Tab. 6.5), hence a direct participation of gallium oxide in the redox reaction, as observed for chromium oxide, (Chap. 6.2.3) can be excluded. Accordingly, all observed changes are due to CuO and its interaction with the Zn-(Al,Ga) matrix.

The apparent activation energies of the reduction were determined for Ga*X*-calc (with $X = 5, 15, 25, 33$) as described in Chapter 2.2 and as done for CZA-calc in
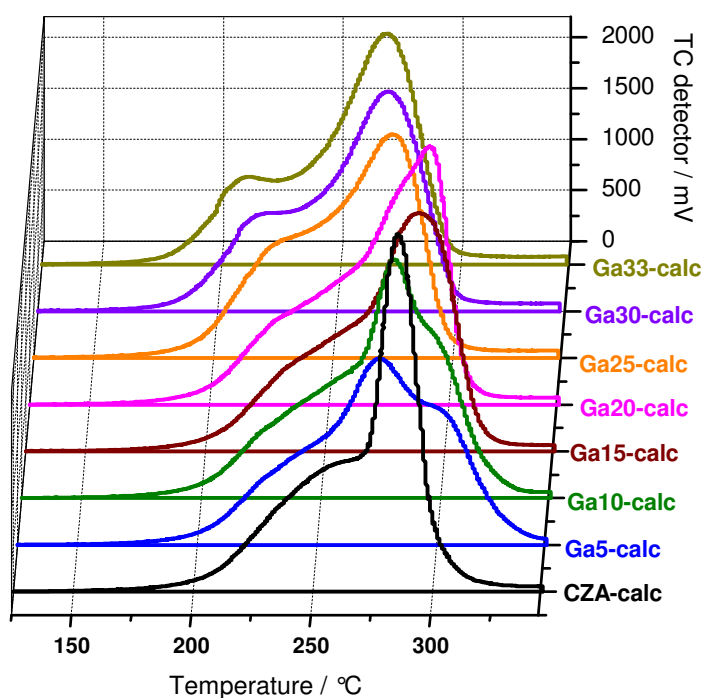
Figure 6.27: TPR profiles of Ga*X*-calc samples (parameters set to $K = 105 - 109\,s$, $P = 10.5 - 10.9\,K$).

Chapter 4.3. The results are given in Table 6.8. A lower value is observed by the introduction of Ga into the catalyst. But nevertheless from the range of the activation energies as well as the similarity of these catalysts with CZA-calc a CuO-like identity

Table 6.7: TPR of Ga series: T_{max} and ratio of reduced CuO determined from hydrogen consumption.

at% Ga	T_{max} / °C	CuO_{red} / %
0	285	98
5	276	98
10	280	96
15	293	99
20	292	99
25	275	98
30	271	97
33	265	96

of the Cu oxide phase within the $Zn(Al,Ga)_2O_4$ matrix can be assumed. Based on the characterization of GaX-calc, the sample series is devided in two groups to analyze the reduction behavior.

As described in Chapter 4.3 for CZA-calc a higher reduction temperature (compared to the conventionally prepared catalyst system) is caused by the controlled separation of reducible and irreducible phases due to homogeneous elemental distribution and the strong interaction of "CuO" with the Zn-Al matrix, which has to be overcome before reduction. This interaction is assumed to be related to the presence of HT-CO_3^{2-} in the calcined sample. Based on the decomposition temperature of HT-CO_3^{2-} (see Fig. 6.22) it was shown that the interaction is slightly weaker for the first group of samples ($5-15\,at\%$ Ga), explaining the lower T_{max} of Ga5-calc. The increasing reduction temperature within this group, is probably due to a particle size effect implemented by the LDH precursor, similar as observed for the Cu,Zn,Al catalyst obtained by ME technique (see Chap. 5). All four samples have approximately the same decomposition temperature of HT-CO_3^{2-} but an increasing particle size was observed by SEM of the precursor samples (Tab. 6.6). Furthermore, the TPR profile of Ga5-calc and Ga10-calc show, additional to the well described shoulder on the low temperature side (see Chap. 4.3), a shoulder on the high temperature side. This is also illustrated within the qualitative peak deconvolution for Ga5-calc in Figure 6.28 which is based on the two-step reduction mechanism of CuO, which was shown for CZA-calc (Chap. 4.3). As this shoulder is not influenced when different heating rates are applied (Fig. A.19 in Appendix A.5), it can be excluded that this effect is caused
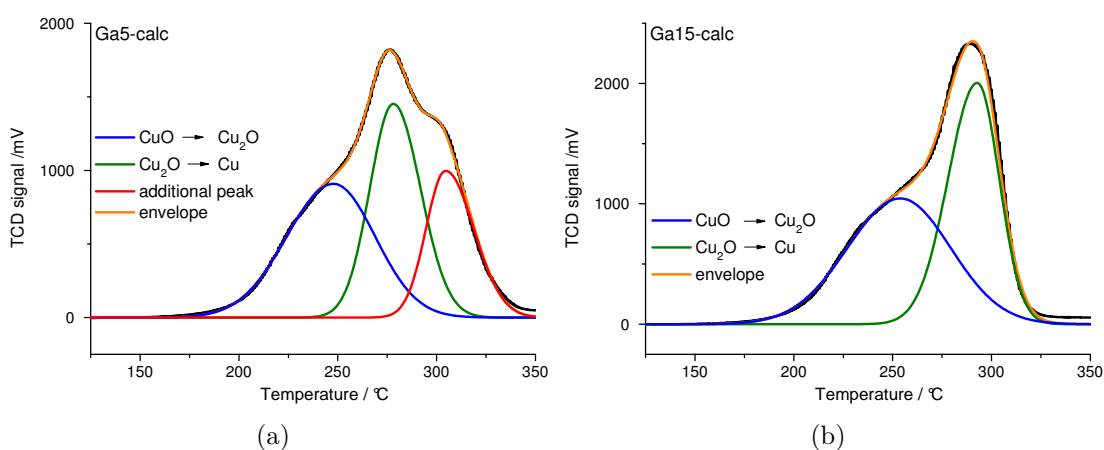
Figure 6.28: Peak deconvolution of TPR profiles: (a) Ga5-calc, (b) Ga15-calc.

by regions with different particle sizes. Accordingly, the only explanation for this observation is that these samples contain two slightly different Cu species due to the modifications in the oxidic matrix by substitution of Al by Ga which is changing the interaction of the Cu phase and the Zn-(Al,Ga) matrix.

On the other hand, the second group of the sample series $(20 - 33\,\text{at\%}\ \text{Ga})$ is characterized by a lower reduction temperature than observed for the first group and CZA-calc which is decreasing with increasing Ga content. Furthermore, the TPR profile of Ga33-calc contains an additional peak around $210\,^\circ\text{C}$, which is also supposed to be present for Ga20-calc, Ga25-calc and Ga30-calc, indicating the presence of two different "CuO" species. This is also supported by the qualitative peak deconvolution, presented in Figure 6.29, which is based on the two-step reduction mechanism of CuO, which was shown for CZA-calc (Chap. 4.3). Based on the knowledge gained
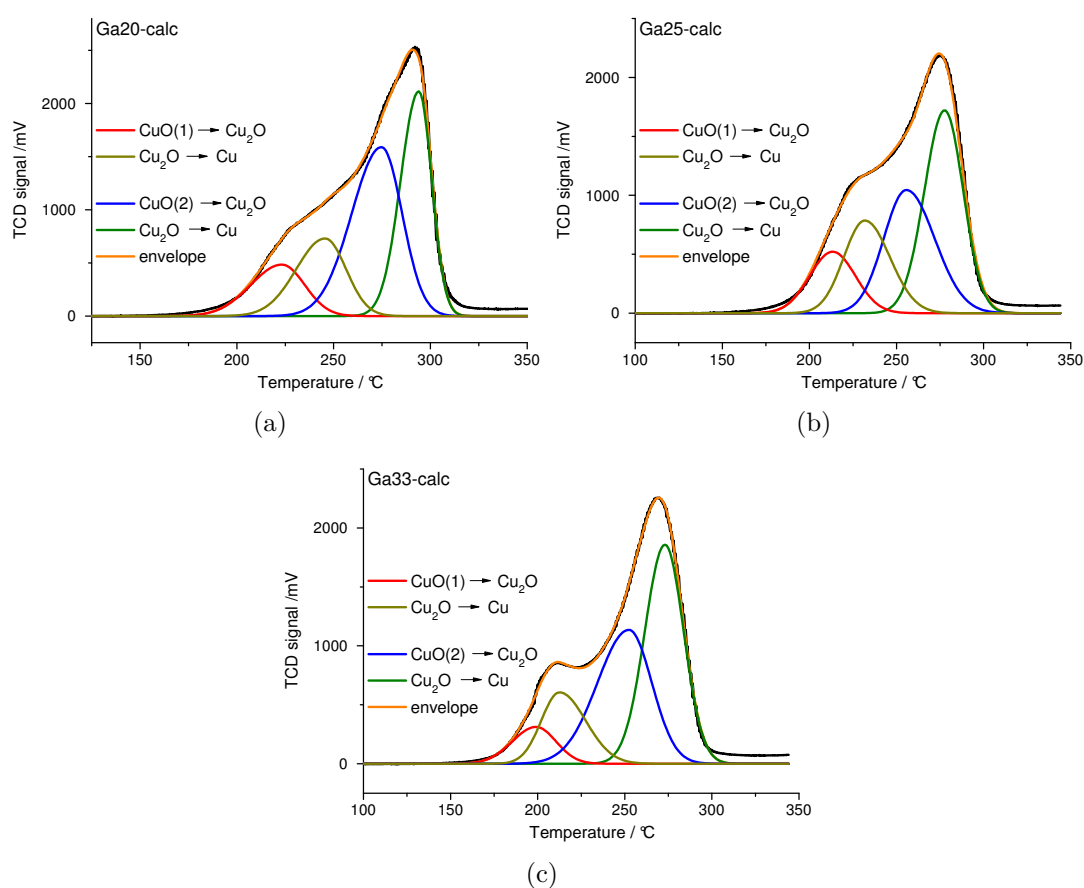
Figure 6.29: Peak deconvolution of TPR profiles: (a) Ga20-calc, (b) Ga25-calc, (c) Ga33-calc.

from XRD of the calcined samples (Fig. 6.23), the peak at lower temperatures is assigned to the weaker interaction of Cu^{2+} with the crystalline $ZnGa_2O_4$ spinel, which is partially formed after calcination (compare red and purple curve in Fig. 6.23). The high temperature peak is attributed to the stronger interaction of Cu^{2+} with the amorphous Zn-(Al,Ga) matrix (compare blue and green curve in Fig. 6.23), as similar observed for CZA-calc. Furthermore, the whole reduction process is occurring at slightly lower temperatures than for CZA-calc, which is probably caused by the partial phase separation during calcination of these samples, seen by the formation of $ZnGa_2O_4$ besides the amorphous matrix.

Similar to CZA-red, the Ga containing catalysts resulting after reduction of GaX-calc is labeled as GaX-red. The Cu surface area of GaX-red (X = 5, 15, 25, 33) was determined by N_2O-RFC (Tab. 6.8), where no influence was observed with substitution of Al by Ga. The TEM investigation, exemplary done for Ga15-red and Ga33-red, showed in agreement to the Cu surface area nearly no inluences on the Cu particle size with increasing Ga content (see Tab. 6.8 and PSD in Fig. A.20 in Appendix A.5). The TEM images, depicted in Figure 6.30, illustrate, once more,

Table 6.8: Activation energy of reduction and properties of resulting catalysts: HT-CO_3^{2-} content is determined from TG-DSC curves, N_2O-RFC and TEM particle size evaluation; interface ratio (IFR) is calculated from theoretic Cu surface area based on TEM particle size.

at% Ga	E_A /kJ/mol	Cu-SA /m^2/g	HT-CO_3^{2-} /wt%	Cu PS /nm	IFR /%
0	60 ± 3	7.4 ± 0.7	4.8	7.0	85
5	58 ± 5	7.0 ± 0.7	1.6	n.m.	n.m.
15	50 ± 4	7.2 ± 0.7	2.7	8.5	81
25	46 ± 2	7.6 ± 0.8	1.4	n.m.	n.m.
33	50 ± 2	7.9 ± 0.8	2.1	8.6	76

the similarity of all catalysts resulting from LDH as the Cu particles of the Ga containing catalysts are also embedded within an oxidic matrix. For Ga contents ≤ 15 at% this mixed oxide is mostly amorphous (compare also XRD in Fig. 6.23) similar to CZA-red. For higher Ga contents in agreement with the observations of the calcined samples also crystalline $ZnGa_2O_4$ spinell was found (see TEM image of Ga33-red in Fig. A.20(c) in Appendix A.5). In Chapter 4.4 the "stability" of this microstructure to air was shown for the final catalyst obtained from LDH precursor.

<div align="center">(a)   (b)</div>
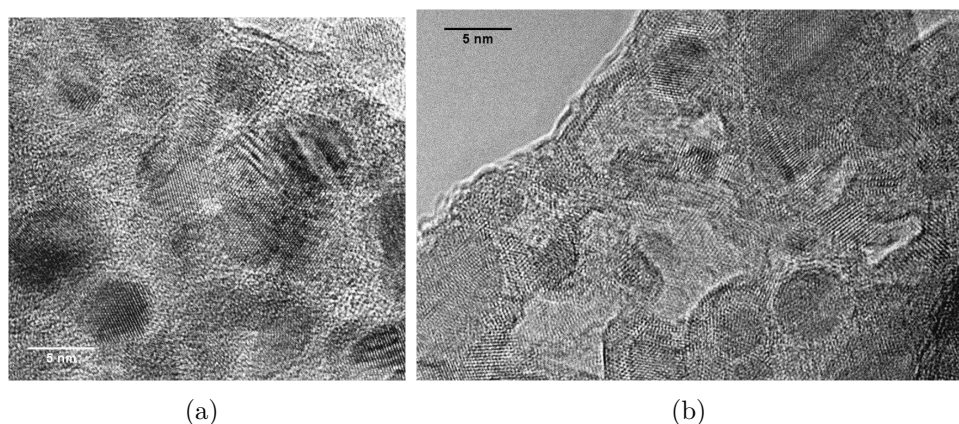
Figure 6.30: TEM images of Ga containing catalysts: (a) Ga15-red, (b) Ga33-red; highly embedded Cu^0-particles (dark spots) in oxidic matrix.

For Ga containing catalysts, this "stability" is maintained after reduction (compare Fig. A.21 in Appendix A.5).

Furthermore, all catalysts were investigated for their catalytic activity in methanol synthesis, the results are presented in Figure 6.31(a). Again, the catalytic activity

<div align="center">(a)   (b)</div>
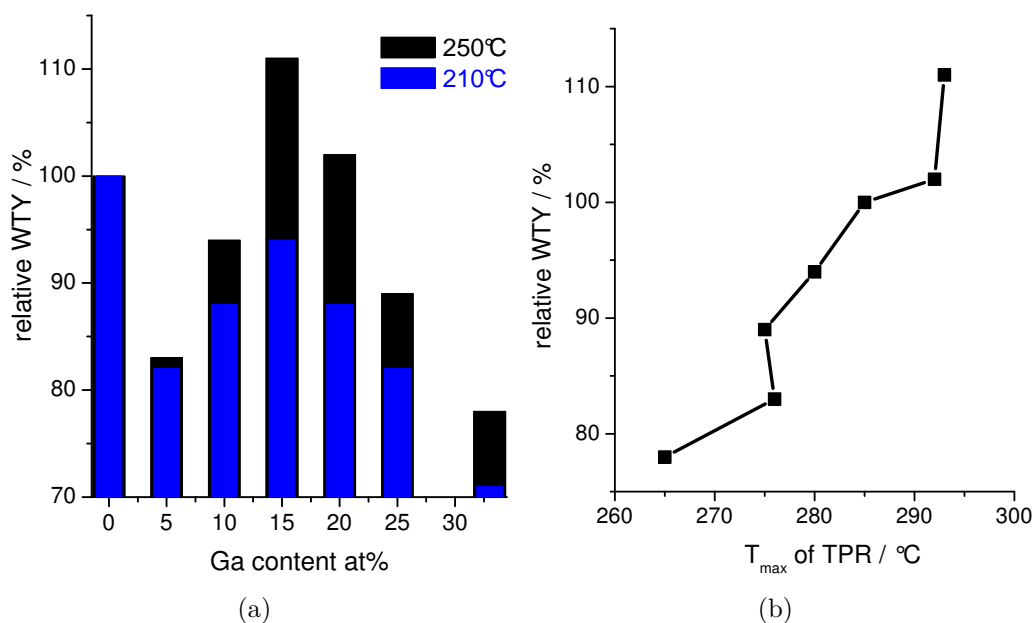
Figure 6.31: Comparison of catalytic activity in methanol synthesis (average WTY): (a) in dependence of the Ga content, normalized to the CZA catalyst, (b) in dependence of T_{max} of reduction of calcined samples.

does not scale with the Cu surface area, which is nearly constant for all samples. The lowest activity, both for 250 °C as well as 210 °C reaction temperature, was found for 33 at% Ga, whereas the highest activity at 250 °C was observed for 15 and 20 at% Ga, where the Al : Ga ratio is around 1 : 1. In other studies it was shown, that the lower the reduction temperature during catalyst activation the higher is the activity of the derived catalyst [74, 107]. Within this study a more or less inverse trend was observed: the higher T_{max} the higher is the activity in methanol synthesis (Fig. 6.31(b)). Additionally, the maximum in activity at 250 °C is coinciding with a low decomposition temperature of HT-CO_3^{2-}. This result show that a ternary oxide can improve the intrinsic activity, if the microstructure of the resulting catalyst is not influenced. On the other hand, the low activity of high Ga contents indicates that partially crystalline oxide, which is already present in the calcined state, yield a lower intrinsic activity, despite the Cu phase is nearly identically to the CZA catalyst system.

To complete this study TPR-TPO cyclization experiments were carried out for GaX-calc with $X = 5, 15, 25, 33$ (see Fig. 6.32), as presented for CZA-calc in Chapter 4.4. The obtained results (summarized in Table A.4 in Appendix A.5) show again the similarity of the obtained Ga containing catalysts and the CZA catalyst after the first reduction (TPR1), as the shape of the profile as well as T_{max} of the rereduction (TPR2) are nearly identical. The smaller hydrogen consumption of TPR2 can be attributed to an incomplete oxidation during the TPO treatment, as was shown for the CZA catalyst (Chap. 4.4). In contrast to the latter, the Cu surface area of the Cu,Zn,Ga catalyst (Al free) was not doubled, but decreased (5 m²/g) upon this redox process, which is attributed to thermal sintering. Accordingly, the positive effect of reoxidation, observed for the CZA catalyst system (Chap. 4.4), was not effective, probably due to the partial phase separation which already occurred during calcination.

6.3.4 Conclusion

The stepwise substitution of Al by Ga, indeed results in quaternary LDH. The incorporation of Ga into the LDH structure was proven by XRD and the average platelet size was increasing significantly with increasing Ga content. After decomposition in air carbonate-modified mixed oxides were obtained for Ga contents ≤ 15 at%,
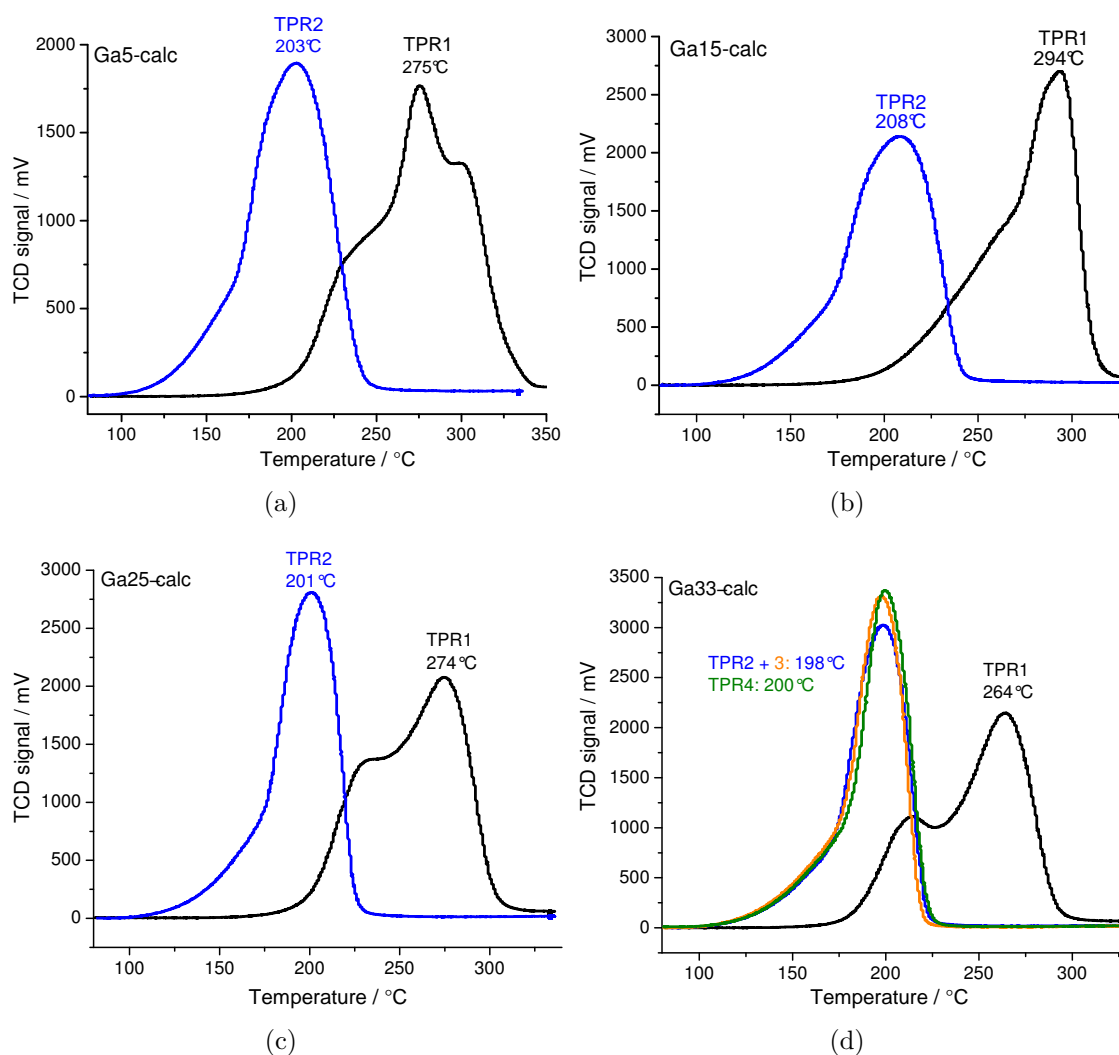
Figure 6.32: TPR profiles of TPR-TPO-TPR experiment: (a) Ga5-calc, (b) Ga15-calc, (c) Ga25-calc, (d) Ga33-calc ($K = 105 - 109\,s$, $P = 10.5 - 10.9\,K$).

like described for CZA-calc. Higher Ga contents led to the formation of crystalline $Zn(Al,Ga)_2O_4$ or $ZnGa_2O_4$ spinel. Similar to the reduction of CZA-calc (Chap. 4.4), the reduction of GaX-calc with $X \leq 15\,at\%$ led to Cu particles embedded within a non-crystalline $Zn(Al,Ga)_2O_4$ spinel-like matrix. For higher Ga contents the Cu particles are still highly embedded, but the oxidic matrix is also composed of crystalline $ZnGa_2O_4$ spinel. The reduction profiles themselves were gradually changed by the insertion of Ga into the catalyst system. In particular, for high Ga contents two different Cu species were found. This is attributed to the presence of partially

crystalline spinel and the resulting different strength of interface interaction of the CuO phase with the crystalline and the amorphous oxide. But nevertheless, the reduction yields Cu based catalysts with similar Cu particle size as well as Cu surface area and interface ratio for all catalysts.

However, as observed for the Cr containing catalysts, the catalytic activity in methanol synthesis does not scale with the Cu surface area as a maximum was observed for $Ga : Al \approx 1 : 1$. Thus, a ternary oxide can improve the intrinsic activity, if the microstructure of the resulting catalyst is not influenced. On the other hand, the low activity of high Ga contents ($\geq 20 \, at\%$) indicates that an early phase separation (during calcination) and a partially crystalline oxide yield a lower intrinsic activity, indicating a less effective interaction of Cu with the oxide matrix. In general, during the evaluation of the presented data the question occured as a reasearch perspective, if the maximum activity of this system is already found. To answer this question, more Ga containing samples need to be prepared with smaller steps of the Al substitution between 10 and $15 \, at\%$ Ga.

Similar to the CZA catalyst TPR-TPO cyclization experiments revealed that the first reduction procedure is an irreversible process. The shape of the profile as well as T_{max} of the rereduction (TPR2) of Ga containing catalysts and the CZA catalyst are nearly identical, indicating a high the similarity of the systems. Probably due to the partial phase separation, which already occurred during calcination, the reoxidation treatment of the Cu,Zn,Ga catalyst is less effective compared to the Cu,Zn,Al catalyst, whose Cu surface area was doubled upon a redox process.

After all, this sample series shows that it is possible to prepare a series of Cu based catalysts with the same preparation history, which are characterized by a homogeneous elemental distribution and a nearly identical microstructure (Cu surface area, Cu particles size, embedment) but significant differences in catalytic performance attributed to differences in intrinsic activity.

7 Final Discussion

As described in Chapter 4 a phase pure Cu,Zn,Al LDH was prepared by co-precipitation, resulting in the composition $(Cu_{0.5}Zn_{0.17})Al_{0.33}(OH)_2(CO_3)_{0.17} \cdot m\,H_2O$, which is showing the typical platelet-like morphology and homogeneous distribution of all three metal cations. Upon decomposition in air a carbonate-modified mixed oxide was formed, without any crystal lattice found by XRD or TEM. The local environment around Cu^{2+} and Zn^{2+} in this homogeneous, amorphous oxide was similar to CuO and $ZnAl_2O_4$ as shown by NEXAFS respectively. Thus, the mixed oxide can be described as well dispersed CuO within $ZnAl_2O_4$ still containing $8\,wt\%$ of carbonate after calcination at $330\,°C$. This form of high temperature resistant carbonat ($HT\text{-}CO_3^{2-}$) is assumed to stabilize the homogeneous mixed oxide and to maintain the homogeneous elemental distribution. A strong interaction of Cu^{2+} ions with the Zn-Al matrix via O^{2-} bridges, as similarly described in [74] has been observed and were shown to be generally characteristic of ex-LDH $Cu/ZnAl_2O_4$ catalysts. These interactions are responsible for a hindered reduction, a strong embedment, a small Cu surface area and a high intrinsic activity of the Cu particles.

The reduction of the Cu species in CZA-calc itself follows the same two-step mechanism as expected for CuO and as observed in other Cu/ZnO based catalysts [81]. In combination with the homogeneous distribution of Cu the special interaction in the Cu,Zn,Al ex-LDH material makes the reduction more difficult and causes a shift to higher temperature (compared to a conventionally prepared reference catalyst) as well as a pronounced stability of the Cu(I) intermediate, which was clearly identified by NEXAFS measurements. The temperature shift is attributed to the strong contact which has to be overcome before reduction. Upon heating, the well dispersed Cu^{2+} cations separate from the Zn-Al-oxide matrix, form clusters and finally start to reduce. Besides, by evaluation of multiple heating rate TPR measurements it was possible to calculate the phase evolution, assuming that the pronounced shoulder of the TPR profile is representing the presence of Cu_2O. This prediction, which represents the

bulk behavior, is in good agreement with the measured phase evolution near the surface (NEXAFS). In conclusion, the reduction of $CuO/ZnAl_2O_4$ resulting from LDH can be described as separation of reducible and irreducible phases. Therefore, in this catalyst system the nanostructuring by phase separation and segregation takes place during reduction and not during calcination as observed for the conventionally prepared catalyst.

The resulting Cu based catalyst can be described as Cu dispersed in a $ZnAl_2O_4$ spinel-like matrix. The Cu particles measure just 7 nm despite the high loading of 50 at%. Due to the high embedment it exhibits only a small absolute activity in methanol synthesis compared to the conventionally prepared reference catalyst but a high intrinsic one (relative to the Cu surface area). This shows the great importance of the interface contact of Cu and its surrounding. Furthermore, this catalyst was shown to be oxidation stable under air contact.

By TPR-TPO cyclization experiments it was shown that the nanostructuring upon reduction of the well dispersed, amorphous CuO (TPR1) is an irreversible process. During reoxidation the embedment is partially destroyed by a sintering effect leading to crystalline copper oxide particles also observed by XRD. After all, the described strong interaction of CuO and $ZnAl_2O_4$ in CZA-calc was broken during reduction and not reinforced during reoxidation. Thus, the rereduction occurs at lower temperatures and the reaction of the intermediate Cu_2O to Cu is not hindered anymore. This redox process results in less embedded Cu particles. Obviously the annihilation of embedment is limited as during further cyclization of oxidation and reduction no additional changes are observed. Thus, the state resulting after the first reduction and reoxidation can be reversibly cycled.

In general, we assume that the characteristics of the LDH precursor are largely reflected in the properties of the catalyst after the initial thermal treatment (so called chemical memory) and that the complete development of the catalyst´s final microstructure is finished only after repeated TPR-TPO treatment. Thus, in case of the ex-LDH catalyst, the redox cycling can be regarded as a part of the preparation rather than a deactivating stress test as in case of the conventionally prepared catalyst.

Additionally, in Chapter 5 the possibility to apply a pH-controlled microemulsion technique to synthesize Cu,Zn,Al LDH by co-precipitation within ME-droplets has been demonstrated. The BET surface area of the ME products (precursor and

calcined one) is higher and the LDH particles are smaller than the ones of the conventionally co-precipitated reference catalyst. In agreement with the catalyst obtained by conventional co-precipitation, the catalyst obtained by microemulsion technique contains small Cu particles embedded within the oxidic matrix. The catalyst resulting from ME exhibits the higher Cu surface area, which is attributed to the smaller size of its $Cu/ZnAl_2O_4$ aggregates. However, the increase in Cu surface area does not scale with the increase in activity. The lower intrinsic activity of the catalyst resulting from microemulsion indicates that the Cu surface area is not the only influencing parameter to gain high activity.

The role of the promoting effect of Al was investigated with the substitution by Cr and Ga. First of all, the stepwise substitution of Al, presented in Chapter 6, has shown that it is possible to prepare quaternary LDH precursors for Cu based catalysts. After decomposition in air carbonate-modified mixed oxides were obtained for Cr containing samples as well as for Ga contents $\leq 15\,at\%$, similar to the $Cu/ZnAl_2O_4$. Higher Ga contents led to the formation of crystalline $Zn(Al,Ga)_2O_4$ or $ZnGa_2O_4$ spinel.

Furthermore, the substitution of Al with Cr gradually weakens the special interaction of the Cu phase with the Zn-X matrix probably due to the participation of the chromium oxide phase at the redox processes during catalyst preparation. Such reactive Cr oxide matrix is less efficient than the inert Al oxide matrix in stabilizing the special microstructure of Cu/ZnM_2O_4 catalysts. It promotes the rearrangements in the solid state and does not hinder the Cu reduction as effectively as $ZnAl_2O_4$. These weakened interactions led to a lowering of the Cu particle embedment, co-inciding with a pronounced Cu crystallite growth during reduction. Both effects partially compensate each other and a maximum in Cu surface area is observed for intermediate Cr contents. However, the catalytic activity does not scale with the Cu surface area in this series of samples, which is attributed to a difference in intrinsic activity of the exposed Cu surface. Correlations of the intrinsic activities with decreasing Cu particle size and increasing interface ratio with the oxide component could be found. These findings are in agreement with recent observations, that the intrinsic activity of Cu is related to defects and strain in the Cu particles [15, 32], which exhibit a larger concentration on small particles and are likely to be "pinned" at the metal-oxide interface [38].

By the analysis of the TPR profiles of GaX-calc two different Cu species were found for high Ga contents. This is attributed to the presence of partially crystalline spinel and the resulting different strength of interface interaction of the CuO phase with the crystalline and the amorphous oxide. As observed for the reduction of CZA-calc, the reduction of GaX-calc led to Cu based catalysts with a similar microstructure, as the average Cu particle size as well as the Cu surface area and interface ratio are quite similar for all catalysts. Furthermore like observed for CZA-red, the small Cu particles are embedded within a $Zn(Al,Ga)_2O_4$ spinel-like matrix for Ga contents $\leq 15\,at\%$. For higher Ga contents the Cu particles are still highly embedded, but the oxidic matrix is also composed of crystalline $ZnGa_2O_4$ spinel. However, their catalytic activity in methanol synthesis does not scale with the Cu surface area either but shows a maximum for intermediate Ga contents in those samples, where the Al-Ga substitution did not lead to a partial crystallization of the spinel. Thus, it was shown that a ternary oxide can improve the intrinsic activity without significant influence onto the catalyst microstructure. Furthermore, the presence of crystalline oxide has a negative influence on the Cu matrix interaction resulting in a lower intrinsic activity as observed for high Ga contents ($\geq 20\,at\%$).

After understanding the shape of the TPR profiles of the presented samples, it can be concluded that the kinetic stabilization of Cu_2O during the reduction of CZA-calc is tunable by the catalyst preparation. Hence, a new synthetic approach could be the preparation of a catalyst having a maximum amount of Cu(I) intermediate during a controlled reduction.

After all, the Al substituting sample series show that it is possible to prepare a series of Cu based catalysts with the same preparation history, which are characterized by a homogeneous elemental distribution and a similar microstructure but significant differences in catalytic performance attributed to differences in intrinsic activity. Thus, it was nicely shown, that Al as inert oxide is stabilizing the special microstructure of the Cu/ZnM_2O_4 catalysts resulting from LDH precursors. In fact, interface interactions between Cu and the oxide seem to beneficially affect the activity of the Cu particles and the optimal catalyst requires a compromise of exposed surface and interface. This investigation has shown that Cr and Ga are influencing the ex-LDH catalyst system at different points. Thus, it was found that the modification of the interface area (Cr) as well as the type of the interface interaction (Ga) are possible to control the intrinsic activity of Cu in the resulting Cu based catalyst.

A Appendix

A.1 Additional diagrams to the analysis of the CZA catalyst system

(a)   (b)
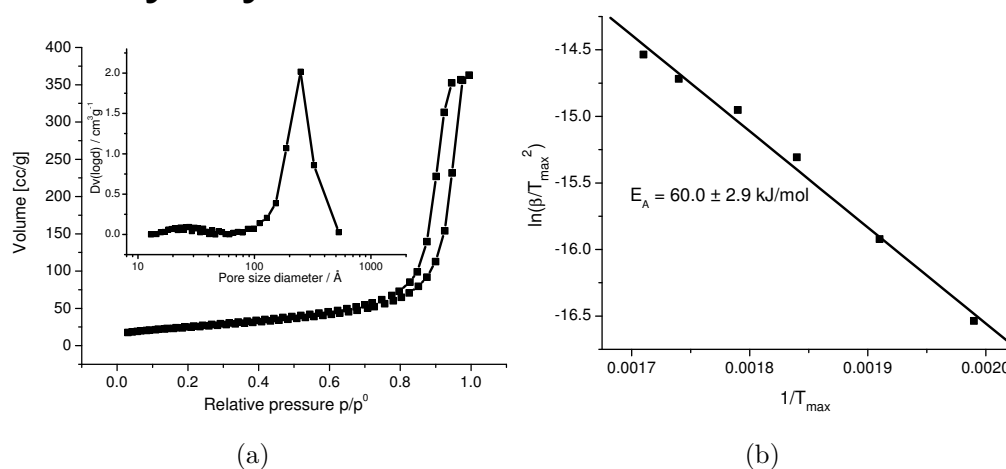
Figure A.1: (a) Nitrogen adsorption-desorption results of CZA-calc: adsorption-desorption isotherm and "pore" size distribution derived with BJH model; (b) Modified temperature programmed "Arrhenius plot" for CZA catalyst.
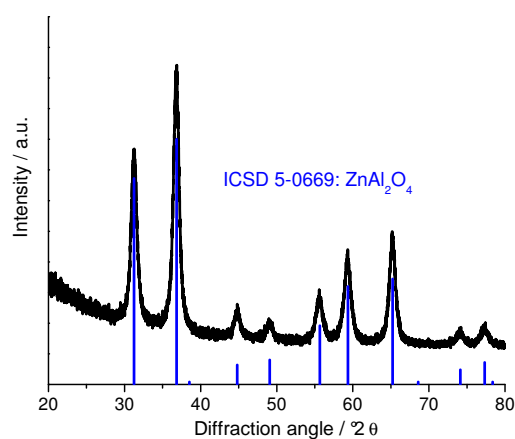
Figure A.2: XRD pattern of $ZnAl_2O_4$ reference compound: phase-pure spinel structure shown by ICSD 5-0669 [109]; for synthesis details see Chapter 3.4.

(a)

(b)

(c)

(d)

(e)
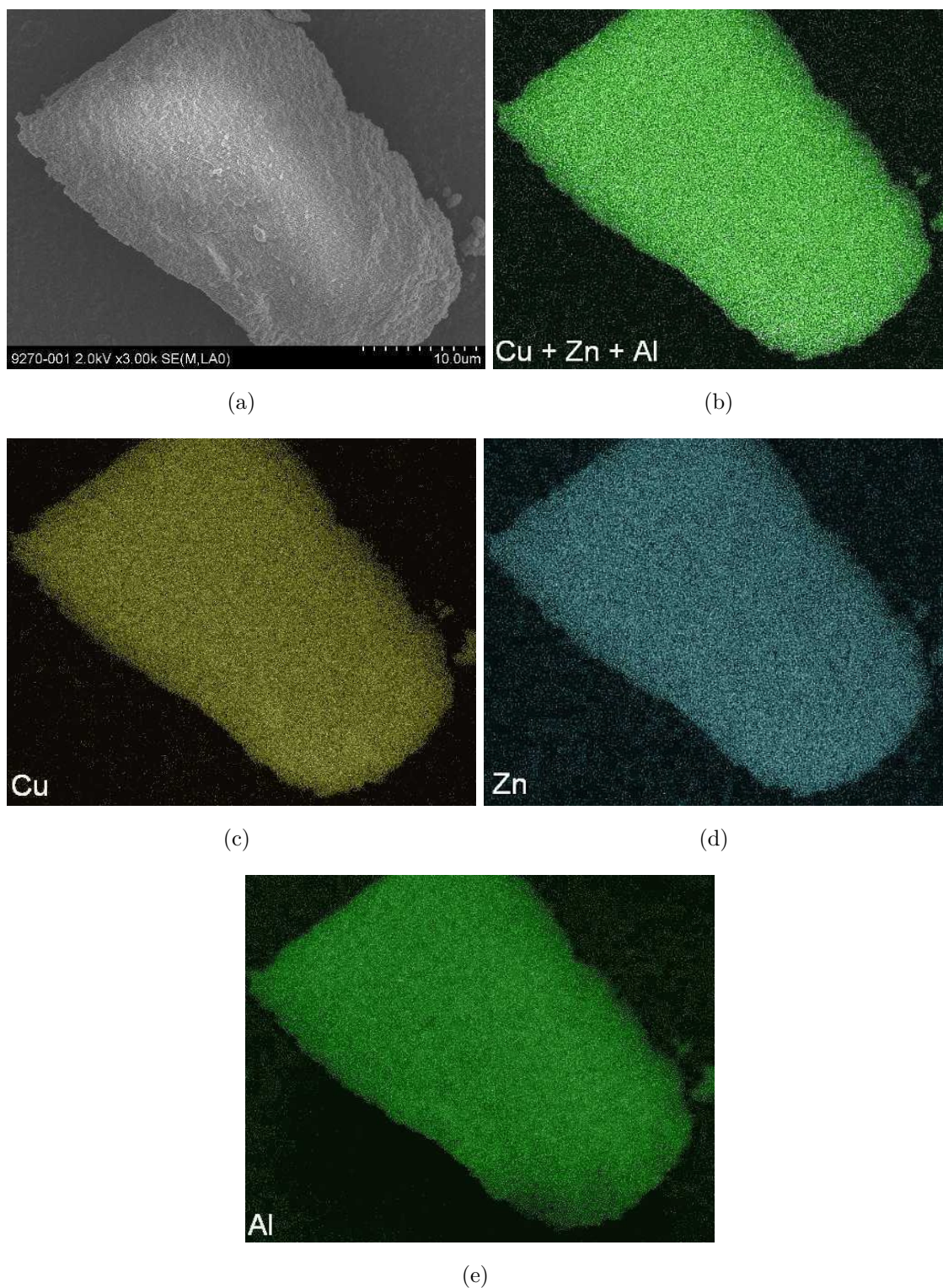
Figure A.3: SEM characteristics of CZA-calc: (a) SEM image; elemental mapping: (b) overview of distribution, (c) Cu, (d) Zn, (e) Al.
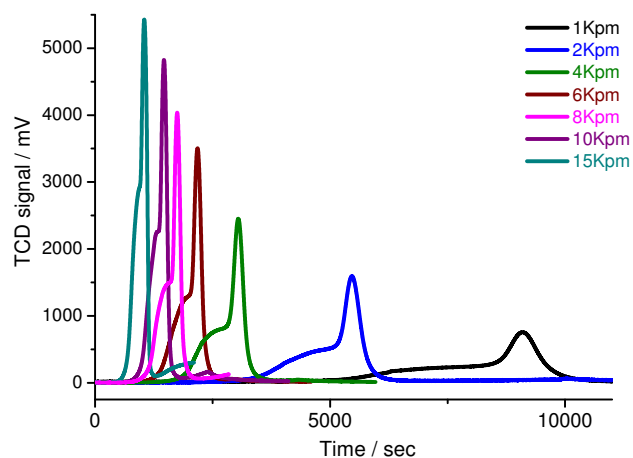
Figure A.4: Heating rate dependent TPR profiles of CZA-calc - time profile.
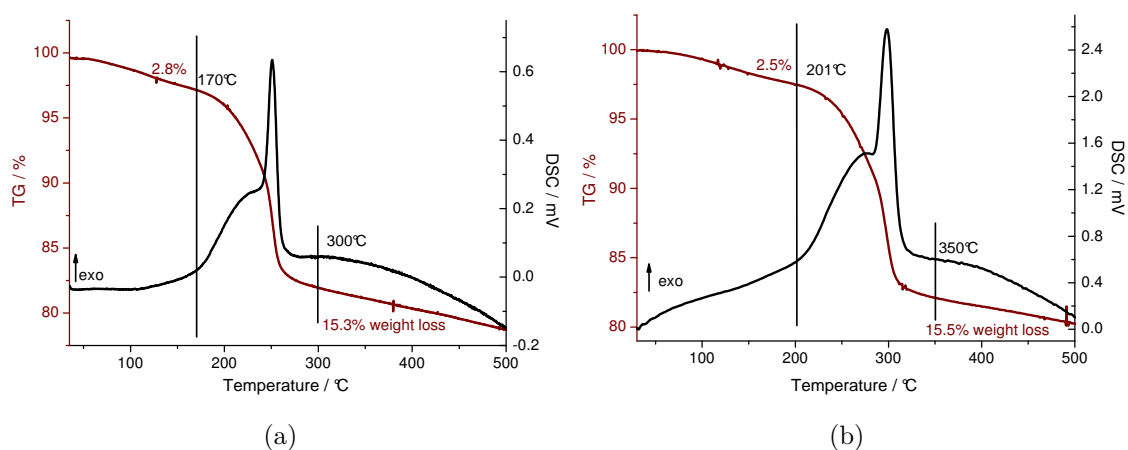
Figure A.5: TG-DSC curves of reduction in hydrogen of CZA-calc with (a) 2 K/min, (b) 10 K/min.
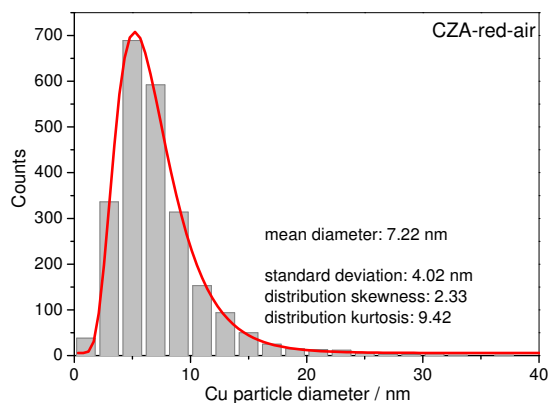
Figure A.6: Cu particle size distribution of CZA-red-air obtained from TEM images (2349 particles).

A.2 Diagrams and tables for the conventionally prepared reference catalyst

(a)   (b)
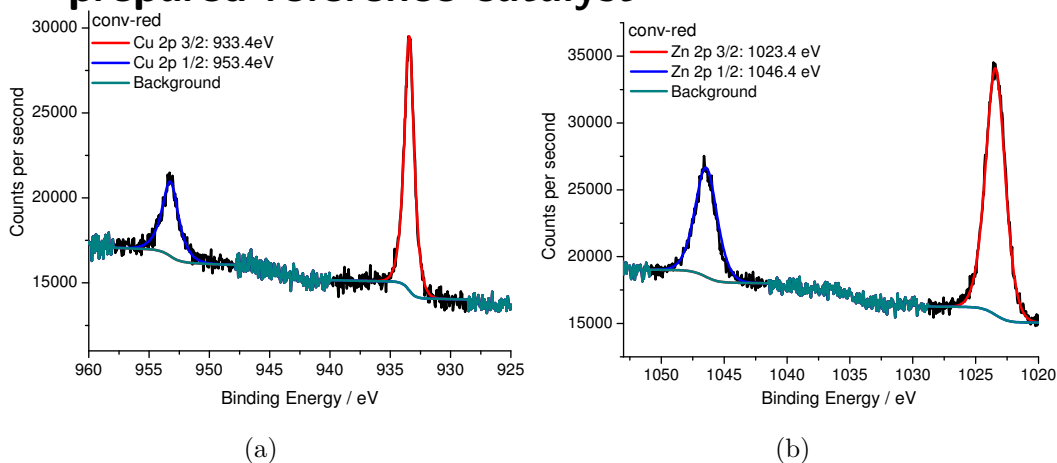
Figure A.7: XPS of conventionally prepared reference catalyst measured in in-situ XPS cell at $250\,^{\circ}$C in $0.25\,$mbar H_2: (a) peak deconvolution of Cu2p core level [84]; (b) peak deconvolution of Zn2p core level just indicating presence of ZnO [87].

Table A.1: XPS investigation of Cu2p and Zn2p during reduction of conv-red: decreasing Cu content on the surface.

| state	Cu:Zn	at% Cu
nominal	2.33	0.7
$70\,^{\circ}$C, H_2	1.9±0.2	0.66±0.07
$130\,^{\circ}$C, H_2	1.43±0.1	0.59±0.03
$155\,^{\circ}$C, H_2	1.34±0.1	0.57±0.04
$190\,^{\circ}$C, H_2	0.49±0.03	0.34±0.02
$220\,^{\circ}$C, H_2	0.39±0.03	0.28±0.02
$250\,^{\circ}$C, H_2	0.40±0.03	0.29±0.02

(a)   (b)
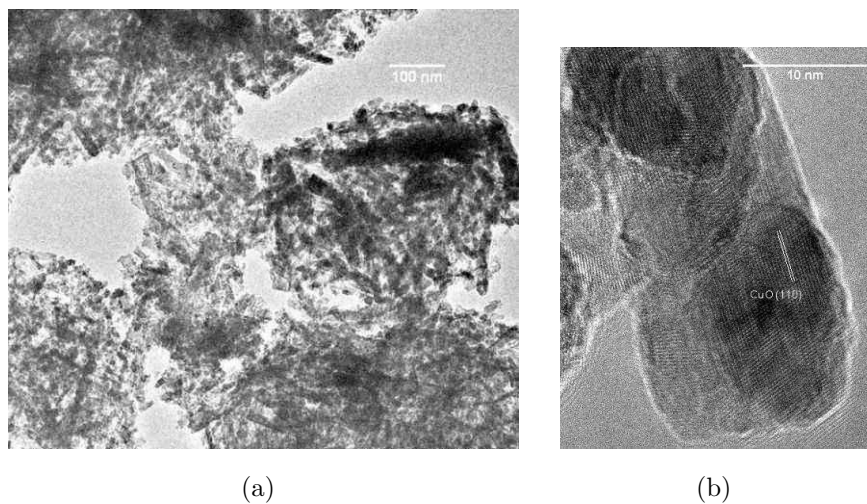
Figure A.8: TEM images of conv-calc.

(a)   (b)
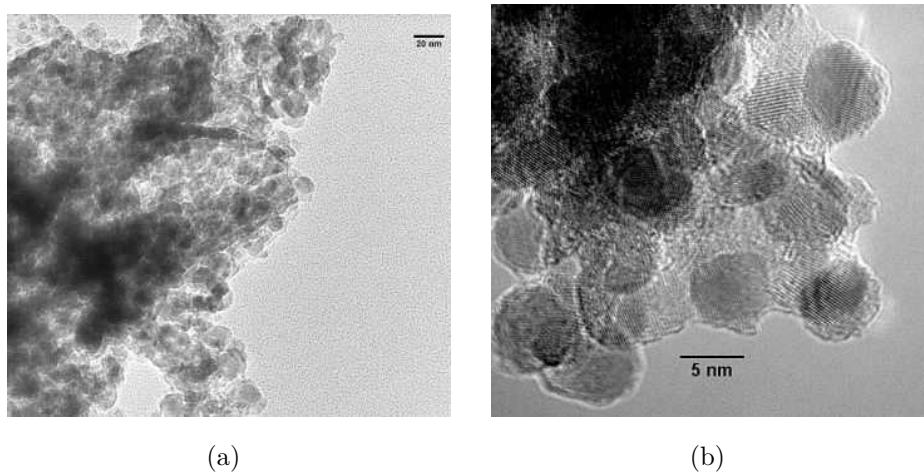
Figure A.9: TEM images of conventionally prepared reference catalyst.

A.3 Results of DLS measurements of microemulsions

Table A.2: Water droplet size determined by DLS in dependence of γ and α.

salt	γ	H$_2$O ratio [%]	α	droplet size [nm]
no	0.25	6	0.92	15
	0.25	8	0.89	21
	0.25	10	0.87	30
	0.225	8	0.9	20
	0.225	10	0.87	22
	0.225	12	0.85	39
metal	0.25	8	0.89	22
	0.225	8	0.9	22
base	0.25	8	0.89	25
	0.225	10	0.87	31

A.4 Additional informations to the analysis of the Cr substituted catalyst system

Figure A.10: Weight loss and MS traces (blue = H_2O and green = CO_2) of Cr substituted LDH compounds during heat treatment: (a) $5\,at\%$ Cr, (b) $10\,at\%$ Cr, (c) $15\,at\%$ Cr, (d) $20\,at\%$ Cr, (e) $25\,at\%$ Cr, (f) $33\,at\%$ Cr.

(a)

(b)

(c)

(d)

(e)

(f)
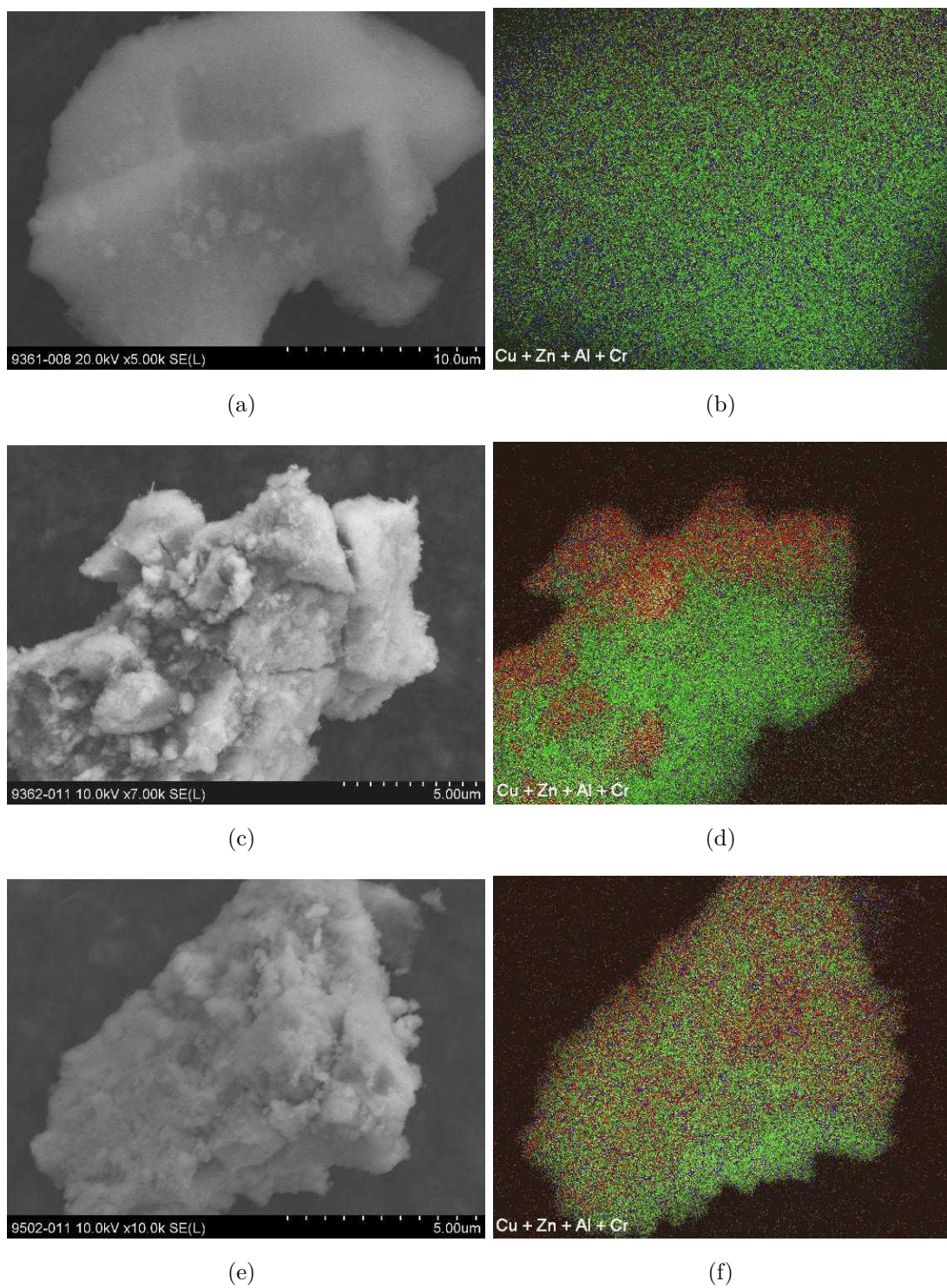
Figure A.11: Elemental distribution of Cr substituted LDH compounds: (a)-(b) $5\,at\%$ Cr, (c)-(d) $10\,at\%$ Cr, (e)-(f) $15\,at\%$ Cr.

(a)

(b)

(c)

(d)

(e)

(f)
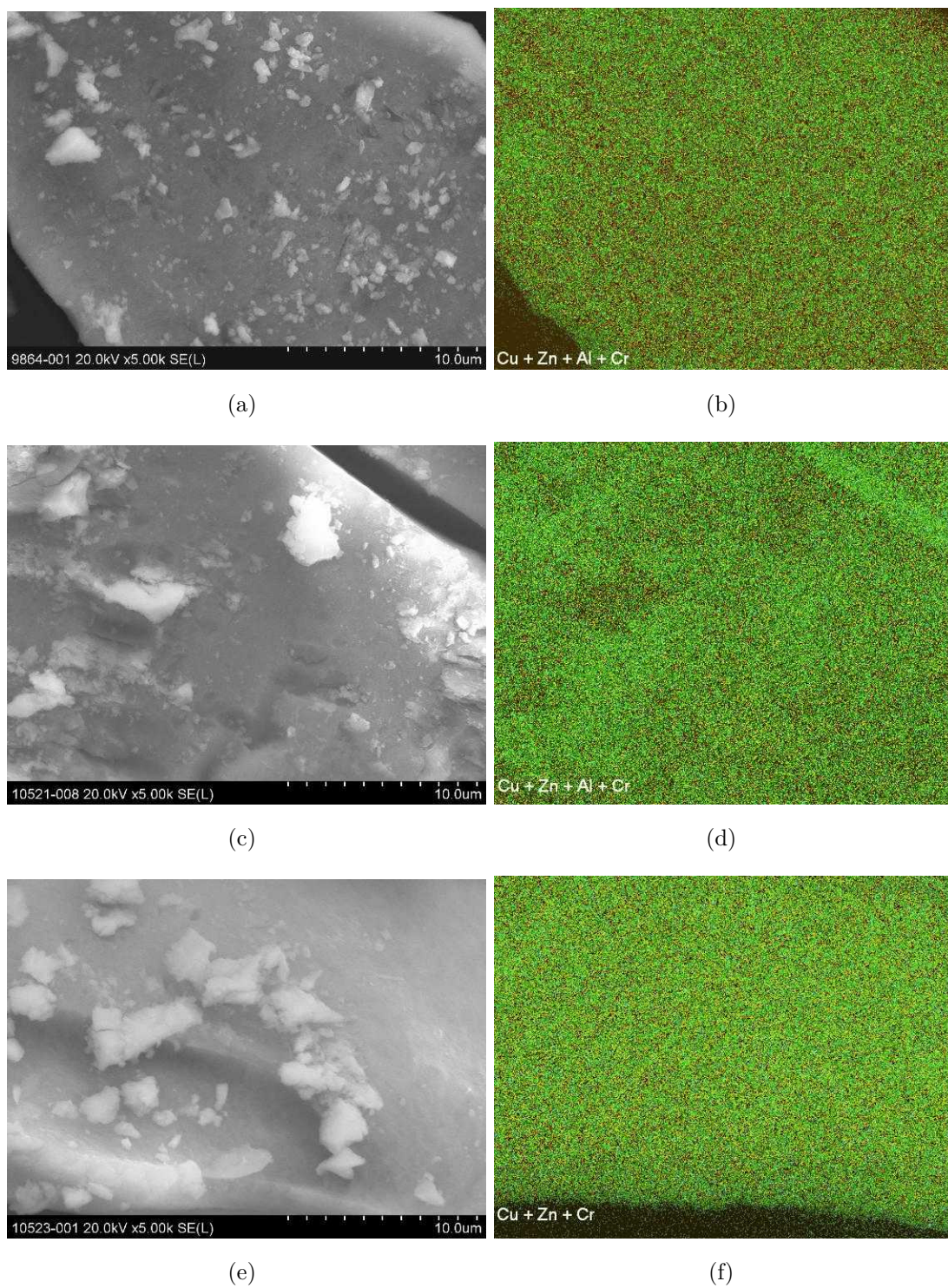
Figure A.12: Elemental distribution of Cr substituted LDH compounds: (a)-(b) 20 at% Cr, (c)-(d) Cr 25 at% Cr, (e)-(f) 33 at% Cr.
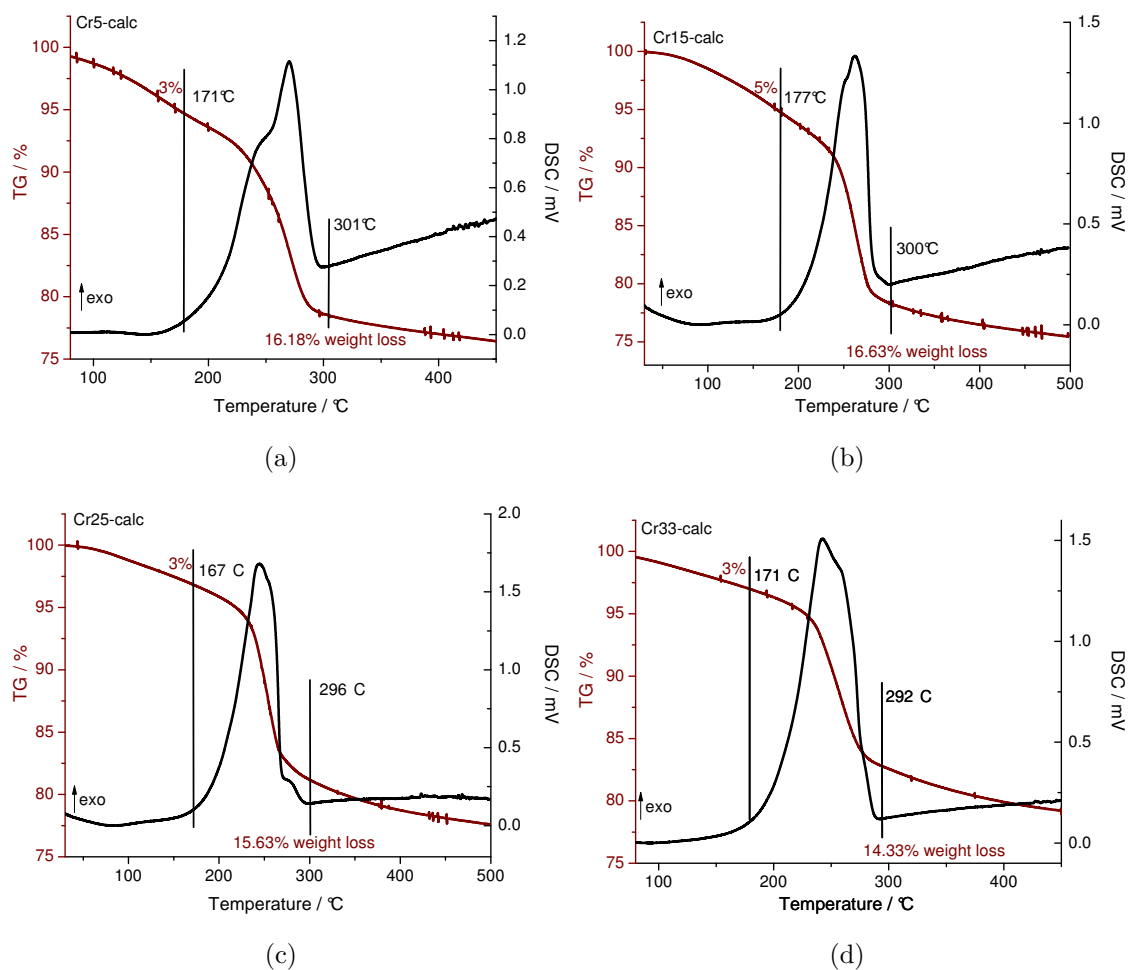
Figure A.13: TG-DSC curves during reduction in 5 % H$_2$ (5 K/min): (a) Cr5-calc, (b) Cr15-calc, (c) Cr25-calc (d) Cr33-calc.
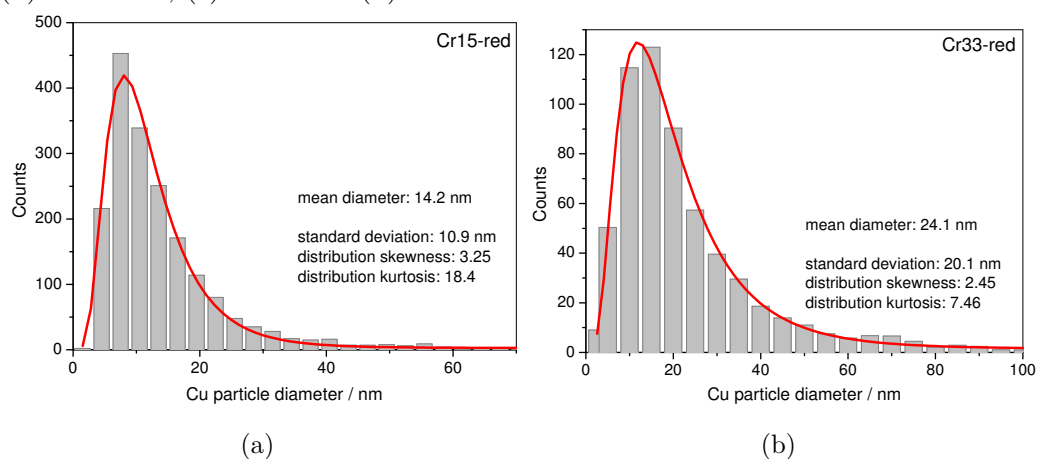
Figure A.14: Cu particle size distribution obtained by evaluation of TEM images of Cr containing catalysts: (a) Cr15-red (1838 particles), (b) Cr33-red (569 particles).

Table A.3: Results of TPR-TPO cyclization experiment of Cr series.

		CZA-calc	Cr5-calc	Cr15-calc	Cr25-calc	Cr33-calc
TPR1	T_{max}	285	266	258	246	240
	H_2/CuO	98	105	118	138	150
TPR2	T_{max}	203	208	229	246	240
	H_2/CuO	85	92	107	105	115

(a)   (b)
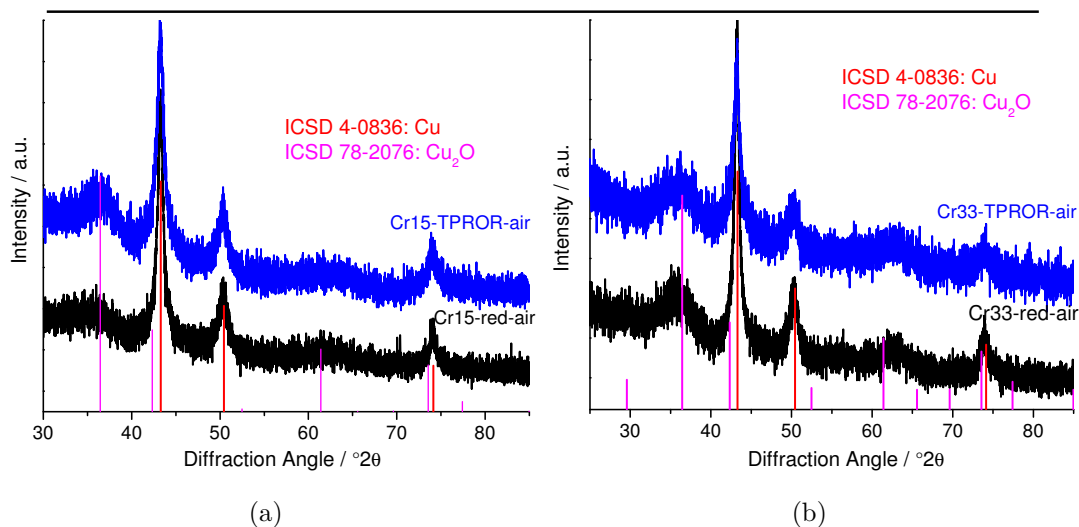
Figure A.15: XRD patterns of Cr containing catalysts handled in air after TPR and TPR-TPO-TPR: (a) $15\,at\%$ Cr, (b) $15\,at\%$ Cr.
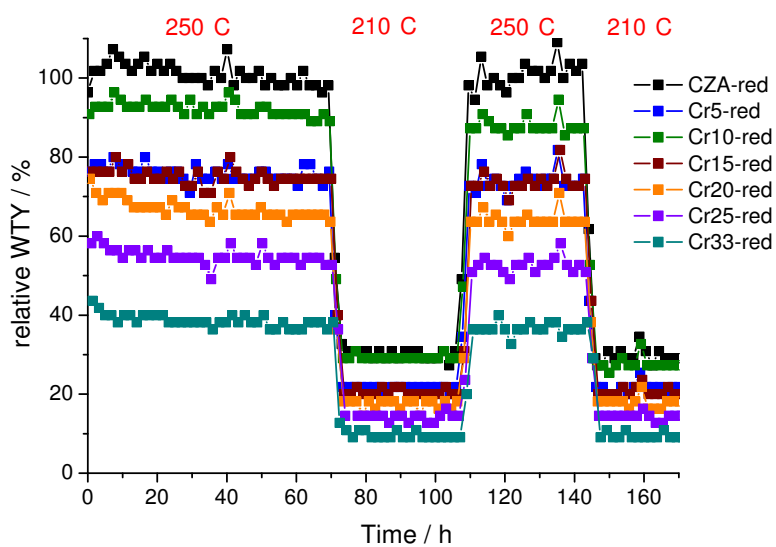
Figure A.16: Comparison of activity versus time on stream.

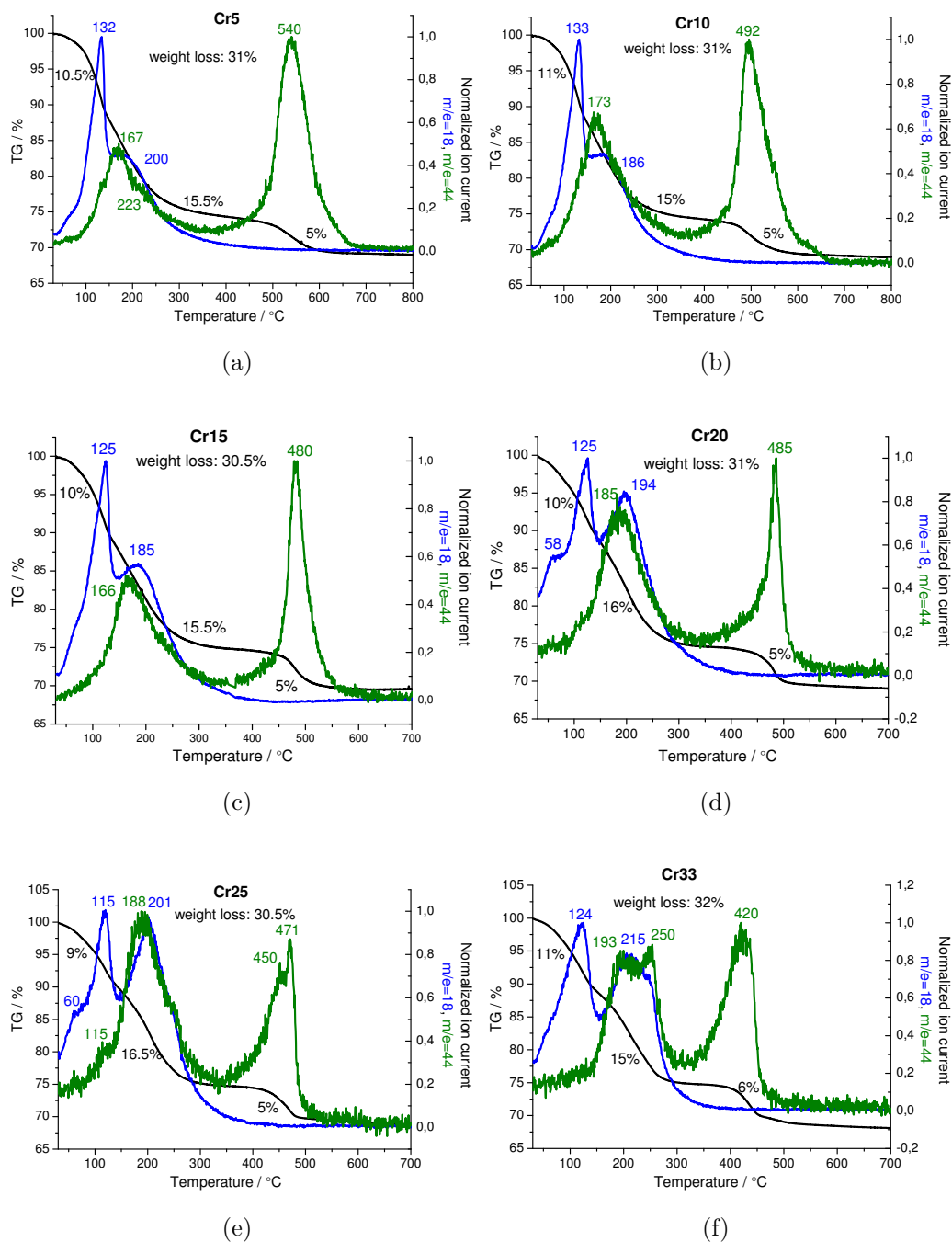## A.5 Additional informations to the analysis of the Ga substituted catalyst system
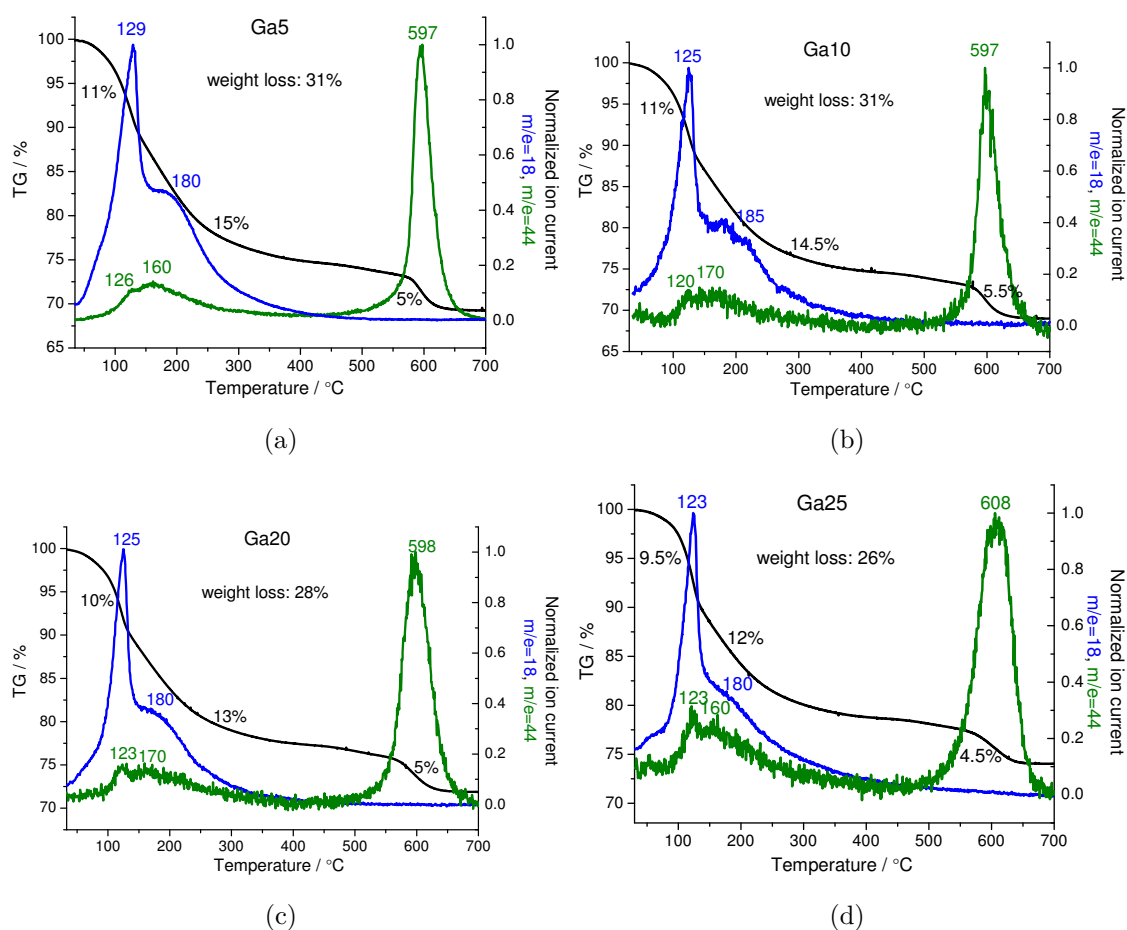
Figure A.17: Weight loss and MS traces (blue = H_2O and green = CO_2) of Ga substituted LDH compounds during heat treatment: (a) $5\,\mathrm{at\%}$ Ga, (b) $10\,\mathrm{at\%}$ Ga, (c) $20\,\mathrm{at\%}$ Ga, (d) $25\,\mathrm{at\%}$ Ga.

(a)

(b)

(c)

(d)

(e)

(f)

(g)

(h)
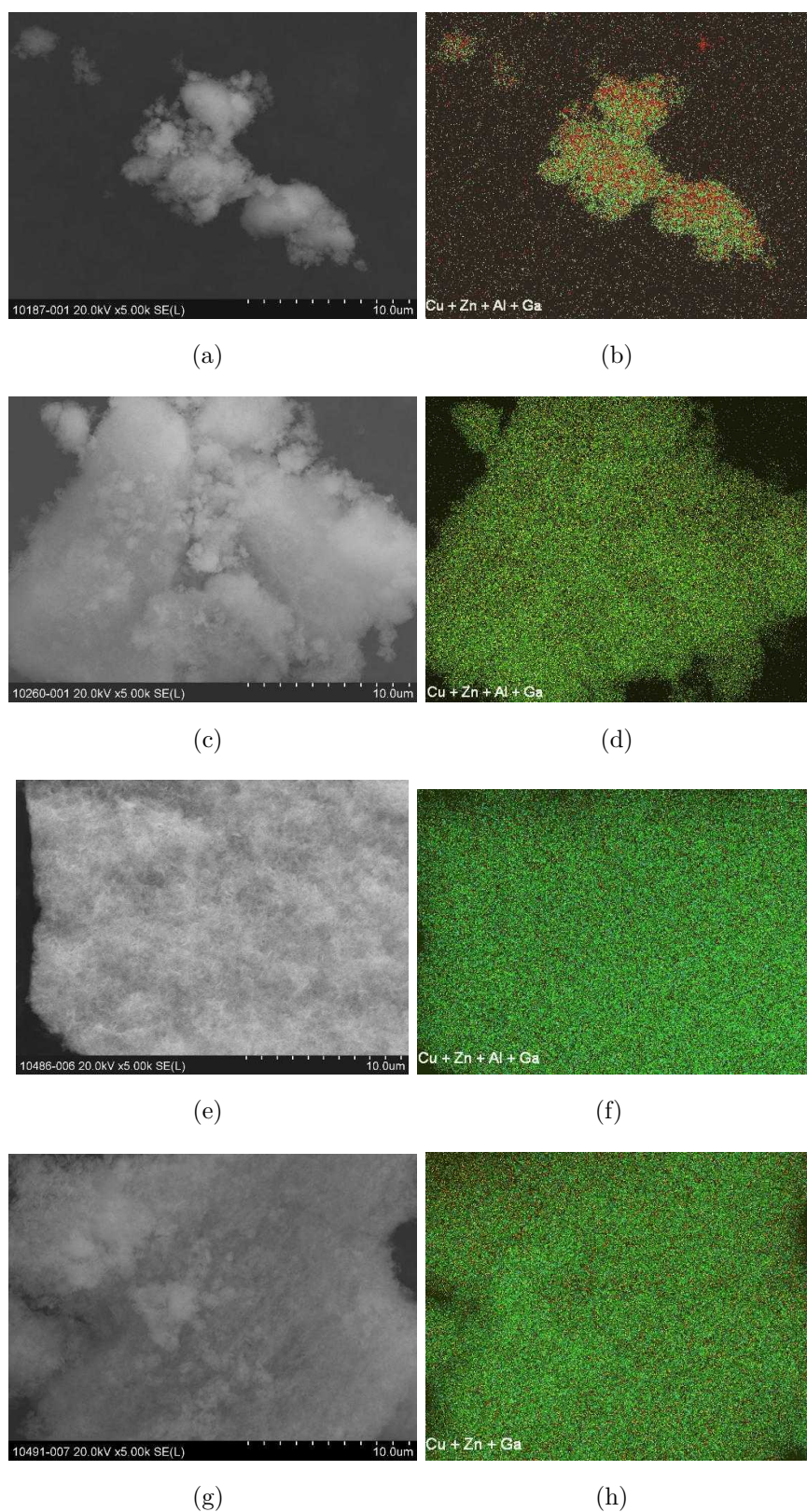
Figure A.18: Elemental distribution of Ga substituted LDH compounds: (a)-(b) 10 at% Ga, (c)-(d) 20 at% Ga, (e)-(f) 25 at% Ga, (g)-(h) 33 at% Ga.
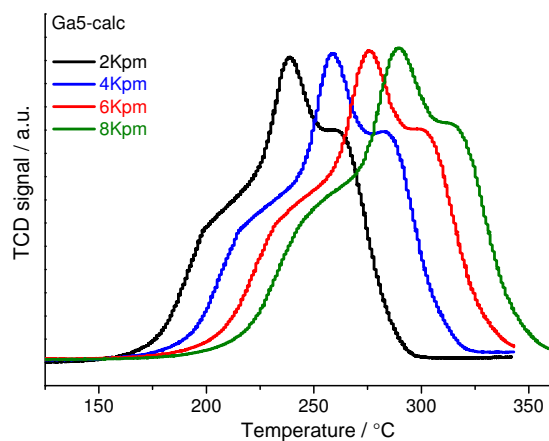
Figure A.19: TPR profiles of Ga5-calc measured with different heating rates.

(a)

(b)
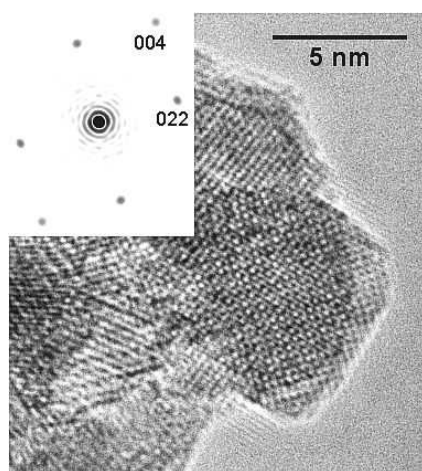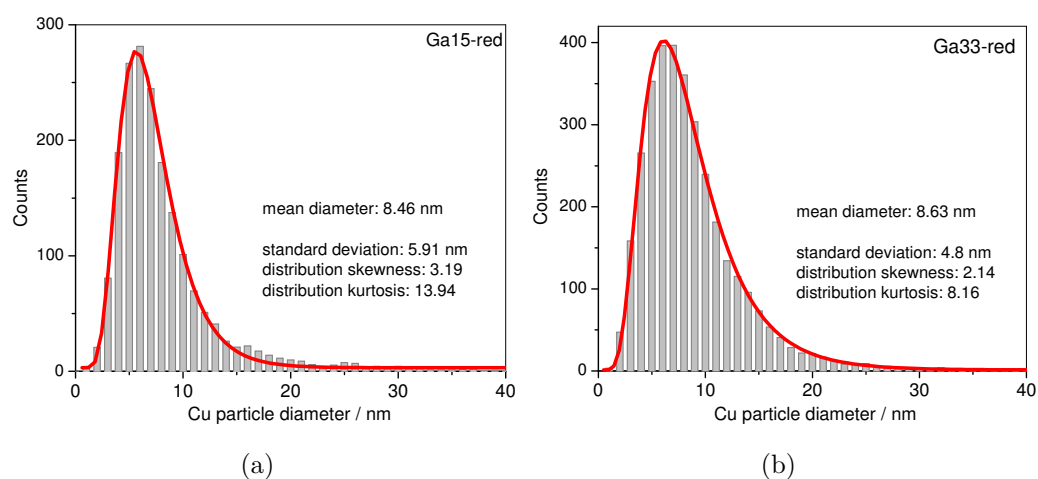
(c)

Figure A.20: Cu particle size distribution from TEM images of Ga containing catalysts: (a) Ga15-red (1699 particles), (b) Ga33-red (3158 particles) and selected TEM image of Ga33-red showing crystalline $ZnGa_2O_4$ – (100) lattice plane.

Figure A.21: XRD patterns of Ga containing catalysts handled in air after TPR and TPR-TPO-TPR: (a) 15 at% Ga, (b) 15 at% Ga.

Table A.4: Results of TPR-TPO cyclization experiment of Ga series.

		CZA-calc	Ga5-calc	Ga15-calc	Ga25-calc	Ga33-calc
TPR1	T_{max}	285	275	294	274	264
	H_2/CuO	98	95	99	99	96
TPR2	T_{max}	203	203	208	201	198
	H_2/CuO	85	86	87	87	88

A.6 Sample identification - FHI intern

Table A.5: Samples of CZA system: (a) pH variation (Chap. 4.1) and (b) precursor and calcined samples (Chap. 4.2).

(a)		(b)	
Label	FHI samplenumber	Label	FHI samplenumber
pH8-LDH	7201	CZA	7201, 7965, 9255
pH8-calc	7330	CZA-330	7330, 7988, 9270
pH7-LDH	6103	CZA-200	7466
pH7-calc	6614	CZA-260	7474
pH9-LDH	6145	CZA-400	7475
pH9-calc	6553	CZA-500	7478
pH10-LDH	6132	CZA-600	7479
pH10-calc	6613	CZA-700	7500, 9908

Table A.6: CZA reduced samples related to #9270 (Chap. 4.4).

Label	FHI samplenumber	conditions
CZA-red-air	10472	H_2/Ar at $300\,°C$ $60\,min$, air
CZA-red	11408	H_2/Ar at $300\,°C$ $60\,min$, inert
CZA-TPRO	10601, 11997	TPR-TPO
CZA-TPROR	11553	TPR-TPO-TPR, inert
CZA-TPROR-air	10606, 11851	TPR-TPO-TPR, air
CZA-red-XPS	8792 (related to 7988)	H_2 at $280\,°C$ $60\,min$ in in-situ cell (BESSY), inert transfer

Table A.7: $ZnAl_2O_4$ spinel as reference compound.

Label	FHI samplenumber	remark
$ZnAl_2O_4$	7341	synthesis details see Chap. 3.4

Table A.8: Samples of microemulsion synthesis and co-precipitated one for comparison (Chap. 5).

Label	FHI samplenumber
ME-LDH	6020, 6852
ME-calc	6054, 6853
co-LDH	6391
co-calc	6522

Table A.9: Cr substituting Al – precursor and calcined samples; X is indicating the nominal Cr content, labels used in thesis given in table header, numbers are representing FHI samplenumbers (Chap. 6.2.2).

X	CrX	CrX-calc	CrX-700
5	9361	9504	9745
10	9362	9505	9746
15	9502	9552	9898
20	9864	9869	11216
25	10521	10525	11209
30	10522	10526	10522
33	10523	10527	11207

Table A.10: Cr substituting Al – reduced samples; labels used in thesis given in table header, numbers are representing FHI samplenumbers (Chap. 6.2.3).

X	CrX-red-air	CrX-red	CrX-TPROR-air
15	12183	11424	10867
33	12182	11415	10862

143

Table A.11: Ga substituting Al – precursor and calcined samples; X is indicating the nominal Ga content, labels used in thesis given in table header, numbers are representing FHI samplenumbers (Chap. 6.3.2).

X	GaX	GaX-calc	GaX-700
5	10186	10227	10364
10	10187	10228	11346
15	10259	10284	10373
20	10260	10285	11370
25	10486	10492	11134
30	10490	10493	11284
33	10491	10494	11251

Table A.12: Ga substituting Al – reduced samples; labels used in thesis given in table header, numbers are representing FHI samplenumbers (Chap. 6.3.3).

X	GaX-red-air	GaX-red	GaX-TPROR-air
15	12095	11513	10877
33	12092	11423	10866

Bibliography

[1] D. R. Palo, R. A. Dagle, J. D. Holladay, *Chem. Rev.* **2007**, *107*, 3992–4021.

[2] Methanol Institute Arrington, Global Methanol Supply and Demand Balance, 2005-2010E, `http://www.methanol.org`.

[3] K.-O. Hinrichsen, J. Strunk, *Nachr. Chem.* **2006**, *54*, 1080–1084.

[4] R. G. Herman, C. E. Bogdan, P. L. Kumler, D. M. Nuszkowski, *Mater. Chem. Phys.* **1993**, *35*, 233–239.

[5] J. Hansen, *Methanol Synthesis, in Handbook of Heterogeneous Catalysis, Vol.6* (Ed.: G. Ertl, H. Knoezinger, F. Schüth, J. Weitkamp), Wiley-VCH, 2nd ed., **2008**, pp. 2920–2949.

[6] P. J. A. Tijm, F. J. Waller, D. M. Brown, *Appl. Catal. A: General* **2001**, *221*, 275–282.

[7] D. Waller, D. Stirling, F. S. Stone, M. S. Spencer, *Faraday Discuss. Chem. Soc.* **1989**, *87*, 107.

[8] M. S. Spencer, *Top. Catal.* **1999**, *8*, 259–266.

[9] R. H. Höppner, E. B. M. Doesburg, J. J. F. Scholten, *Appl. Catal.* **1986**, *25*, 109–119.

[10] K. Klier, *Appl. Surf. Sci.* **1984**, *19*, 267–297.

[11] J. C. Frost, *Nature* **1988**, *334*, 577–580.

[12] J.-D. Grunwaldt, A. M. Molenbroek, N.-Y. Topsøe, H. Topsøe, B. S. Clausen, *J. Catal.* **2000**, *194*, 452–460.

[13] R. Naumann d'Alnoncourt, X. Xia, J. Strunk, E. Löffler, O. Hinrichsen, M. Muhler, *Phys. Chem. Chem. Phys.* **2006**, *8*, 1525–1538.

[14] B. Bems, M. Schur, A. Dassenoy, H. Junkes, D. Herein, R. Schlögl, *Chem. Eur. J.* **2003**, *9*, 2039–2052.

[15] M. M. Günter, T. Ressler, B. Bems, C. Büscher, T. Genger, O. Hinrichsen, M. Muhler, R. Schlögl, *Catal. Lett.* **2001**, *71*, 37–44.

[16] C. Forano, T. Hibino, F. Leroux, C. Taviot-Gueho, *Handbook of Clay Science - Chap. 13.1 Layered Double Hydroxides* (Ed.: F. Bergaya), Elsevier Ltd., **2006**, pp. 1021 –1095.

[17] F. Cavani, F. Trifiró, A. Vaccari, *Catal. Today* **1991**, *11*, 173–301.

[18] S. P. Newman, W. Jones, *New J. Chem.* **1998**, *22*, 105–115.

[19] A. de Roy, *Mol. Cryst. Liq. Cryst.* **1998**, *311*, 173–193.

[20] J. G. Nunan, P. B. Himelfarb, R. G. Herman, K. Klier, C. E. Bogdan, G. W. Simmons, *Inorg. Chem.* **1989**, *28*, 3868–3874.

[21] W. Feitknecht, *Helv. Chim. Acta* **1942**, *25*, 555–569.

[22] W. Feitknecht, M. Gerber, *Helv. Chim. Acta* **1942**, *25*, 131–137.

[23] Z. P. Xu, G. Stevenson, C.-Q. Lu, G. Q. Lu, *J. Phys. Chem. B* **2006**, *110*, 16923–16929.

[24] Y. You, H. Zhao, G. F. Vance, *J. Mater. Chem.* **2002**, *12*, 907–912.

[25] P. Gherardi, O. Ruggeri, F. Trifiro, A. Vaccari, *Prep. Catal. III* **1983**, 723–733.

[26] C. Busetto, G. del Piero, G. Manara, F. Trifiro, A. Vaccari, *J. Catal.* **1984**, *85*, 260–266.

[27] S. Gusi, F. Pizzoli, F. Trifiro, A. Vaccari, G. Del Piero, *Prep. Catal. IV* **1987**, 753–765.

[28] M. Turco, G. Bagnasco, U. Costantino, F. Marmottini, T. Montanari, G. Ramis, G. Busca, *J. Catal.* **2004**, *228*, 56–65.

[29] M. Behrens, I. Kasatkin, S. Kühl, G. Weinberg, *Chem. Mater.* **2010**, *22*, 386–397.

[30] C. Baltes, S. Vukojevic, F. Schüth, *J. Catal.* **2008**, *258*, 334–344.

[31] M. Behrens, F. Girgsdies, A. Trunschke, R. Schlögl, *Eur. J. Inorg. Chem.* **2009**, *10*, 1347–1357.

[32] I. Kasatkin, P. Kurr, B. Kniep, A. Trunschke, R. Schlögl, *Angew. Chem.* **2007**, *119*, 7465–7468.

[33] T. Fujitani, J. Nakamura, *Catal. Lett.* **1998**, *56*, 119–124.

[34] D. M. Whittle, A. A. Mirzaei, J. S. J. Hargreaves, R. W. Joyner, C. J. Kiely, S. H. Taylor, G. J. Hutchings, *Phys. Chem. Chem. Phys.* **2002**, *4*, 5915–5920.

[35] M. Behrens, *J. Catal.* **2009**, *267*, 24–29.

[36] M. Kurtz, N. Bauer, C. Büscher, H. Wilmer, O. Hinrichsen, R. Becker, S. Rabe, K. Merz, M. Driess, R. A. Fischer, M. Muhler, *Catal. Lett.* **2004**, *92*, 49–52.

[37] A. Mastalir, B. Frank, A. Szizybalski, H. Soerijanto, A. Deshpande, M. Niederberger, R. Schomäcker, R. Schlögl, T. Ressler, *J. Catal.* **2005**, *230*, 464–475.

[38] M. Behrens, A. Furche, I. Kasatkin, A. Trunschke, W. Busser, M. Muhler, B. Kniep, R. Fischer, R. Schlögl, *ChemCatChem* **2010**, *2*, 816–818.

[39] S. Schimpf, M. Muhler, *Synthesis of Solid Catalysts* (Ed.: K. de Jong), Wiley-VCH, **2009**, 329 ff.

[40] H. Wilmer, T. Genger, O. Hinrichsen, *J. Catal.* **2003**, *215*, 188–198.

[41] M. Kurtz, H. Wilmer, T. Genger , O. Hinrichsen, M. Muhler, *Catal. Lett.* **2003**, *86*, 77–80.

[42] B. Warren, *X-ray Diffraction*, Dover Publications, New York, **1990**, pp. 275.

[43] D. Herein, *X-Ray Powder Diffraction, in Handbook of Heterogeneous Catalysis, Vol.3* (Ed.: G. Ertl, H. Knoezinger, F. Schüth, J. Weitkamp), Wiley-VCH, 2nd ed., **2008**, pp. 765–774.

[44] International Center for Diffraction Data, `http://www.icdd.com`.

[45] H. Knoezinger, *Temperature-Programmed Reduction and Oxidation, in Handbook of Heterogeneous Catalysis, Vol.3* (Ed.: G. Ertl, H. Knoezinger, F. Schüth, J. Weitkamp), Wiley-VCH, 2nd ed., **2008**, pp. 1080–1096.

[46] N. W. Hurst, S. J. Gentry, A. Jones, B. D. McNicol, *Catal. Rev.-Sci-Eng.* **1982**, *24*, 233–309.

[47] D. A. M. Monti, A. Baiker, *J. Catal.* **1983**, *83*, 323–335.

[48] P. Malet, A. Caballero, *J. Chem. Soc. Faraday Trans. I* **1988**, *84*, 2369 –2375.

[49] J. Haber, *J. Less-Common Met.* **1977**, *54*, 243–261.

[50] 0. J. Wimmers, P. Arnoldy, J. A. Moulijn, *J. Phys. Chem.* **1986**, *90*, 1331–1337.

[51] G. C. Chinchen, C. M. Hay, H. D. Vandervell, K. C. Waugh, *J. Catal.* **1987**, *103*, 79–86.

[52] O. Hinrichsen, T. Genger, M. Muhler, *Chem. Eng. Technol.* **2000**, *23*, 956–959.

[53] R. M. Dell, F . S. Stone, P. F. Tiley, *Trans. Faraday Soc.* **1953**, *49*, 195–201.

[54] D.C. Koningsberger, D.E. Ramaker, *Application of X-Ray Absorption Spectroscopy in Heterogeneous Catalysis, in Handbook of Heterogeneous Catalysis, Vol.3* (Ed.: G. Ertl, H. Knoezinger, F. Schüth, J. Weitkamp), Wiley-VCH, 2nd ed., **2008**, pp. 774–803.

[55] J. Stöhr, *NEXAFS Spectroscopy*, Springer-Verlag, **Berlin, 2003**.

[56] M. Salmeron, R. Schlögl, *Surf. Science Reports* **2008**, *63*, 169–199.

[57] F. M. F. de Groot, *J. Electron. Spectrosc. Relat. Phenom.* **1994**, *67*, 529–622.

[58] A.K. Datye, P.L. Hansen, S. Helveg, *Electron Microscopy Techniques, in Handbook of Heterogeneous Catalysis, Vol.3* (Ed.: G. Ertl, H. Knoezinger, F. Schüth, J. Weitkamp), Wiley-VCH, 2nd ed., **2008**, pp. 803–833.

[59] J. Niemantsverdriet, *Spectroscopy in Catalysis*, Wiley-VCH, 2nd ed., **2000**.

[60] K. S. W. Sing, D. H. Everett, R. A. W. Haul, L. Moscou, R. A. Pierotti, J. Rouquerol, T. Siemieniewska, *Pure & Appl. Chem.* **1984**, *57*, 603–619.

[61] S. Brunauer, P.H. Emmett, E. Teller, *J. Am. Chem. Soc.* **1938**, *60*, 309.

[62] A.V. Neimark, K. S. W. Sing, M. Thommes, *Surface Area and Porosity, in Handbook of Heterogeneous Catalysis, Vol.3* (Ed.: G. Ertl, H. Knoezinger, F. Schüth, J. Weitkamp), Wiley-VCH, 2nd ed., **2008**, pp. 721–738.

[63] S. Lowell, J. E. Shields, M. A. Thomas, M. Thommes, *Characterization of porous solids and powders: surface area, pore size and density*, Kluwer, **2004**.

[64] E. Barrett, L. Joyner, P. Halenda, *J. Am. Chem. Soc.* **1951**, *73*, 373.

[65] D. A. Skoog, J. J. Leary, *Instrumentelle Analytik: Grundlagen, Geräte, Anwendungen*, Springer, **1996**, pp. 611–622.

[66] J.J. Yeh, I. Lindau, *At. Data Nucl. Data Tables* **1985**, *32*, 1.

[67] M. A. Valenzuela, P. Bosch, G. Aguilar-Rios, A. Montoya, I. Schifter, *J. Sol-Gel Sci. Techn.* **1997**, *8*, 107–110.

[68] H. Bluhm, M. Haevecker, A. Knop-Gericke, E. Kleimenov, R. Schlögl, *J. Phys. Chem. B* **2004**, *108*, 14340–14347.

[69] M. Behrens, D. Brennecke, F. Girgsdies, S. Kißner, A. Trunschke, N. Nasrudin, S. Zakaria, N. Fadilah Idris, S. Bee Abd Hamid, B. Kniep, R. Fischer, W. Busser, M. Muhler, R. Schlögl, *Appl. Catal. A: General* **2011**, *392*, 93–102.

[70] G. J. Millar, I. H. Holm, P. J. R. Uwins, J. Drennan, *J. Chem. Soc. Faraday Trans.* **1998**, *94*, 593–600.

[71] N. J. Calos, J.S. Forrester, G. B. Schaffer, *J. Solid State Chem.* **1996**, *122*, 273.

[72] J. C. Waerenborgh, M. O. Figueiredo, J. M. P. Cabral, L. C. J. Pereira, *J. Solid State Chem.* **1994**, *111*, 300.

[73] G.C. Chinchen, P.J. Denny, J.R. Jennings, MS. Spencer and K.C. Waugh, *Appl. Catal.* **1988**, *36*, 1–65.

[74] G. Fierro, M. Lo Jacono, M. Inversi, P. Porta, F. Cioci, R. Lavecchia, *Appl. Catal. A: General* **1996**, *137*, 327–348.

[75] J. Y. Kim, J. A. Rodriguez, J. C. Hanson, A. I. Frenkel, P. L. Lee, *J. Am. Chem. Soc.* **2003**, *125*, 10684–10692.

[76] S. Gentry, N. Hurst, A. Jones, *J. Chem. Soc. Faraday Trans. I* **1981**, *77*, 603–619.

[77] S. Velu, K. Suzuki, M. Okazaki, M. P. Kapoor, T. Osaki, F. Ohashi, *J. Catal.* **2000**, *194*, 373–384.

[78] H. Bosch, B.J. Kip, J. G. van Ommen, P. J. Gellings, *J. Chem. Soc. Faraday Trans. I* **1984**, *80*, 2479–2488.

[79] J. Opfermann, *J. Therm. Anal. Calor.* **2000**, *60*, 641–658.

[80] M. J. Tiernan, P. A. Barnes, G. M. B. Parkes, *J. Phys. Chem. B* **1999**, *103*, 338–345.

[81] M. M. Günter, T. Ressler, R. E. Jentoft, and B. Bems, *J. Catal.* **2001**, *203*, 133–149.

[82] H. E. Swanson, E. Tatge, *National Bureau of Standards* **1953**, *539*, 15.

[83] D. Barreca, A. Gasparotto, E. Tondello, *Surface Science Spectra* **2007**, *14*, 41–51.

[84] A. C. Miller, G. W. Simmons, *Surface Science Spectra* **1993**, *2*, 55–60.

[85] C. D. Wagner, W.M. Riggs, L. E. Davis, J. F. Moulder, G. E. Muilenberg, *Handbook of X-ray Photoelectron Spectroscopy* (Ed.: G. E. Muilenberg), Perkin-Elmer Corporation, **1979**.

[86] B. R. Strohmeier, *Surface Science Spectra* **1995**, *3*, 128–134.

[87] D. Barreca, A. Gasparotto, C. Maccato, C. Maragno, E. Tondello, *Surface Science Spectra* **2007**, *14*, 19–26.

[88] R. Restori, D. Schwarzenbach, *Acta Crystallogr. Sec. B: Structural Science* **1986**, *42*, 201.

[89] C. Wagner, *J. Electrochem. Soc.* **1952**, *99*, 369–380.

[90] D. Adityawarmana, A. Voigt, P. Veit, K. Sundmacher, *Chem. Eng. Sci.* **2005**, *60*, 3373–3381.

[91] J. Agrell, K. Hasselbo, K. Jansson, S. G. Järas, M. Boutonnet, *Appl. Catal. A: General* **2001**, *211*, 239–250.

[92] F. Bellezza, A. Cipiciani, U. Costantino, M. Nocchetti, T. Posati, *Eur. J. Inorg. Chem.* **2009**, *10*, 2603–2611.

[93] G. Hu, D. O´Hare, *J. Am. Chem. Soc.* **2005**, *127*, 17808–17813.

[94] G. Hu, N. Wang, D. O´Hare, J. Davis, *J. Mater. Chem.* **2007**, *17*, 2257–2266.

[95] L. Sun, Y. Zhang, J. Zhang, C. Yan, C. Lia, Y. Lu, *Solid State Comm.* **2002**, *124*, 35–38.

[96] F. Rauscher, P. Veit, K. Sundmacher, *Coll. Surf. A* **2005**, *254*, 183–191.

[97]   B. Niemann, F. Rauscher, D. Adityawarman, A. Voigt, K. Sundmacher, *Chem. Eng. Pro.* **2006**, *45*, 917–935.

[98]   M. Turco, G. Bagnasco, U. Costantino, F. Marmottini, T. Montanari, G. Ramis, G. Busca, *J. Catal.* **2004**, *228*, 43–55.

[99]   M. Saito, T. Fujitani, M. Takeuchi, T. Watanabe, *Appl. Catal. A: General* **1996**, *138*, 311–318.

[100]   Q. Jiao, H. Liu, Y. Zhao, Z. Zhang, *J. Mater. Science* **2009**, *44*, 4422–4428.

[101]   A, Venugopal, J. Palgunadi, K. D. Jung, O.-S. Joo, C.-H. Shin, *Catal. Lett.* **2008**, *123*, 142–149.

[102]   R. D. Shannon, *Acta Cryst. Sec. A* **1976**, *32*, 751–767.

[103]   A. D. Apte, V. Tare, P. Bose, *J. Hazard. Mater. B* **2006**, *128*, 164–174.

[104]   A. B. Gaspar, L. C. Dieguez, *Appl. Catal. A: General* **2002**, *227*, 241–254.

[105]   M. Crivello, C. Pérez, J. Fernández, G. Eimer, E. Herrero, S. Casuscelli, E. Rodríguez-Castellón, *Appl. Catal. A.: General* **2007**, *317*, 11–19.

[106]   D. Grolimund, T. P. Trainor, J. P. Fitts, T. Kendelewicz, P. Liu, S.A. Chambers, G.E. Brown, Jr., *J. Synchrotron Rad.* **1999**, *6*, 612–614.

[107]   Y. Kawamura, K. Yamamotoa, N. Ogura, T. Katsumata, A. Igarashi, *J. Power Sources* **2005**, *150*, 20–26.

[108]   A. Venugopal, J. Palgunadi, J. K. Deog, O. Joob, C. Shin, *J. Mol. Catal. A: Chemical* **2009**, *302*, 20–27.

[109]   H. E. Swanson, R.K. Fuyat, *National Bureau of Standards* **1953**, *539*, 38.

Curriculum Vitae

Persönliche Informationen

Geboren am 07.05.1983 in Berlin

Ausbildung

2002-2007
Studium der Chemie an der Humboldt Universiät zu Berlin – Abschluss: Dipl. Chem.

02-07/2007
Diplomarbeit im Arbeitskreis von Prof. Kemnitz des Instituts für Chemie der Humboldt Universität zu Berlin.
Thema: „Organisch modifizierte Metallfluoride – anorganisch-organische Hybridsysteme durch Sol-Gel-Synthese"

Seit 10/2007
Promotion am Fritz-Haber-Institut (FHI) der Max-Planck-Gesellschaft in Berlin, Abteilung Anorganische Chemie.
Thema: „Synthese und Charakterisierung von Cu-basierten Katalysatoren hergestellt aus Cu,Zn,X Hydrotalcit-ähnlichen Verbindungen".

Contributions at conferences – Poster

Cu,Zn,Al hydrotalcite-like Compounds as Precursors for Copper Catalysts in Methanol Chemistry
S. Kühl, M. Behrens, R. Schlögl, *42. Jahrestreffen deutscher Katalytiker*, March 11-13, 2009, Weimar, Germany

Synthesis of Cu-based ex-hydrotalcite catalysts – structural characterization and first look to influencing parameters
S. Kühl, M. Behrens, *3rd IDECAT Conference on Catalysis*, May 19-24, 2009, Porquerolles, France

Cu-based ex-hydrotalcite catalyst synthesis – structural characterization and investigation of influencing parameters
S. Kühl, M. Behrens, *EuropaCat IX*, August 30-September 4, 2009, Salamanca, Spain

Neutronenbeugung an Cu basierten Methanol-Synthese-Katalysatoren
S. Kühl, S. Kißner, F. Girgsdies, M. Tovar, D. Wallacher, M. Behrens, *SNI*, February 24-26, 2010, Berlin, Germany

Neutron diffraction study of different Cu based methanol synthesis catalysts
S. Kühl, S. Kißner, F. Girgsdies, M. Tovar, D. Wallacher, M. Behrens, *43. Jahrestreffen deutscher Katalytiker*, March 10-12, 2010, Weimar, Germany

Cu,Zn,Al hydrotalcite-like Compounds as Precursors for Copper Catalysts in Methanol Chemistry
S. Kühl, M. Behrens, *1st Ertl Symposium on Electrochemistry and Catalysis*, April 11-14, 2010, GIST in Gwangju, South Korea

Cu-based catalysts resulting from Cu,Zn,Al layered double hydroxides
S. Kühl, M. Behrens, *15th Conference of GDCh, Division for Solid State Chemistry and Material Research*, September 20-21, 2010, Berlin, Germany

The Effect of Promoters on the Active Copper Phase in Methanol Chemistry Studied Using Cu,Zn,Al-Hydrotalcite-like Compounds as Model Systems
S. Kühl, M. Behrens, R. Schlögl, *44. Jahrestreffen deutscher Katalytiker*, March 16-18, 2011, Weimar, Germany

The Effect of Promoters on the Active Copper Phase in Methanol Chemistry Studied Using Cu,Zn,Al-Hydrotalcite-like Compounds as Model Systems
S. Kühl, M. Behrens, R. Schlögl, P. Kurr, *EuropaCat X*, August 28 - September 2, 2011, Glasgow, Great Britain